Title

Experimental comparison of pyranometer, reflectometer, and spectrophotometer methods for the measurement of roofing product albedo

Authors

Levinson, Ronnen
Egolf, Mischa
Chen, Sharon
et al.

Publication Date

2020-08-01

DOI

10.1016/j.solener.2019.11.103

Peer reviewed

This document is a pre-print of the following publication:

> Levinson, R., Egolf, M., Chen, S., & Berdahl, P. (2020). Experimental comparison of pyranometer, reflectometer, and spectrophotometer methods for the measurement of roofing product albedo. *Solar Energy*, *206*, 826–847. https://doi.org/10.1016/j.solener.2019.11.103

The pre-print may lack improvements made during the typesetting process. If you do not have access to the publication, you may request it from Ronnen Levinson at Lawrence Berkeley National Laboratory (RML27@cornell.edu).

Experimental comparison of pyranometer, reflectometer, and spectrophotometer methods for the measurement of roofing product albedo

Ronnen Levinson [a,*], Mischa Egolf [b], Sharon Chen [a,] and Paul Berdahl [a]

[a] Heat Island Group, Lawrence Berkeley National Laboratory, Berkeley, CA, USA

[b] Cool Roof Rating Council, Portland, OR, USA

[*] Corresponding author (RML27@cornell.edu)

2019-11-24

Abstract

Albedo (solar reflectance) can be measured outdoors with a pyranometer or indoors with a hemispherical reflectometer or a spectrophotometer. The current study evaluates these methods and their applicability to roofing materials by measuring and comparing the ASTM E1918 (pyranometer), non-ASTM E1918A (alternative pyranometer), ASTM C1549 (reflectometer), and E903 (spectrophotometer) albedos of 10 roofing products, including three single-ply membranes, one asphalt shingle, three roofing aggregates, and three high-profile tiles. It uses full-size (4 m × 4 m) assemblies in the E1918 and E1918A trials; corrects the E1918 albedos to remove shadow and background errors; and evaluates C1549 and E903 albedos with two different irradiance spectra, one global horizontal and the other beam normal.

E1918A albedos matched E1918 corrected (E1918_cor) albedos to within 0.036. Agreement between C1549 air mass 1 global horizontal (C1549_G1) albedo and E1918_cor albedo was within 0.015 for membrane and shingle coupons, and within 0.031 for aggregates, though the uncertainty in the latter agreement was up to 0.043. After minor corrections, C1549_G1 albedos of flat or slightly convex tile chips were 0.032 to 0.052 higher than the E1918_cor albedos of their corresponding high-profile tile assemblies because high-profile surfaces have concavities. Switching to the beam-normal albedo C1549_1.5E increased the C1549 albedos of the 10 tested products by 0.004 to 0.054, with the largest increases (C1549_1.5E – C1549_G1) accruing to spectrally selective cool colors. Using C1549_1.5E albedo to characterize a chip of a cool-colored tile compounded the error associated with representing a high-profile surface by a flat or slightly convex specimen.

Keywords

solar reflectance; albedo; pyranometer; hemispherical reflectometer; solar spectrophotometer; roofing product

Nomenclature

Note that the use of certain symbols (a, A, b, B, H, X, Y, and Z) to simplify view-factor formulas and other complex expressions is not detailed in these tables.

English symbols

a	Edge length
A	Area
b	Edge length
c	Distance between two surfaces
$F_{x\to y}$	View factor from surface x to surface y
h	Height
I	Downwelling solar radiance
J	Upwelling solar radiance
l	Arc length
p	Probability of photon return to surface
r	Radius
R	Nondimensional radius
$\mathcal{R}_{\text{E1918}}$	E1918 albedo
$\mathcal{R}_{\text{E1918A}}$	E1918A albedo
$\mathcal{R}$	Measured reflectance *or* planar reflectance
$\hat{\mathcal{R}}$	Macroscopic reflectance
S	Surface area
w	Chord length

Greek symbols

β	Solar altitude angle
δ	Uncertainty *or* difference in reflectance decrease
$\Delta\mathcal{R}$	Reflectance decrease
η	Area ratio
θ	Half angle swept by arc segment
μ	Mean
ρ	True albedo
σ	Standard deviation
ϕ	Diffuse fraction of global horizontal solar irradiance

1 Introduction

Roofing product albedo (solar reflectance) is rated to demonstrate compliance with minimum albedo requirements present in a variety of building energy codes and standards, green building standards, green building rating systems, and energy efficiency qualifications programs (Akbari and Levinson, 2008; Cool Roof Rating Council, 2018a), including California Title 24 Building Energy Efficiency Standards (California Energy Commission, 2016), California Green Building Standards Code (CALGreen) (California Building Standards Commission, 2016), ASHRAE

Standard 90.1 (ASHRAE, 2016), ASHRAE Standard 189.1 (ASHRAE, 2014), the International Energy Conservation Code (International Code Council, 2018a), the International Green Construction Code (International Code Council, 2018b), the US Green Building Council's Leadership in Energy and Environmental Design (LEED) green building rating system (U.S. Green Building Council, 2018), and the US EPA Energy Star program (United States Environmental Protection Agency, 2018).

The albedo of roofing materials can be measured outdoors with a pyranometer or indoors with a hemispherical reflectometer or a spectrophotometer. Levinson et al. (2010a, 2010b) detailed the selection of a solar reflectance metric for calculation of terrestrial solar heat gain; analyzed pyranometer, reflectometer, and spectrophotometer methods for albedo measurement; and provided guidance about the suitability of each method to various test surface geometries. The current study evaluates these methods and their applicability to roofing products.

ASTM E1918-16: Standard Test Method for Measuring Solar Reflectance of Horizontal and Low-Sloped Surfaces in the Field (ASTM International, 2016a) determines albedo as the ratio of the reflected sunlight incident on a downward pyranometer to downwelling sunlight incident on an upward pyranometer. Its hemispherical field of view lets it capture the effect of surface roughness on albedo, and its use of natural sunlight helps evaluate albedo under real-world illumination. However, it requires a large test specimen, or "target" (at least 4 m × 4 m if rectangular, or 4 m in diameter if circular); a clear sky; and a solar incidence angle of at least 45°. E1918 measurements are also subject to errors induced by the shadows of the pyranometer and its support (shadow error) and reflection of sunlight from the target's surrounding (background error) (Levinson et al., 2010b). ASTM E1918's precision-and-bias statement for a first-class albedometer ("Instrument C") reports intralaboratory repeatability standard deviations of 0.0023 – 0.0056 (mean 0.0040) and interlaboratory reproducibility standard deviations of 0.0080 – 0.0138 (mean 0.0114) from a study with seven participants and three roofing materials (two membranes and a metal product) (ASTM International, 2016a).

Non-ASTM alternative pyranometer method E1918A (Akbari et al., 2008; Levinson et al., 2010b) minimizes shadow error and eliminates background error by determining albedo from the sunlight reflected by a test specimen in three configurations—covered by a solar-opaque white mask, covered by a solar-opaque black mask, and uncovered—and the laboratory-measured albedos of the masks. Each mask is typically 1 m², and the target is the region exactly covered by the masks. Substituting E1918A for E1918 reduces the minimum target size by a factor of 16, but also deceases the sensor-to-target view factor by about 42%, lowering the ratio of signal to noise. This method has not yet been tested in an interlaboratory study.

Other pyranometer methods designed to measure the albedo of a limited-extent test surface surround the surface with a shade ring (Sailor et al., 2006) or restrict the pyranometer's field of view with a light baffle (Mei et al., 2017; Qin et al., 2018; Qin and He, 2017). These are not explored in the current study.

ASTM C1549-16: Standard Test Method for Determination of Solar Reflectance Near Ambient Temperature Using a Portable Solar Reflectometer (ASTM International, 2016b) evaluates albedo with a solar hemispherical reflectometer. The Solar Spectrum Reflectometer (SSR; Devices & Services, Dallas, TX) specified by C1549 illuminates the test specimen with diffuse incandescent light, and measures diffuse-near normal albedo with a set of filtered detectors whose weighted and summed solar spectral response can mimic various solar spectral irradiances. Since diffuse-directional reflectance equals directional-hemispherical reflectance (Howell et al., 2015), the reflectometer returns near normal-hemispherical albedo.

C1549 does not specify the spectrum to use, leaving it to the operator to select one consistent with that incident on a roof. Levinson et al. (2010b) found that choosing a solar spectral irradiance that excludes skylight can overestimate the C1549 albedo of a spectrally selective ("cool-colored") surface by up to 0.08.

The instrument is fast—about 10 s per measurement—and can determine the albedo of a flat, homogeneous product with a small target, typically about 10 cm × 10 cm to permit placement of the instrument's 2.5 cm diameter sample port at three non-overlapping spots. The mean albedo of a flat, heterogeneous product can be measured following either Procedure A (exhaustive sampling) or Procedure B (random sampling) in Appendix X1 of C1549-16. The albedo of roofing aggregate layers of modest profile—e.g., that formed by aggregates up to 1.6 cm (5/8") in particular size—can also be measured via C1549 following the Method A ("box of rocks") exhaustive sampling process specified by Levinson et al. (2014). Method A of Levinson et al. (2014) is essentially identical to Procedure A in Appendix X1 of C1549-16 but has been shown to match roofing aggregate albedos measured following E1918.

The instrument's small sample port (diameter 2.5 cm) and even smaller measurement area within the port (diameter 1.9 cm) makes it difficult to capture the effect of the concavities present in high-profile roofing assemblies, such as S-tile, barrel-tile, or profiled-metal roofs, though the instrument has been used to measure the albedo of crimped-foil miniature models of high-profile surfaces (Moore, 2009). The reflectometer's measurement head can be oriented in any direction, facilitating the measurement of loose roofing materials—e.g., aggregate—that must be placed on a horizontal surface.

C1549's precision-and-bias statement reports intralaboratory repeatability standard deviations of 0.0006 – 0.0021 (mean 0.0014) and interlaboratory reproducibility standard deviations of 0.0015 – 0.0072 (mean 0.0038) from a study with six participants and seven unspecified roofing materials (ASTM International, 2016b). Synnefa et al. (2013) also compared reflectometer and spectrophotometer measurements of albedo. Their interlaboratory study of C1549 with four participants and 17 roofing materials (five coatings, three modified-bitumen membranes, one asphalt shingle, one single-ply membrane, three concrete tiles, and four metal products) found interlaboratory reproducibility standard deviations of 0.0000 – 0.0403 (mean 0.0087).

ASTM E903-12: Standard Test Method for Solar Absorptance, Reflectance, and Transmittance of Materials Using Integrating Spheres (ASTM International, 2012) specifies a practice for

measuring near normal-hemispherical solar spectral reflectance with a UV-visible-near infrared spectrophotometer fitted with an integrating sphere. This class of instrument is typically used to characterize the reflectance of a small, homogeneous specimen because its collimated light source illuminates only about 10 mm² of the target. One can measure the reflectance at multiple spots on the surface of a heterogenous product by repositioning the test specimen between trials; however, each trial takes several minutes, and special procedures, such as covering the apparatus and specimen with a blackout curtain, are needed to accommodate specimens too large to fit inside the instrument's reflectance sample port, typically 10 cm × 15 cm. A spectrophotometer can be used to measure the reflectance of loose roofing materials if its reflectance sample port is at the bottom of the integrating sphere, but this port is more commonly on the side of the sphere.

E903 describes several functionally equivalent methods for computing albedo by weighting solar spectral reflectance with a representative solar spectral irradiance. While the standard provides examples of solar spectral irradiances that might be suitable for terrestrial applications, the irradiance spectrum is not prescribed, again leaving it to the operator to select one consistent with that incident on a roof.

E903's summary of bias, precision, and uncertainty (Section X3.2) states that the uncertainty in a given solar-weighted optical property is 0.02 (ASTM International, 2012). An interlaboratory study of E903 by Synnefa et al. (2013) with seven participants and the same 17 roofing materials used in their study of C1549 found interlaboratory reproducibility standard deviations of 0.0038 – 0.0310 (mean 0.0135) for the hazy-sky, beam-normal spectrum specified by ASTM E891-87(1992): Tables for Terrestrial Direct Normal Solar Spectral Irradiance Tables for Air Mass 1.5 (ASTM International, 1992).For a given choice of solar spectrum, C1549 albedo should closely match E903 albedo because the SSR's design was calibrated with spectrophotometer measurements (Levinson et al., 2010b). Using the aforementioned beam-normal spectrum, ASTM C1549's precision-and-bias statement reports that C1549 albedo exceeds E903 albedo by -0.0020 to 0.0290 (mean 0.0163), while the interlaboratory comparison by Synnefa et al. (2013) found that C1549 albedo exceeded E903 albedo by -0.050 to 0.020 (mean 0.005). The extreme difference of -0.050 in the latter study may have resulted from the use of a white tile standard, rather than a mirror standard, to calibrate the SSR before measuring the albedo of a bare metal specimen.Akbari, Levinson, and Stern (2008) compared pyranometer (E1918, E1918A) and spectrophotometer (E903) measurements of the albedos of 14 flat or curved roofing tile assemblies. They found that the E1918 and E1918A albedos of 9.3 m² assemblies agreed to within 0.03, but had difficulty relating the E1918 and E1918A albedos of assemblies to the E903 albedos of tile chips because the colors of the chips did not closely match those of the assembly tiles. Furthermore, none of the ten "large" (3.0 m × 3.0 m) assemblies and four smaller assemblies tested in the 2008 study provided the 4 m × 4 m minimum footprint required by E1918 for a rectangular target.[1] Finally, the study did measure the C1549 albedos of the tile chips, but omitted them because the

[1] Akbari et al. (2008) inaccurately converted the dimensions of the large assemblies from feet to meters. The true footprint and area of each large assembly was 10 ft × 10 ft (3.0 m × 3.0 m) and 100 ft² (9.3 m²), rather than 3.3 m × 3.3 m and 10 m². The 2008 study also incorrectly reported E1918's minimum target area as 10 m²; the actual requirement is 16 m² for a square target or 12.6 m² for a circular target.

reflectometer available at the time (SSR version 5) could not report an albedo based on a global horizontal solar irradiance (Levinson et al., 2010b).

The current study experimentally compares the E1918, E1918A, C1549, and E903 albedos of 10 roofing products, including three single-ply membranes, one asphalt shingle, three roofing aggregates, and three high-profile tiles. It uses full-size (4 m × 4 m) assemblies in the E1918 and E1918A trials; corrects the E1918 albedos to remove shadow and background errors identified by Levinson et al. (2010b); and evaluates C1549 and E903 albedos with two different irradiance spectra, one global horizontal (including both beam sunlight and diffuse skylight) and the other beam normal (including only beam sunlight, to match historical practice).

First, we establish the theory used to calculate albedo from pyranometer measurements of solar radiation, to correct for shadow and background errors in method E1918, to compute view factors used in these corrections, and to predict the reflectance decrease induced by the curvature of tile assemblies. Second, we describe the experimental measurement of roofing product albedos using pyranometer, reflectometer, and spectrophotometer methods. Third, we compare these measurements to gauge agreement between methods and identify systematic differences. Fourth, we compare measured decreases in tile-assembly reflectance values to theoretical predictions.

2 Theory

2.1 E1918 albedo

2.1.1 Definition

E1918 determines the albedo of its target as the ratio of upwelling radiance (radiative power per unit area) J incident on the sensor of the downward pyranometer to the downwelling radiance I incident on the sensor of the upward pyranometer. That is, the E1918 albedo

$$\mathcal{R}_{\mathrm{E1918}} = J/I \, . \tag{1}$$

2.1.2 Correction for shadow and background errors

The upwelling irradiance J incident on the downward pyranometer sensor is given by the radiative power summation

$$A_1 J = A_{2\mathrm{u}} I \rho_2 F_{2\mathrm{u}\to 1} + A_{2\mathrm{s}} \phi \rho_2 I F_{2\mathrm{s}\to 1} + A_{3\mathrm{u}} I \rho_3 F_{3\mathrm{u}\to 1} + A_{3\mathrm{s}} \phi I \rho_3 F_{3\mathrm{s}\to 1} \, , \tag{2}$$

where A_x is the area of surface x, $F_{x\to y}$ is the view factor from surface x to surface y, ρ_x is the true albedo of surface x, I is global horizontal solar irradiance, ϕ is the diffuse fraction of global horizontal solar irradiance, surface 1 is the sensor, surface 2 is the target, surface 3 is the target's background (surroundings), sub-surfaces 2s and 2u are the shaded and unshaded portions of the target, and sub-surfaces 3s and 3u are the shaded and unshaded portions of the background. Applying view factor reciprocity ($A_x F_{x\to y} = A_y F_{y\to x}$),

$$J = I\,\rho_2\,(F_{1\to 2\mathrm{u}} + \phi\,F_{1\to 2\mathrm{s}}) + I\,\rho_3\,(F_{1\to 3\mathrm{u}} + \phi\,F_{1\to 3\mathrm{s}}). \quad (3)$$

193 Therefore

$$\mathcal{R}_{\mathrm{E1918}} = J/I = a\,\rho_2 + b\,, \quad (4)$$

194 where

$$a = F_{1\to 2\mathrm{u}} + \phi\,F_{1\to 2\mathrm{s}} \quad (5)$$

195 and

$$b = \rho_3\,(F_{1\to 3\mathrm{u}} + \phi\,F_{1\to 3\mathrm{s}})\,. \quad (6)$$

196 Rearranging Eq. (4), the target's true albedo

$$\rho_2 = (\mathcal{R}_{\mathrm{E1918}} - b)/a\,. \quad (7)$$

197 Since the view factor to any surface is the sum of the view factors to its sub-surfaces,

$$F_{1\to 2\mathrm{u}} + F_{1\to 2\mathrm{s}} = F_{1\to 2} \quad (8)$$

$$F_{1\to 3\mathrm{u}} + F_{1\to 3\mathrm{s}} = F_{1\to 3} \quad (9)$$

198 and

$$F_{1\to 2} + F_{1\to 3} = 1. \quad (10)$$

199 Therefore

$$a = (F_{1\to 2} - F_{1\to 2\mathrm{s}}) + \phi\,F_{1\to 2\mathrm{s}} = F_{1\to 2} - (1-\phi)F_{1\to 2\mathrm{s}} \quad (11)$$

200 and

$$b = \rho_3\,[(F_{1\to 3} - F_{1\to 3\mathrm{s}}) + \phi\,F_{1\to 3\mathrm{s}}] = \rho_3\,[F_{1\to 3} - (1-\phi)F_{1\to 3\mathrm{s}}]\,. \quad (12)$$

201 If the view factor from the sensor to the shaded portion of the background is much smaller than
202 that to the unshaded portion of the background (i.e., $F_{1\to 3\mathrm{s}} \ll F_{1\to 3}$),

$$b \approx \rho_3\,F_{1\to 3} = \rho_3\,(1 - F_{1\to 2})\,. \quad (13)$$

203 This yields the correction constants a and b in terms of the sensor-to-target view factor $F_{1\to 2}$,
204 sensor-to-target shadow view factor $F_{1\to 2\mathrm{s}}$, background albedo ρ_3, and diffuse fraction ϕ:

$$a = F_{1\to 2} - (1-\phi)F_{1\to 2\mathrm{s}} \quad (14)$$

$$b \approx \rho_3\,(1 - F_{1\to 2})\,. \quad (15)$$

205 Given $F_{1\to 2}$ and ϕ, we can compute $F_{1\to 2\mathrm{s}}$ from a

$$F_{1\to 2\mathrm{s}} = (F_{1\to 2} - a)/(1-\phi) \quad (16)$$

206 and estimate ρ_3 from b:

$$\rho_3 \approx b/(1 - F_{1\to 2}) \; . \tag{17}$$

2.1.3 Adjusting means and standard deviations

Since the target's true albedo ρ_2 is linearly related to its E1918 albedo $\mathcal{R}_{\mathrm{E1918}}$ by Eq. (4), the mean and standard deviation of ρ_2 will also be linearly related to those of $\mathcal{R}_{\mathrm{E1918}}$.

If $y = a\,x + b$, the mean of y (μ_{y}) is related to that of x (μ_{x}) by

$$\mu_{\mathrm{y}} = a\,\mu_{\mathrm{x}} + b \tag{18}$$

and the standard deviation of y (σ_{y}) is related to that of x (σ_{x}) by

$$\sigma_{\mathrm{y}} = a\,\sigma_{\mathrm{x}} \; . \tag{19}$$

Rearranging,

$$\mu_{\mathrm{x}} = (\mu_{\mathrm{y}} - b)/a \tag{20}$$

and

$$\sigma_{\mathrm{x}} = \sigma_{\mathrm{x}}/a \; . \tag{21}$$

Therefore

$$\mu_{\rho_2} = (\mu_{\mathrm{R_{E1918}}} - b)/a \tag{22}$$

and

$$\sigma_{\rho_2} = \sigma_{\mathcal{R}_{\mathrm{E1918}}}/a \; . \tag{23}$$

2.2 E1918A albedo

E1918A determines the albedo of its target by comparing the upwelling radiance J incident on the sensor of downward pyranometer when the target is uncovered to that when the target is bare (configuration 3) to that when the target is exactly covered by a solar-opaque white mask (configuration 1) and that when the target is exactly covered by a solar-opaque black mask (configuration 2). That is, the E1918A albedo

$$\mathcal{R}_{\mathrm{E1918A}} = \rho_{\mathrm{black}} + \frac{J_3 - J_2}{J_1 - J_2}\,(\rho_{\mathrm{white}} - \rho_{\mathrm{black}}) \; , \tag{24}$$

where ρ_x is the true albedo of surface x (Akbari et al., 2008; Levinson et al., 2010b).[2]

Note that the masks must be exactly equal in size, and that the target is defined as the masked region.

[2] In practice, the white mask is likely to transmit some sunlight, while the black mask is usually solar opaque. The white mask should be placed over the black mask during E1918A trials and when measuring its true albedo with a laboratory technique.

2.3 Uncertainties in E1918 and E1918A albedos

The uncertainty in $f(x, y, z)$ induced by uncorrelated uncertainties δx, δy, and δz is

$$\delta f = \left[\left(\frac{\partial f}{\partial x}\,\delta x\right)^2 + \left(\frac{\partial f}{\partial y}\,\delta y\right)^2 + \left(\frac{\partial f}{\partial z}\,\delta z\right)^2\right]^{\frac{1}{2}}. \tag{25}$$

For simplicity, the following analyses assume that the pyranometer(s) used to measure solar irradiance are accurately calibrated; neglect tilt, cosine-response, and zero-offset errors; and consider only uncorrelated errors, such as those that might arise from variations in convection inside or outside the pyranometer domes, fluctuations in sky clarity, or electrical signal noise. Future research could investigate *systematic* errors in pyranometer measurement of irradiance and albedo.

2.3.1 E1918 albedo uncertainty

Let E1918 albedo $\mathcal{R} = f(I, J) = J/I$. Applying Eq. (25) and re-arranging,

$$\frac{\delta\mathcal{R}}{\mathcal{R}} = \left[\left(\frac{\delta J}{J}\right)^2 + \left(\frac{\delta I}{I}\right)^2\right]^{\frac{1}{2}}. \tag{26}$$

Substituting $J = I\,\mathcal{R}$ yields

$$\frac{\delta\mathcal{R}}{\mathcal{R}} = \left[\left(\frac{\delta J}{I\,\mathcal{R}}\right)^2 + \left(\frac{\delta I}{I}\right)^2\right]^{\frac{1}{2}}. \tag{27}$$

If $\delta J \le \delta_0$ and $\delta I \le \delta_0$,

$$\delta\mathcal{R} \le \frac{\delta_0}{I}\left[1 + \mathcal{R}^2\right]^{\frac{1}{2}}. \tag{28}$$

Since $\mathcal{R} \le 1$,

$$\delta\mathcal{R} \le \sqrt{2} \times \frac{\delta_0}{I}. \tag{29}$$

Example. If the uncorrelated uncertainties in upflux J and downflux I are each no more than δ_0=10 W/m² when I = 1,000 W/m², the resulting uncertainty in E1918 reflectance will be no more than 0.014.

2.3.2 E1918A albedo uncertainty

Let E1918A albedo $\mathcal{R} = f(J_1, J_2, J_3) = \rho_b + \frac{J_3 - J_2}{J_1 - J_2}\,(\rho_w - \rho_b)$ where ρ_w and ρ_b are the true albedos of the white and black masks, respectively. Applying Eq. (25),

$$\delta\mathcal{R} = \frac{\rho_w - \rho_b}{(J_1 - J_2)^2} \times \left[(J_3 - J_2)^2\,(\delta J_1)^2 + (J_1 - J_3)^2\,(\delta J_2)^2 + (J_1 - J_2)^2\,(\delta J_3)^2\right]^{\frac{1}{2}}. \tag{30}$$

If ρ_t is the true albedo of the test surface covered by the masks and F is the view factor from the pyranometer to the target (mask or test surface),

$$J_1 - J_2 = (\rho_w - \rho_b)\, F\, I \tag{31}$$

$$J_1 - J_3 = (\rho_w - \rho_t)\, F\, I \tag{32}$$

$$J_3 - J_2 = (\rho_t - \rho_b)\, F\, I \tag{33}$$

Substituting Eqs. (31) - (33) into Eq. (30) yields

$$\delta\mathcal{R} = \frac{1}{(\rho_w - \rho_b)\, F\, I} \times [(\rho_w - \rho_b)^2\, (\delta J_1)^2 + (\rho_w - \rho_t)^2\, (\delta J_2)^2 + (\rho_t - \rho_b)^2\, (\delta J_3)^2]^{\frac{1}{2}}. \tag{34}$$

If $\delta J_1 \le \delta_0$, $\delta J_2 \le \delta_0$, and $\delta J_3 \le \delta_0$,

$$\delta\mathcal{R} \le \frac{\delta_0}{(\rho_w - \rho_b)\, F\, I} \times [(\rho_w - \rho_b)^2 + (\rho_w - \rho_t)^2 + (\rho_t - \rho_b)^2]^{\frac{1}{2}} \tag{35}$$

or

$$\delta\mathcal{R} \le \frac{\delta_0}{F\, I} \times g(x), \tag{36}$$

where

$$x = \frac{\rho_t - \rho_b}{\rho_w - \rho_b} \tag{37}$$

and

$$g(x) = [2(1 - x + x^2)]^{\frac{1}{2}}. \tag{38}$$

If $\rho_b = 0.05$ and $\rho_w = 0.80$, $g(x) < 1.65$ for all possible values of target reflectance. Hence,

$$\delta\mathcal{R} \le 1.65 \times \frac{\delta_0}{F\, I}. \tag{39}$$

Example. If the uncorrelated uncertainties in upfluxes J_1, J_2, and J_3 are each no more than δ_0=10 W/m² when downflux I is 1,000 W/m², and the view factor to target from pyranometer is 0.55 (1 m² square mask centered under pyranometer), the resulting uncertainty in E1918A reflectance will be no more than 0.030.

2.4 View factors

2.4.1 Disc to parallel coaxial disc of unequal radius

The view factor from a circular pyranometer sensor to a parallel coaxial circular target equals that from a disc to a parallel coaxial disc of unequal radius. The view factor from a disc of radius r_1 (surface 1) to a parallel coaxial disk of radius r_2 at distance c (surface 2) is

$$F_{1\to 2} = \frac{1}{2}\left\{X - \left[X^2 - 4\left(\frac{R_2}{R_1}\right)^2\right]^{\frac{1}{2}}\right\}, \tag{40}$$

where $R_1 = \frac{r_1}{c}, R_2 = \frac{r_2}{c}$, and $X = 1 + (1 + R_2^2)/R_1^2$ (Howell, 2018, factor C-41).

We can use this relationship to show that the precise size or shape assigned to the 2 cm diameter sensor has minimal effect on the view factor from sensor to target or sensor to shadow. For example, applying Eq. (40) to compute the view factor from a circular sensor of radius 0.01, 1, or 2 cm to a parallel coaxial circular shadow of radius 7.5 cm at distance 50 cm—the shadow beneath a 15 cm diameter pyranometer when the sun is at zenith—yields view factors of 0.02200, 0.02200, and 0.02197, respectively. The first value is 0.04% higher than the second value, and the third value is 0.11% lower than the second value.

2.4.2 Square to parallel coaxial square of different edge length (pyranometer sensor to square E1918 target or square E1918A mask)

The view factor from a circular pyranometer sensor to a parallel coaxial square target is well approximated by that from a square to a parallel coaxial square of different edge length. The view factor from a square of edge length a (surface 1) to a parallel coaxial square of edge length b at distance c (surface 2) is

$$F_{1\to 2} = \frac{1}{\pi A^2}\left\{\ln\frac{\left[A^2(1+B^2)+2\right]^2}{(Y^2+2)(X^2+2)} + (Y^2+4)^{\frac{1}{2}}\left[Y\,\mathrm{atan}\frac{Y}{(Y^2+4)^{\frac{1}{2}}} - X\,\mathrm{atan}\frac{X}{(Y^2+4)^{\frac{1}{2}}}\right] + (X^2+4)^{\frac{1}{2}}\left[X\,\mathrm{atan}\frac{YX}{(X^2+4)^{\frac{1}{2}}} - Y\,\mathrm{atan}\frac{Y}{(X^2+4)^{\frac{1}{2}}}\right]\right\}, \tag{41}$$

where $A = \frac{a}{c}, B = \frac{b}{a}, X = A(1+B)$, and $Y = A(1-B)$ (Howell, 2018, factor C-12).

Example 1. Modeling the sensor as a square of edge length a = 2 cm at height c = 50 cm above a square target of edge length b = 400 cm (minimum size of square target in E1918) yields view factor $F_{1\to 2}$ = 0.951.

Example 2. Increasing the target edge length to 762 cm (size of square targets used in E1918 measurements by Levinson et al. 2014) raises $F_{1\to 2}$ to 0.986.

Example 3. Reducing the target edge length to 100 cm (typical size of square or nearly square masks used in E1918A) lowers $F_{1\to 2}$ to 0.554.

2.4.3 Differential plane element to parallel offset disc (pyranometer sensor to pyranometer shadow)

The view factor from a circular pyranometer sensor to its shadow is well approximated by that from a differential plane element to a parallel offset disc. If h is the distance between the plane of

the element and the plane of the disc and a is the offset between element and disc—that is, the distance in the plane of the disc from the center of the disc to the projection of the element's normal—the view factor from a plane element (surface $d1$) to the parallel offset disc of radius r (surface 2) is

$$F_{d1\to 2} = \frac{1}{2}\left[1 - \frac{Z - 2R^2}{(Z^2 - 4R^2)^{\frac{1}{2}}}\right], \tag{42}$$

where $H = \frac{h}{a}$, $R = \frac{r}{a}$, and $Z = 1 + R^2 + H^2$ (Howell, 2018, factor B-14).

Curve "to pyranometer shadow" in Figure 1 shows the application of Eq. (42) to compute as a function of solar altitude angle β the view factor from a sensor at height h = 50 cm over the center of a square target of edge length 400 cm to the pyranometer's shadow (radius r = 7.5 cm) on the target. Here the offset from sensor to center of shadow is $a = \frac{h}{\tan\beta}$, and the view factor is set to zero once the offset exceeds half the edge length. Note that all view factors reported in this study are dimensionless.

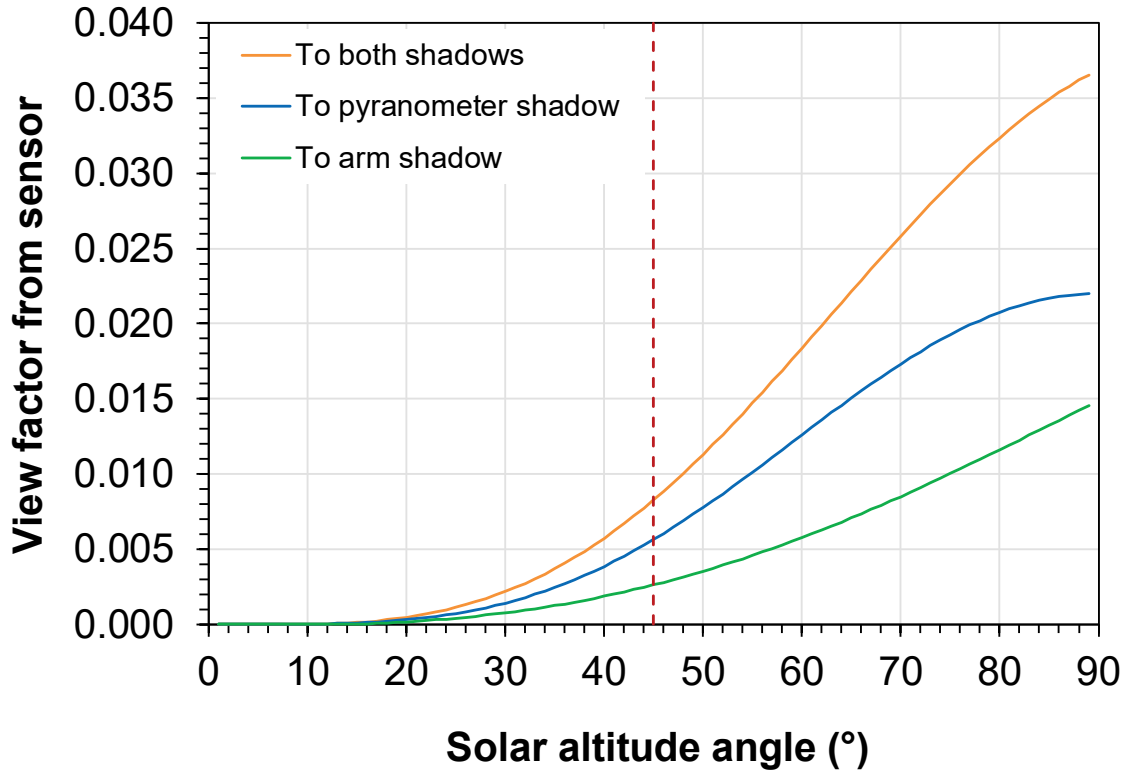

Figure 1. Variation with solar altitude angle of view factors to shadows from sensor of downward pyranometer 50 cm over the center of a square target of edge length 400 cm. Curves show view factors from sensor to 15 cm diameter pyranometer shadow on target, to 3 cm wide pyranometer support arm shadow on target, and to both shadows combined. Vertical line marks minimum solar altitude angle (45°) used in E1918/E1918A measurements on a horizontal target.

2.4.4 Pyranometer sensor to support arm shadow

Consider a differential plane element (surface $d1$) at height h above a differential coaxial ring of radius r parallel to the element (surface $d2$). The view factor from the element to the ring is

$$F_{d1\to d2} = \frac{2\,R\,dR}{(1+R^2)^2}, \tag{43}$$

where $R = r/h$ (Howell, 2018, factor A-5). The view factor from the element to a differential ring segment of arc length l (surface $d3$) is

$$F_{d1\to d3} = \frac{l}{2\,\pi\,r}\,F_{d1\to d2} = \frac{l}{2\,\pi\,r}\frac{2\,R\,dR}{(1+R^2)^2} = \frac{l}{\pi\,h}\frac{dR}{(1+R^2)^2}. \tag{44}$$

A segment that sweeps angle 2θ and has chord length $w = 2\,r\sin\theta$ will have arc length $l = 2\,r\,\theta$. If θ is small such that $\sin\theta \approx \theta$ and $l \approx w$,

$$F_{d1\to d3} = \frac{w}{\pi\,h}\frac{dR}{(1+R^2)^2}. \tag{45}$$

We model the downward-facing pyranometer sensor as a horizontal plane element (surface $d1$) at height h above its support arm's horizontal shadow (surface 4). If the rectangular shadow of constant width w extends from radius r_1 to radius r_2, the view factor from the sensor to the arm's shadow

$$F_{d1\to 4} = \int_{R_1}^{R_2} F_{d1\to d3}\,dR = \frac{w}{\pi\,h}\int_{R_1}^{R_2}\frac{dR}{(1+R^2)^2}, \tag{46}$$

where $R_1 = r_1/h$ and $R_2 = r_2/h$. Note that the assumption that θ is small fails as $r_1 \to 0$, so Eq. (46) will work best for shadows that are horizontally displaced from the sensor.

When $R_2 > R_1 \geq 0$,

$$F_{d1\to 4} = \frac{w}{2\,\pi\,h}\left[\frac{(R_2-R_1)(1-R_1R_2)}{(1+R_1^2)\,(1+R_2^2)} + \operatorname{atan}(R_2) - \operatorname{atan}(R_1)\right]. \tag{47}$$

Curve "to arm shadow" in Figure 1 shows the application of Eq. (47) to compute as a function of solar altitude angle β the view factor from at a sensor at height h = 50 cm over the center of a square target of edge length 400 cm to the support arm's shadow (width w = 3 cm). Here the shadow on the target extends from $r_1 = \frac{h}{\tan\beta}$ to r_2 = 200 cm (distance from center of target to edge of target).

2.5 Reflectance decrease induced by surface curvature or roughness

It is well known that a curved or rough surface reflects less radiation than a planar (perfectly flat) surface of the same composition because a photon reflected from a non-planar surface may return and be absorbed. Reflectometer method C1549 averages reflectance over an area about 3 cm², so

smaller-scale roughness is not an issue. However, of the four measurement techniques used in this study—C1549, E903, E1918, and E1918A—only the pyranometer methods E1918 and E1918A can determine the reflectance of larger areas, and these methods are less convenient for routine use than C1549. Thus we seek to use reflectances obtained from pyranometer and reflectometer measurement in the current study to improve our theoretical understanding of the relationship between the "macroscopic" reflectance of a curved or rough surface and the reflectance of a planar specimen of the same composition.

Berdahl et al. (2008) proposed a simple model that uses a single number, the area ratio, to represent surface roughness. This ratio is the area of the curved or rough surface, S_2 divided by the surface's plan view (footprint) area S_1. The probability p that a reflected photon will re-encounter the surface is estimated as

$$p = 1 - \eta^{-1}\,, \tag{48}$$

where area ratio $\eta = S_2\,/S_1$. In reality p varies over the surface, but we just regard its value as a constant that characterizes the entire surface. If the surface has macroscopic reflectance $\hat{\mathcal{R}}$ and planar reflectance $\mathcal{R}$, the reflectance decrease induced by curvature and roughness $\Delta\mathcal{R} \equiv \mathcal{R} - \hat{\mathcal{R}}$ is estimated as

$$\Delta\mathcal{R} = p\,\mathcal{R}\,\frac{1-\mathcal{R}}{1-p\,\mathcal{R}}. \tag{49}$$

Takebayashi et al. (2012) studied solar reflectance and heat transfer of traditional curved tile roofs popular in Japan. To simulate the effect of roughness they utilized a surface with V-shaped grooves. This shape does not closely mimic the tile shapes, but it has the advantage of being analytically solvable. In this special case Eqs. (48) and (49) above are exact. Takebayashi et al. also measured the temperature distributions across tile surfaces and within the roof assembly, and accounted for convective and conductive heat transfer as well as radiation. Thus, they obtained a good general picture of roof heat transfer.

Moore (2009) implemented a more accurate and complex technique for computing beam-hemispherical macroscopic reflectance from beam-hemispherical planar reflectance. His finite-element method represents the curved surface by a series of long thin parallel flat facets, assesses the availability of the source light at each facet; evaluates the radiative transfer between each pair of facets, and then solves a set of linear equations (one per facet) to find the flux absorbed by each facet and the macroscopic absorptance (1 - reflectance) of the curved surface. Within the assumption made (that the reflectance is fully diffuse), this method can be regarded as exact. Moore's method requires piecewise representation of the surface's shape, calculation of many view factors, and the simultaneous solution of a large set of equations. Still, it is more accurate than Berdahl's simple model, and therefore can determine the size of the errors of the simple model. If even more sophistication is needed, due to complex geometry or complex bi-directional reflectance function, Monte Carlo ray tracing techniques may be used (Howell, 1998).

Figure 2 shows how the reflectance decrease $\Delta\mathcal{R}$ varies with planar reflectance $\mathcal{R}$ according to the simple Berdahl model (upper curves) and more complex Moore model (lower curves) applied to

the four profiles analyzed by Moore (2009): high-profile tile, cosine, metal box rib, and standing seam (Figure 3). Results for the complex model were obtained from computations provided by Moore (2009). Both calculations yield curves that are nearly symmetric and parabolic, with the maximum displaced slightly to the right from $\mathcal{R} = 0.5$.

In general, the simple model performs well in comparison with the complex model in these four examples: The worst case is the standing seam roof, which is flat with vertical 2.5 cm fins at 30 cm intervals. For the standing seam roof, the maximum error is 0.009 whereas otherwise the largest error is 0.006. For the cosine profile, the largest error is 0.001; it is not clear why the error should be so small.

Why does the simple model tend to overestimate the magnitude of the adjustment required for surfaces that are not flat? The likely reason is the simplifying assumption that the probability p is a constant. Consider a surface A with area ratio $\eta_{\mathrm{A}} = 1.1$, and a second surface B with $\eta_{\mathrm{B}} = 1.3$, that have the same planar reflectance $\mathcal{R}$. Together the two surfaces, with equal footprint areas, make up a surface C with $\eta_{\mathrm{C}} = 1.2$. We can now evaluate the difference between the reflectance decrease $\Delta\mathcal{R}$ for surface C relative to the average decrease for surfaces A and B:

$$\delta = \Delta\mathcal{R}_{\mathrm{C}} - \frac{1}{2}(\Delta\mathcal{R}_{\mathrm{A}} + \Delta\mathcal{R}_{\mathrm{B}}) = \frac{\mathcal{R}(1-\mathcal{R})}{2}\frac{(\eta_{\mathrm{A}}-\eta_{\mathrm{B}})^2}{\eta_A\,\eta_{\mathrm{B}}\,(\eta_A+\eta_{\mathrm{B}})}\,. \tag{50}$$

Here the small term $p\,\mathcal{R}$ in the denominator of Eq. (49)has been temporarily omitted for the sake of simplicity. This equation shows that the use of a mean value of the area ratio rather than two distinct values increases the magnitude of the reflectance adjustment. Evaluating the value of the difference for $\mathcal{R} = 0.5$ we find $\delta = 0.0015$; including the full denominator, $\delta = 0.0010$. Evidently the simple model usually overestimates the reflectance loss, as is also illustrated by the four examples in Figure 2.

One other interesting example is provided by the metal box rib profile (Figure 2 and Figure 3). The top part of the surface is uppermost and is flat. Therefore, it has a return-to-surface probability $p = 0$ and a well-defined area. It does not exchange radiation with the rest of the surface. We can apply the simple model to the concave remainder of the surface. The resulting reflectance loss curve falls between the two curves in Figure 2c, an improvement over the simple model used by itself. Note that all reflectances and reflectance decreases reported in this study are dimensionless.

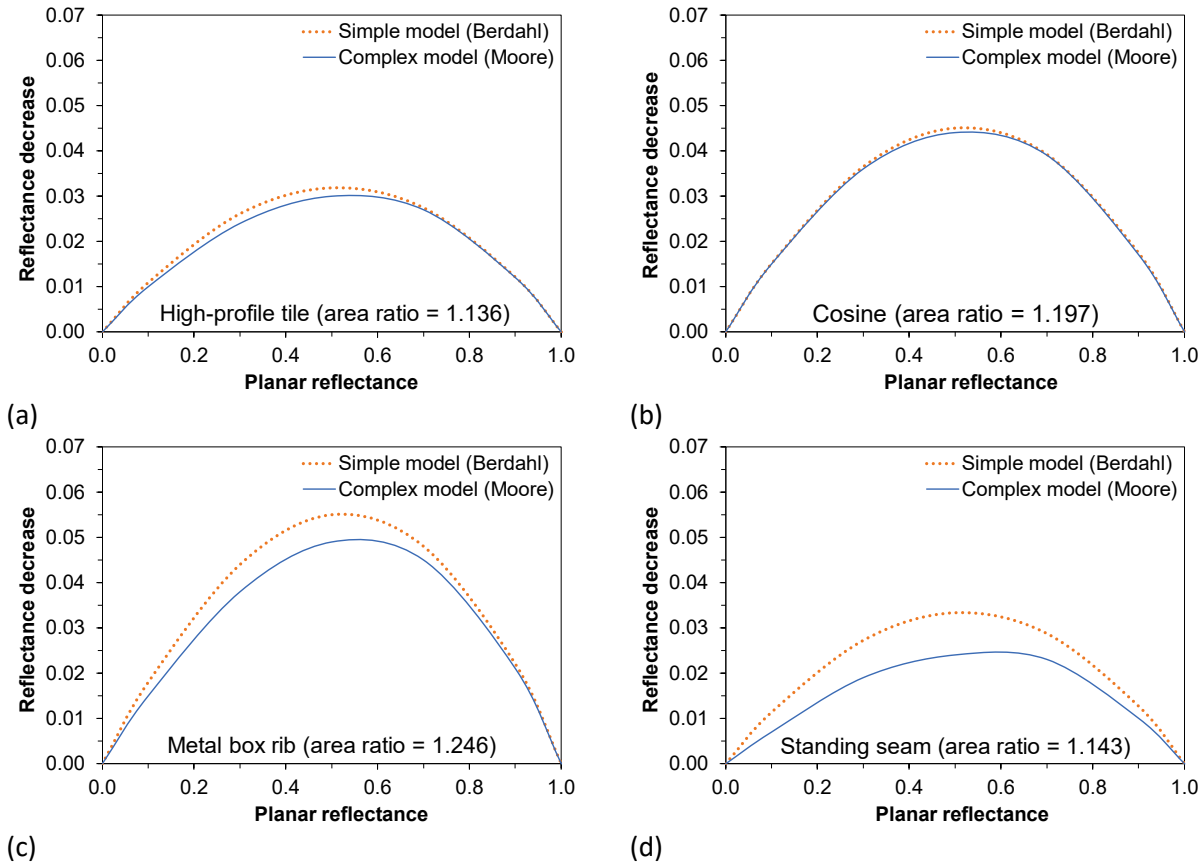

Figure 2. Reflectance decrease $\Delta\mathcal{R}$ (planar reflectance – macroscopic reflectance) as a function of the planar reflectance $\mathcal{R}$ for the four profiles specified in Moore (2009): (a) high-profile tile, (b) cosine, (c) metal box rib, and (d) standing seam. The upper dotted-orange curve in each panel is from the simple (Berdahl) model, while the lower solid-blue curve is from the complex (Moore) model.

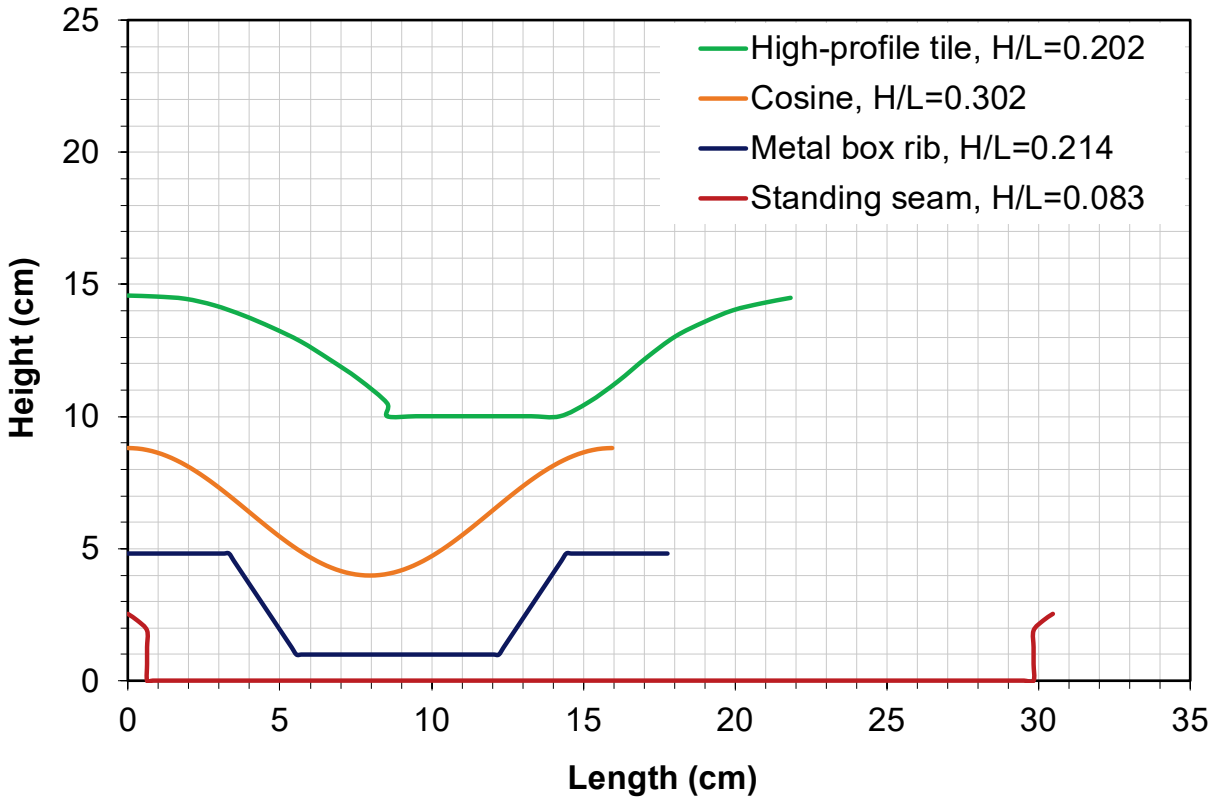

Figure 3. Four cross-sectional profiles analyzed by Moore (2009)—high-profile tile, cosine, metal box rib, and standing seam—with values of height-to-length ratio H/L shown in legend. Curves are vertically offset for clarity. Adapted from Moore (2009).

3 Experiment

3.1 Overview

The albedos of 10 roofing products were measured outdoors in accordance with E1918 and E1918A at an outdoor site in New River, AZ. The albedos of representative samples of these products were then measured indoors at Lawrence Berkeley National Laboratory (LBNL) following C1549 and E903.

3.2 Product selection

We acquired three single-ply membranes (membranes M1 – M3), one asphalt shingle (shingle S1), three roofing aggregates (aggregates A1 – A3), and three high-profile tiles (T1 – T3), each donated new by its manufacturer (Table 1; Figure 4). Detailed images of each product are shown in Electronic Supplementary Material (ESM) Figures A-1 through A-10.

Materials were supplied in quantities sufficient to prepare targets at least 4 m × 4 m for E1918 test. We held the following expectations for these 10 products:

1. The membranes would provide smooth, flat, and homogenous surfaces whose albedos could be accurately measured via C1549 and E903 and used to correct shadow and background errors present in E1918 measurements.

2. The granule-covered shingle would present a quasi-smooth, flat, and somewhat heterogeneous surface whose albedo could be accurately measured via the exhaustive sampling protocol specified in Procedure A of Appendix X1 of C1549, and by averaging E903 measurements performed at many spots.

3. The aggregates would let us further test the box-of-rocks exhaustive sampling protocol (Levinson et al., 2014, Method A) by comparing their mean C1549 albedos to the corrected E1918 albedos.

4. Comparing the C1549 and E903 albedos of flat or nearly flat tile chips to the corrected E1918 albedos of the corresponding high-profile tile assemblies would let us estimate the effect of concavity on reflectance, and assess the error induced by rating the albedo of a high-profile product based on that of a flat specimen.

5. Comparing C1549 and E903 albedos evaluated with various solar spectral irradiances (global or beam-only) to corrected E1918 measurements would help gauge the consequences of spectrum choice in C1549 and E903, supplementing earlier analysis by Levinson et al. (2010b).

Table 1. Details of products tested, including code, color/composition, description, representative albedo, spectral selectance, E1918 target size, numbers of C1549 and E903 measurement spots, and original code used during albedo measurements.

Product code	Color or composition	Description [a]	Repre-sentative albedo [b]	Spectral select-ance [c]	E1918 target size (cm × cm)	C1549 spots [d]	E903 spots [d]	C1549 spots (at Atlas) [e]	Original code [f]
Membrane M1	White	Single-ply PVC membrane	0.84	-0.07	424 × 419	3	3	3	1-1
Membrane M2	Gray	Single-ply PVC membrane	0.48	-0.04	406 × 399	3	3	3	1-2
Membrane M3	Blue	Single-ply PVC membrane	0.16	0.06	404 × 411	3	3	3	1-3
Shingle S1	Gray	Three-tab asphalt shingle	0.24	0.02	417 × 458	24	9	3	2-2
Aggregate A1	5/8” gray granite	Roofing aggregate	0.21	NA	403 × 403	25	NA	NA	3-1
Aggregate A2	3/8” white marble	Roofing aggregate	0.54	NA	403 x 403	25	NA	NA	3-2
Aggregate A3	1.5” multicolor ballast	Roofing aggregate	0.16	NA	403 x 403	25	NA	NA	3-3
Tile T1	White	Concrete S-tile (3.6”) [92 mm]	0.78	-0.01	>400 × >400 [g]	18	6	3	5-1
Tile T2	Orange	Clay S-tile (2.9”) [74 mm]	0.42	0.28	>400 × >400 [g]	16	14	3	5-2
Tile T3	Red	Concrete S-tile (3.0”) [76 mm]	0.24	0.13	>400 × >400 [g]	9	6	6	6-2

[a] Tile dimension shown is height. The complete dimensions of each tile are reported in ESM Figures A-11 to A-13 of ESM Appendix A.
[b] C1549_G1 albedo of flat or nearly flat specimen (membrane, shingle, tile) or “box of rocks” (aggregate) measured at LBNL.
[c] Defined as E903_AM1GH near-infrared reflectance – E903_AM1GH visible reflectance of flat or nearly flat specimen.
[d] Number of measurement spots used in C1549, C1549 Appendix X1 Procedure A, C1549 “box of rocks”, or E903 albedo measurement at LBNL.
[e] Number of measurements spots used in C1549 albedo measurement at Atlas performed with ORNL reflectometer.
[f] Original product code used during albedo measurements.
[g] The exact dimensions of the tile assemblies cannot be located, but each assembly exceeded a 400 cm × 400 cm boundary marked on its platform.

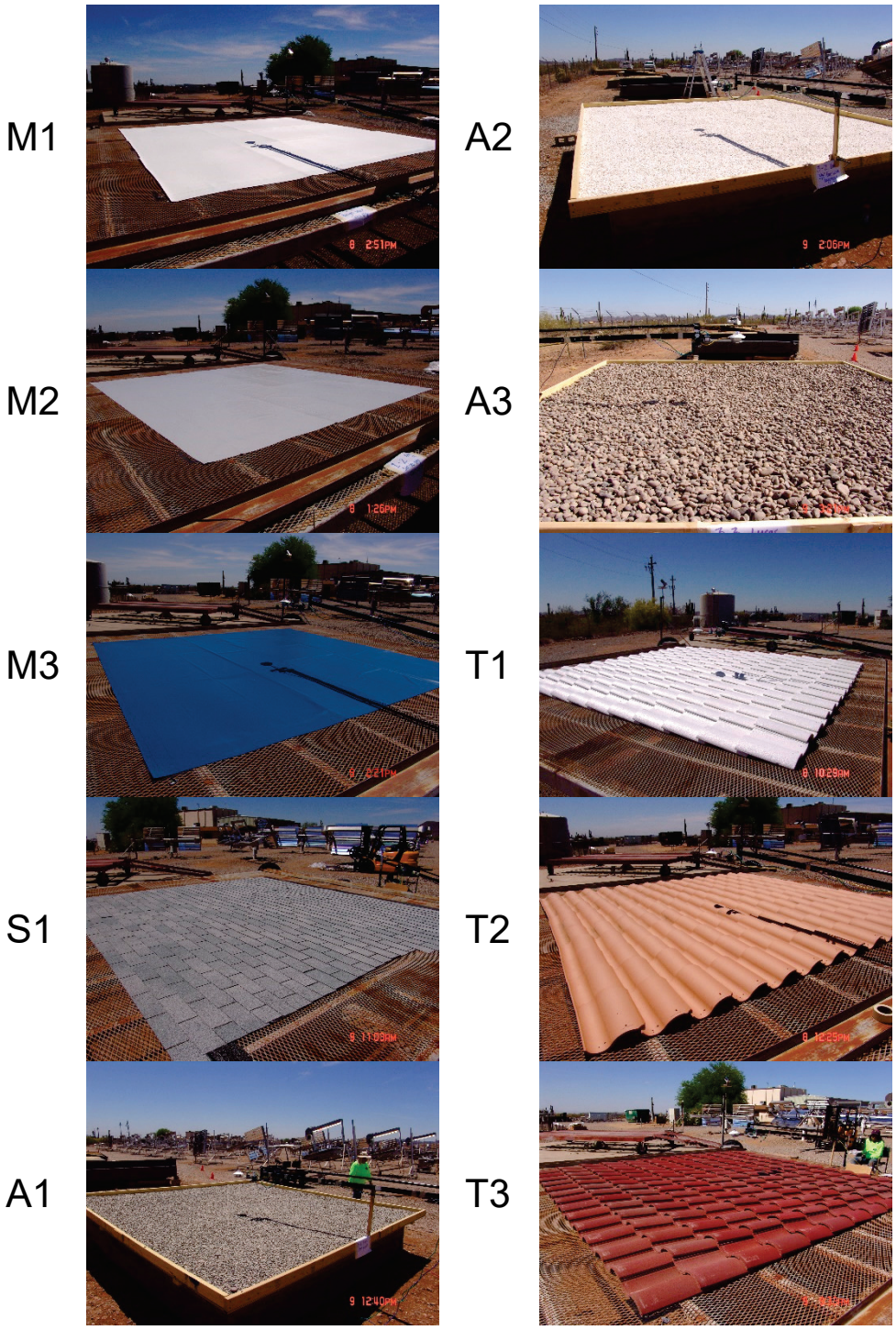

443 Figure 4. Images of membranes M1 – M3, shingle S1, aggregates A1 – A3, and tiles T1 – T3 as
444 assembled for E1918 trials.

3.3 Pyranometer measurement of albedo (E1918 and E1918A)

The E1918 and E1918A albedos of each product were measured on May 8 or 9, 2018 on the grounds of the Atlas Weather DSET Laboratory (Figure 5). The DSET Lab is in New River, AZ (33.898 °N, 112.158 °W), 52 km north of Phoenix. The site was chosen in expectation of clear skies and dry weather; the dates near the summer solstice were selected to obtain about 6 hours/day with the sun at least 45° above the horizon, while avoiding the hottest months in Arizona (June – August). Solar positions were computed with NREL's MIDC SOLPOS Calculator (National Renewable Energy Laboratory, 2018).

The DSET Laboratory provided time series of air temperature, relative humidity, wind speed, wind direction, and global tilt solar irradiance (5 °S) measured with the on-site weather sensors listed in Table 2. The weather station was 220 m west of the turntable shown in Figure 5.

Table 2. Weather and reflectance properties and apparata.

Property	**Apparatus**	**Notes**
Air temperature and relative humidity (weather)	Vaisala HMP50 temperature and relative humidity sensor	On DSET weather station, 3.0 m above ground.
Wind speed and direction (weather)	Gill Windsonic ultrasonic wind sensor	On DSET weather station, 2.1 m above ground.
Global tilt solar irradiance (weather)	Kipp & Zonen CMP22 secondary-standard pyranometer	On DSET weather station, 0.9 m above ground, tilted 5° S.
Downwelling and upwelling global horizontal solar irradiance (E1918/E1918A)	Kipp & Zonen CMA6 first-class albedometer with two Kipp & Zonen Meteon display meters	Factory calibrated on 2018-04-28; supported on Advanced Digital 12' (3.7 m) camera crane.
Pyranometer roll and pitch angle (E1918/E1918A)	Machine-DRO digital angle gauge with remote display, one for roll and one for pitch,	Mounted on CMA6 support rod. These sensors supplement the circular bubble level on the CMA6.
Reference reflectances for E1918A	TAP Plastics HDPE sheets (masks), one white and one black	Each 1 m² sheet is 91.4 cm × 109 cm × 0.8 mm.
Solar reflectance (C1549)	Devices & Services Solar Spectrum Reflectometer version 6	Measurements at LBNL performed with instrument #081; those at Atlas performed with instrument #078 on loan from ORNL.
Solar spectral reflectance (E903)	PerkinElmer Lambda 900 UV-vis-NIR spectrometer with Labsphere 150 mm integrating sphere	At LBNL.

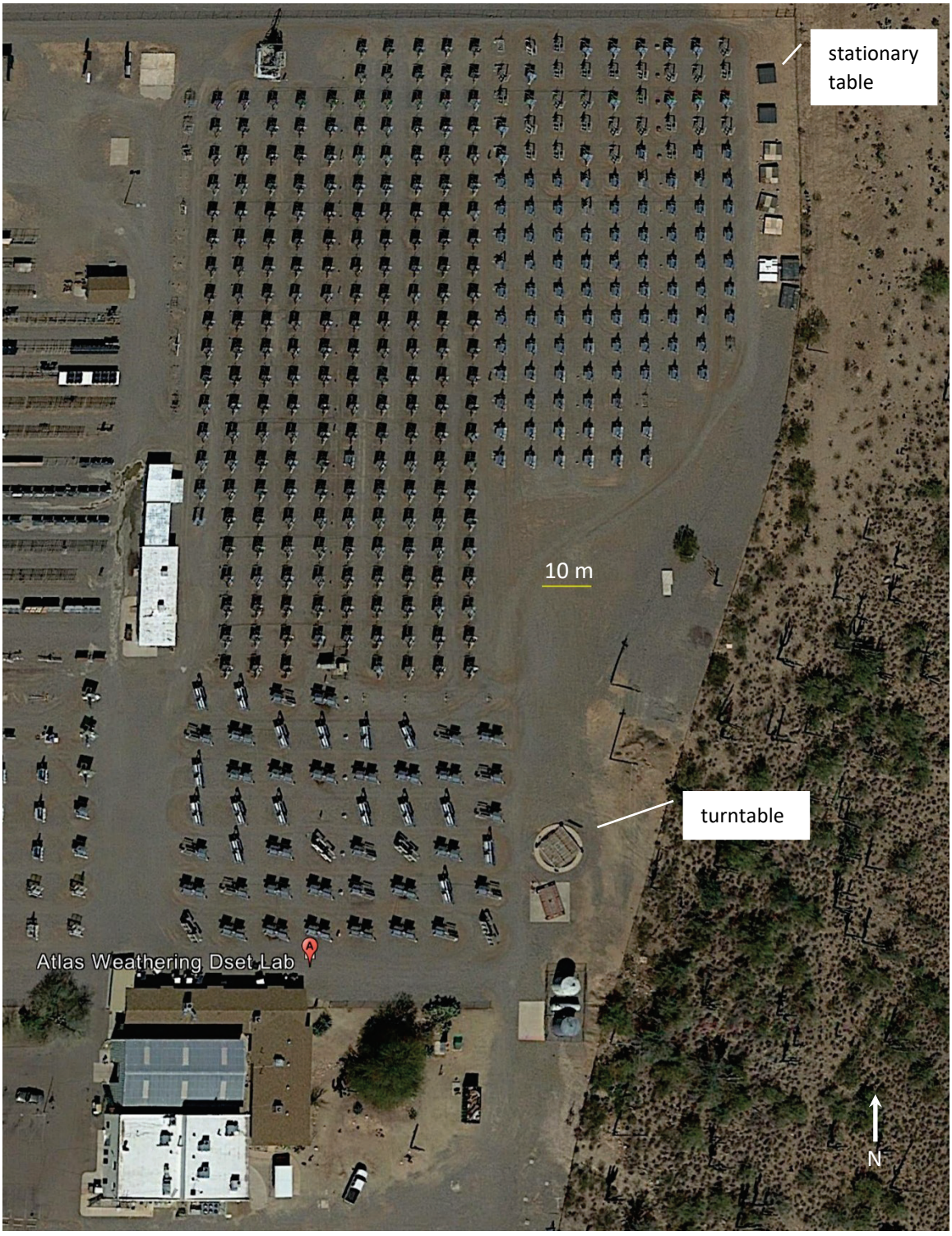

Figure 5. Atlas Weathering DSET Lab site image locating turntable used for E1918/E1918 measurement of membrane, shingle, and tile albedo, and stationary table used for E1918/E1918 measurement of aggregate albedo. Image source: Google Earth.

Roofing contractors assembled the E1918/E1918A test specimens on large platforms. The dimensions of each E1918 test specimen are listed in Table 1.

Each membrane, shingle, and tile product was assembled on an 6.1 m × 6.1 m horizontal metal turntable whose surface was 76 cm above ground (ESM Figure B-9a). Shingles, tiles, and membranes were overlapped in the manner customary to each product, but were not attached to the platform, battens, or each other (panel *a* in ESM Figures A-1 to A-4 and A-8 to A-10). The complete dimensions of each tile are reported in ESM Figures A-11 to A-13 of ESM Appendix A.

Each aggregate was poured one at a time into a wooden box ("stationary table") with 8.9 cm high vertical walls and a horizontal surface 61 cm above ground (ESM Figure B-9b). The aggregate was then smoothed to form a layer about 2 – 3 cm deep (aggregates A1 and A2; ESM Figures A-5 and A-6) or 4 – 5 cm deep (aggregate A3; ESM Figure A-7). The aggregate was not adhered to the bottom of the table. The stationary table was emptied and swept before installing the next product.

The E1918/E1918A albedos of the membranes, shingle, and aggregates were measured in a single azimuthal orientation (ESM Figures B-3 to B-5), while those of the tile assemblies were measured in two orientations: once with the tile ridges parallel to the horizontal projection of the solar beam, and again with the ridges perpendicular to this projection (ESM Figures B-1 and B-2).

The E1918 and E1918A measurements were performed with a first-class albedometer—back to back first-class pyranometers, each with its own display meter—flown 50 cm over the center of each 4 m × 4 m target by a 3.7 m (12 ft) camera crane (Figure C-5). The 95% response time of this albedometer is less than 18 s (Kipp & Zonen, 2016).

Digital levels with remote displays were attached to the pyranometer's support rod to measure the instrument's roll and pitch and verify that it was horizontal. (The circular bubble level on the top of the albedometer was also used for this purpose.) Black and white HDPE sheets, each 1 m², were used as masks in E1918A (Table 2).

Three E1918A trials were performed successively for each target. Within each E1918A trial, the downwelling (incident) and upwelling (reflected) radiances were recorded simultaneously in three configurations: (1) white mask over black mark over center of 4 m × 4 m test specimen; (2) black mask only over center of specimen; and (3) specimen bare. The upwelling radiances measured in in configurations 1 – 3 were used to compute E1918A albedo in accordance with Eq. (24), while the upwelling and downwelling radiances measured in configuration 3 were used to calculate E1918 albedo following Eq. (1).

The C1549 albedos of the masks were measured at Lawrence Berkeley National Laboratory before and after the E1918/E1918A trials in Arizona (Table 3). The pre-trial air mass 1 global horizontal (AM1GH) C1549 albedo (SSR output "G1") was used as the true albedo of each mask (black) or mask sandwich (white over black).

Methods E1918 and E1918A work best if the test specimens and (for E1918A) masks diffusely reflect sunlight to the downward-facing pyranometer. The membranes, white tile (T1), and masks were slightly glossy. However, we assessed through laboratory measurements detailed in Sections 3.6 and 4.2.2 that their directional-specular solar reflectances are likely quite small (< 0.02) at incidence angles up to 45°, the range allowed by E1918 and E1918A.

Table 3. C1549 albedos of E1918A masks before and after trials.

	Black, G1	White over black, G1	Black, 1.5E	White over black, 1.5E	Black, 1.5E – G1	White over black, 1.5E – G1
Before trials	0.050	0.782	0.049	0.805	-0.001	0.023
After trials	0.053	0.778	0.053	0.802	0.000	0.023
After – before	0.003	-0.004	0.004	-0.003	0.001	0.001

3.4 Reflectometer measurement of albedo (C1549 and variants)

3.4.1 Measurements at LBNL

Three coupons (about 300 – 400 cm²) cut from each membrane and shingle product (panel *b* in ESM Figures A-1 to A-4) and about 10 kg of each aggregate tested in the E1918/E1918A trials were transported to LBNL for C1549 albedo measurement. Each aggregate product was poured into a small cardboard frame on a black tabletop to create a 15 cm × 15 cm "box of rocks" (panel *b* in ESM Figures A-5 to A-7) in accordance with Method A of Levinson et al. (2014). About a month after the E1918/E1918A trials, the manufacturer of each tile product sent to LBNL at least six replicate coupons ("chips") of each tile product. The tile T1 and tile T3 chips were 8 cm × 8 cm and flat, while the tile T2 chips were 10 cm × 10 cm and slightly convex, with an outer curvature radius of 12.5 cm (panel *b* in ESM Figures A-8 to A-10).

C1549 albedos were measured with version 6 of the Devices & Services Solar Spectrum Reflectometer (Dallas, TX). The albedo of each membrane (M1 – M3) was measured at three spots with the SSR in accordance with C1549, while the albedo of the shingle (S1) was measured at 24 spots with the SSR in accordance with Procedure A in Appendix X1 of C1549. The albedo of each aggregate (A1 – A3) was measured at 25 spots with the SSR in accordance with Method A of Levinson et al. (2014) (equivalent to Procedure A in Appendix X1 of C1549). The albedo of the tile T1, tile T2, and tile T3 chip sets were measured at 18, 16, and 9 spots with the SSR; the number of measurements per chip set, each well in excess of the 3 spots required by C1549, was guided by the degree to which albedo varied from spot to spot and chip to chip. ESM Figure B-6 shows C1549 measurements performed on membrane, shingle, convex tile, and flat file specimens, while ESM Figure B-7 shows C1549 measurements performed on boxes of roofing aggregates.

The SSR's "G1" albedo output corresponding to air mass 1 global horizontal, or AM1GH, solar spectral irradiance (Levinson et al., 2010a, 2010b), and its "1.5E" albedo output, corresponding to the ASTM Standard E891 Beam Normal, or E891BN, solar spectral irradiance at air mass 1.5(ASTM International, 1992), were recorded in the course of each spot measurement. C1549_G1 (AM1GH) albedo is designed to well represent the solar reflectance of a horizontal or low-sloped

terrestrial surface, while C1549_1.5E (E891BN) albedo was designed to represent the solar reflectance of a surface that receives only beam (direct) sunlight. The E891BN power spectrum (2.9% ultraviolet, 300 – 400 nm; 39.0% visible, 400 – 700 nm; and 58.1% near-infrared, 700 – 2,500 nm) is richer in near-infrared light than the AM1GH power spectrum (6.6% ultraviolet, 44.7% visible, and 48.7% near-infrared). AM1GH albedo better suits roofs, which on a clear day receive both beam and diffuse sunlight (Levinson et al., 2010a, 2010b). However, the C1549_1.5E albedo reported by version 6 of the SSR, or the equivalent C1549_1.5 albedo reported by version 5 of the SSR, has been used to rate the albedo of every product listed in the Rated Products Directory of Cool Roof Rating Council (Cool Roof Rating Council, 2018b).[3]

Because the tile T2 chip was convex, we made an additional measurement of its C1549 albedo following Devices & Services Technical Note 11-1: SSR-ER Reflectance Measurements for Large Radius Cylindrical Surfaces (Moore, 2010). This procedure estimates the albedo that would be obtained if the test surface were flat, rather than convex. The increase in albedo predicted by this additional measurement was 0.010 (C1549_G1) or 0.012 (C1549_1.5E). We round this increase to 0.01 for either albedo metric.

C1549 albedos reported in this paper as "C1549_G1" or "C1549_1.5E" are those measured with the LBNL reflectometer at LBNL.

3.4.2 Measurements at Atlas

Anticipating possible color and albedo differences between the tiles used in the large assemblies and their chips yet to be received, we measured the C1549 albedos of the membrane, shingle, and tile products during the experiment at the Atlas facility for comparison with C1549 albedo measurements to be performed at LBNL.

C1549 measurements at Atlas were performed indoors using a second reflectometer—the same make and model as that at LBNL—loaned by Oak Ridge National Laboratory (ORNL). The membrane and shingle coupons tested with the ORNL reflectometer were those later sent to LBNL. The tiles tested with the ORNL reflectometer were selected to represent the tile assemblies. We used one tile for T1 and one tile for T2 because the T1 and T2 assemblies were each uniform in color. We selected two tiles—one reddish, one brownish—to represent T3 and averaged their albedos because we observed minor tile-to-tile variations in color within the T3 assembly. Measurements were made on the flattest available portions of the convex upper surface of each tile.

[3] As of December 2018, all solar reflectances reported in this directory were obtained with the solar spectrum reflectometer following ASTM C1549 (three-point measurement) or its variants, such as CRRC Test Method #1 (random sampling of at least 30 points) or the Template Method (systematic measurement at 54 points), following ANSI/CRRC S100 (2016): Standard Test Methods for Determining Radiative Properties of Materials (Cool Roof Rating Council, 2016). ANSI/CRRC S100 (2016) specifies use of the air mass 1.5 beam-normal solar reflectance output of the reflectometer, called "C1549_1.5E" in this paper.

C1549 albedos reported in this paper as "C1549_G1_ORNL" or "C1549_1.5E_ORNL" at those measured with the ORNL reflectometer at Atlas.

3.4.3 Correction of tile chip albedo

We generated "corrected" C1549 albedos (C1549_G1_cor, C1549_1.5E_cor) for the three tile chips to compare to the corrected E1918 albedos (E1918_cor) of the three tile assemblies. The corrected C1549 albedo of a tile chip—that is, the C1549 albedo expected for a planar sample of the assembly tile if measured with the LBNL reflectometer—was obtained by adding two terms to the C1549 tile albedo measured with the ORNL reflectometer: the curvature adjustment of 0.01 obtained in Section 3.4.1 and an instrument adjustment of 0.007 (C1549_G1) or 0.004 (C1549_1.5E). The instrument adjustment was the mean difference in C1549 albedo (LBNL – ORNL) reported by the two reflectometers for the membranes and shingle.

No adjustments to the C1549 albedos of the membranes, shingle, or aggregates measured at LBNL were required because the membrane, shingle, and aggregate specimens tested at LBNL were collected from the assemblies tested at Atlas. For these seven products C1549_G1_cor = C1549_G1 (LBNL) and C1549_1.5E_cor = C1549_1.5E (LBNL).

3.5 Spectrophotometer measurement of albedo (E903)

E903 albedos of the membrane coupons, shingle coupon, tile chips, and masks were measured at LBNL with a PerkinElmer Lambda 900 UV-vis-NIR spectrometer fitted with a 150 mm Labsphere integrating sphere. Solar spectral reflectance was measured at three spots on each membrane (M1 – M3), nine spots on the shingle (S1), six spots on each flat tile chip (T1 and T3), 14 spots on the convex tile chip (T2), and 3 spots on each mask. ESM Figure B-8 shows membrane and tile specimens at the reflectance port of the integrating sphere. E903 albedos were not measured for the aggregate products because there is no procedure to measure the reflectance of an aggregate pile with this apparatus.

Each solar spectral reflectance was measured from 300 to 2,500 nm at an interval of 5 nm. E903_AM1GH and E903_E891BN albedos were computed by averaging solar spectral reflectance weighted with the corresponding solar spectral irradiance. Irradiance-weighted broadband reflectances were also computed for the ultraviolet , visible, and near-infrared spectra.

3.6 Spectrophotometer measurement of specular reflectance

The solar spectral directional-specular reflectance at 8° incidence of each non-aggregate specimen and each mask was determined by subtracting its reflectance measured with the sphere's specular port open from that measured with the port closed. Since the first-surface reflectance of unpolarized beam light passing from air (real refractive index 1) to a polymer of real refractive index 1.5 at 8° incidence is 0.040 and that at 45° incidence is 0.050 (Georgia State University, 2019), we estimate that that ratio of specular reflectance at 45° incidence to that at 8° incidence will not exceed 0.050 / 0.040 = 1.25.

4 Results and discussion

4.1 Pyranometer measurement of albedo (E1918 and E1918A)

4.1.1 Weather and solar position

Panels (a) – (c) of Figure 6 show the global tilt solar irradiance (5 °S), windspeed, and air temperature time series on May 8 and 9, 2018. The vertical lines in these plots mark the midpoint of each products E1918/E1918A trials. Suffixes "a" and "b" after each tile code (e.g., T1a, T2b) indicate that tile ridge was oriented (a) parallel or (b) perpendicular to the horizontal projection of the solar beam.

Hazy or patchy skies should be avoided during E1918/E1918A measurements (ASTM International, 2016a). The sky was sunny and generally clear during all tests on May 8 and for the first four tests on May 9 but turned cloudy around 13:00 local standard time (LST) on May 9. This hindered E1918/E1918A measurements on the last two products (aggregates A2 and A3). Wind gusts (Figure 6b) occasionally dislodged the E1918A masks, requiring repetition of some trials on each day. [4] We suggest that researchers attach thin weights, such as flat iron brackets, to the back of the masks for ballast.

High air temperatures (up to 38 °C, or 100 °F) combined with strong sun (up to 1 kW/m²) made the black mask dangerously hot to touch. We minimized contract with this mask by repositioning both the black and white masks with a mechanical "grabber arm" that we had brought to reach the center of a 4 m × 4 m specimen without walking on it. It was also necessary to frequently rehydrate and move out of the sun. The latter was a challenge during E1918A trials, which required continuous addition and removal of the masks.

Figure 6d shows the solar altitude angle time series. All measurements except those for the final product tested, aggregate A3, were performed when the solar altitude angle was at least 45°. The solar altitude angle fell to about 43° during the A3 tests, which were delayed by cloudy and windy weather.

[4] Note that the wind speed was measured at 3 m above ground, while the test specimens were about 0.5 to 1 m above ground. The wind speeds were lower at specimen level.

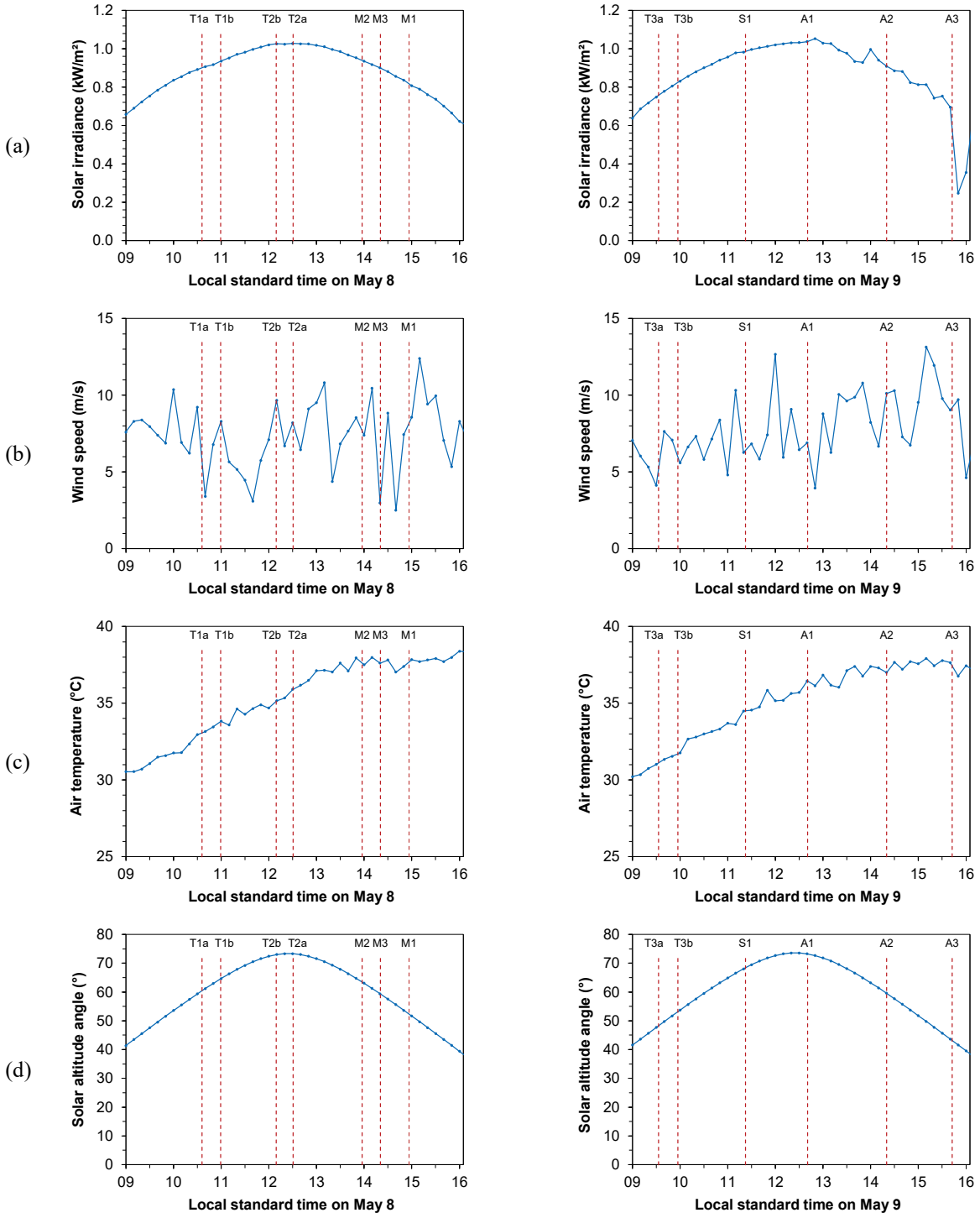

623 Figure 6. Environmental conditions during E1918/E1918A trials, including (a) global tilt solar
624 irradiance (5° S) measured 0.9 m above ground level; (b) wind speed measured 3.0 m above
625 ground level; (c) dry-bulb air temperature measured 2.1 m above ground level; and (d)
626 computed solar altitude angle. Vertical lines mark midpoint of each product's trial set. Suffix
627 a/b indicates tile ridge was parallel/perpendicular to horizontal projection of solar beam.

4.1.2 Albedos

The orientation of each tile assembly had minimal effect on its E1918 and E1918A albedos (Figure 7 and Figure 8), with absolute changes not exceeding 0.005 and 0.014, respectively. Therefore, we averaged each tile assembly's parallel and perpendicular results to obtain its representative E1918 and E1918A albedos.

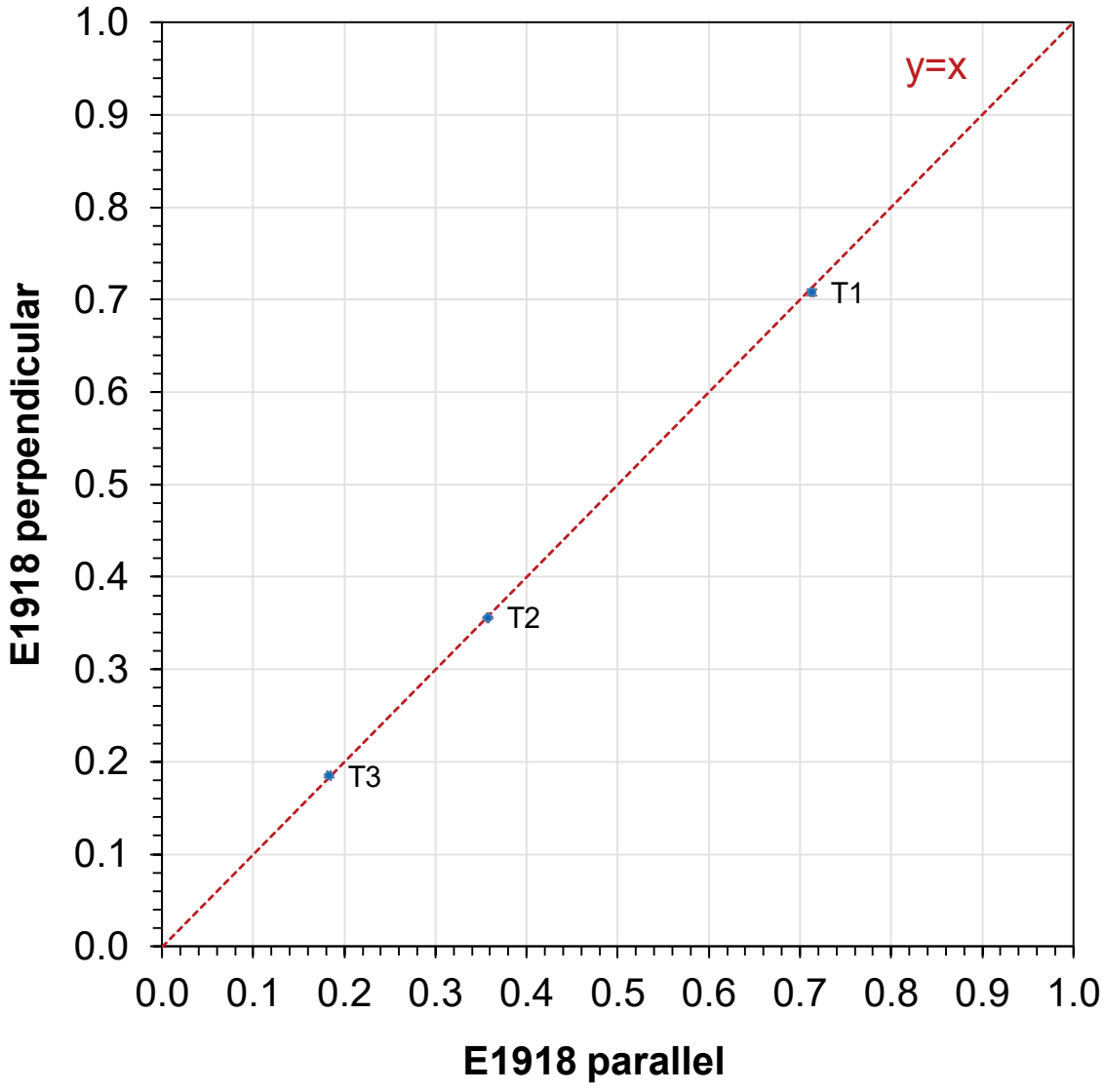

Figure 7. E1918 perpendicular albedo (tile ridge perpendicular to horizontal projection of solar beam) vs. E1918 parallel albedo (tile ridge parallel to horizontal projection of solar beam) for tiles T1 – T3. Error bars on all plots mark ± 1 standard deviation.

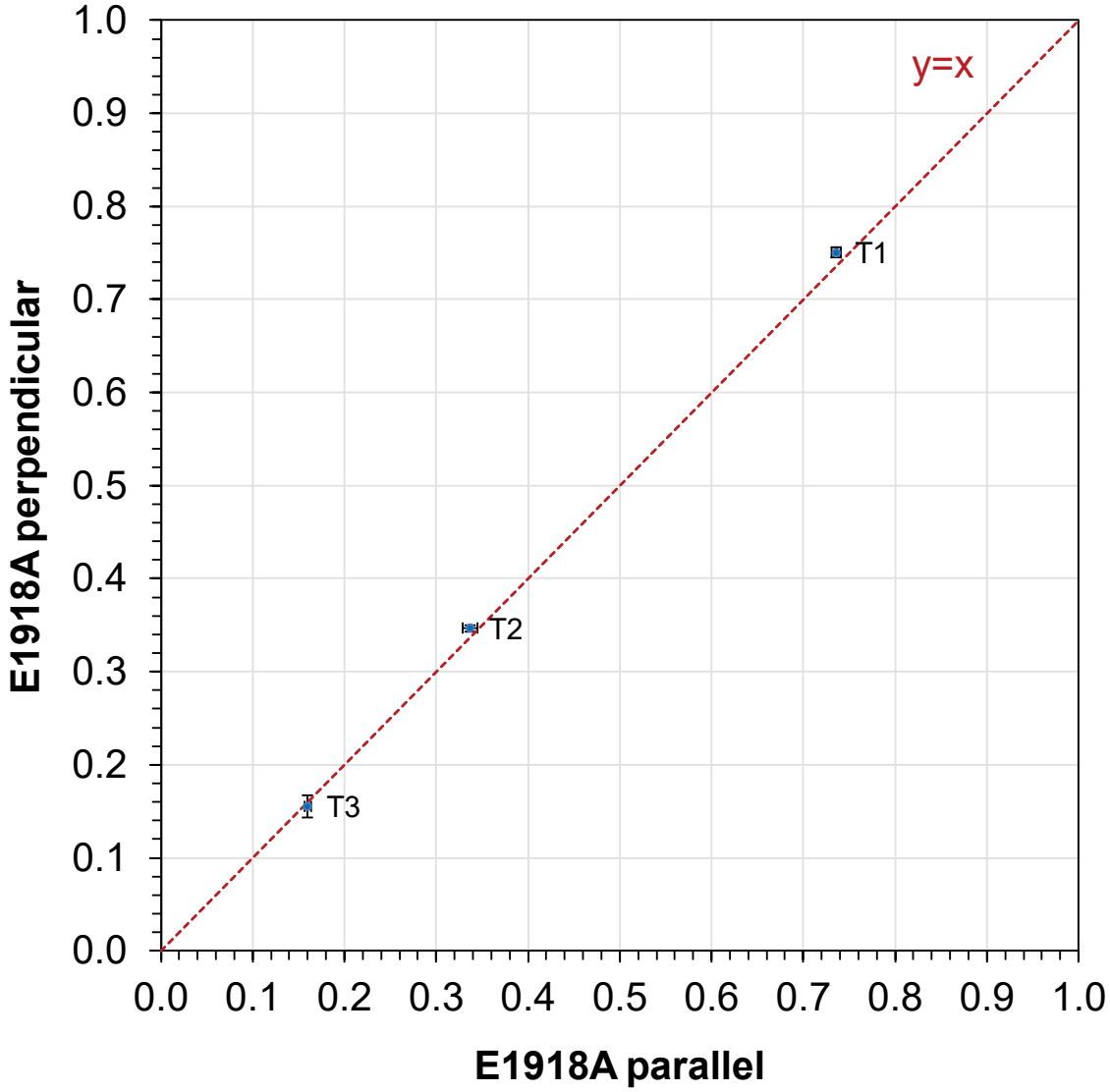

637

638 Figure 8. E1918A perpendicular albedo vs. E1918A parallel albedo for tiles T1 – T3.

639 E1918A albedos of the more reflective products—those with E1918A albedos above 0.40—tended
640 to exceed E1918 albedos of these products (Figure 9), supporting the theory of shadow and
641 background errors. [Such errors affect E1918 but have little influence on E1918A; see Levinson
642 et al. (2010b)].

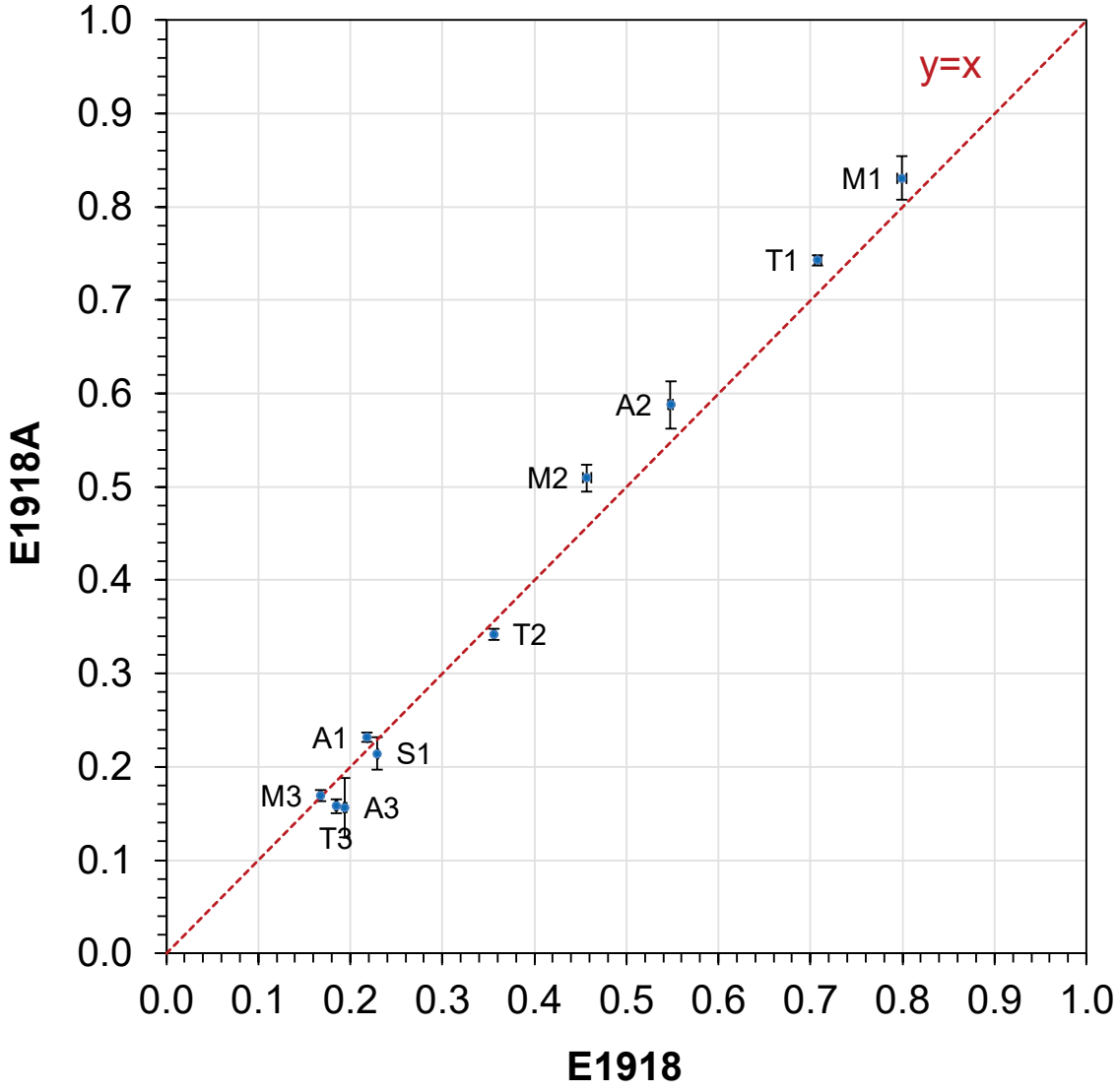

Figure 9. E1918A albedo vs. E1918 albedo for all products. E1918 and E1918A values for tiles on this and subsequent plots average the ridge-parallel and ridge-perpendicular measurements.

To correct these errors, we linearly regressed the E1918 albedos of the three membranes to their C1549_G1 "true" albedos (Figure 10). This yielded coefficients $a = 0.930$ and $b = 0.017$ in Eq. (4) with coefficient-of-determination $R^2 = 0.9998$. Using the sensor-to-target view factor $F_{1\to2} = 0.951$ for a 4 m × 4 m target computed in Section 2.4.2 and assuming that 15% of global horizontal solar irradiance is diffuse ($\phi = 0.15$), we obtain sensor-to-target shadow view factor $F_{1\to2s} = 0.025$ from Eq. (16) and background albedo $\rho_3 = 0.35$ from Eq. (17). The experimentally derived value $F_{1\to2s} = 0.025$ is slightly higher than the geometrically computed range of $F_{1\to2s} = 0.013 - 0.021$ shown in curve "to both shadows" in Figure 1. The computed range corresponds to the solar altitudes 52° to 64° encountered during the membranes' E1918 trials (a). The background albedo (0.35) is higher than the 0.20 typically assumed for ground surfaces, but the rusted metal turntable

supporting the membrane, shingle, and tile specimens and the surrounding ground were reddish. This suggests the presence of red iron oxide, a "cool colorant" that often exhibits high near-infrared reflectance (Levinson et al., 2005).

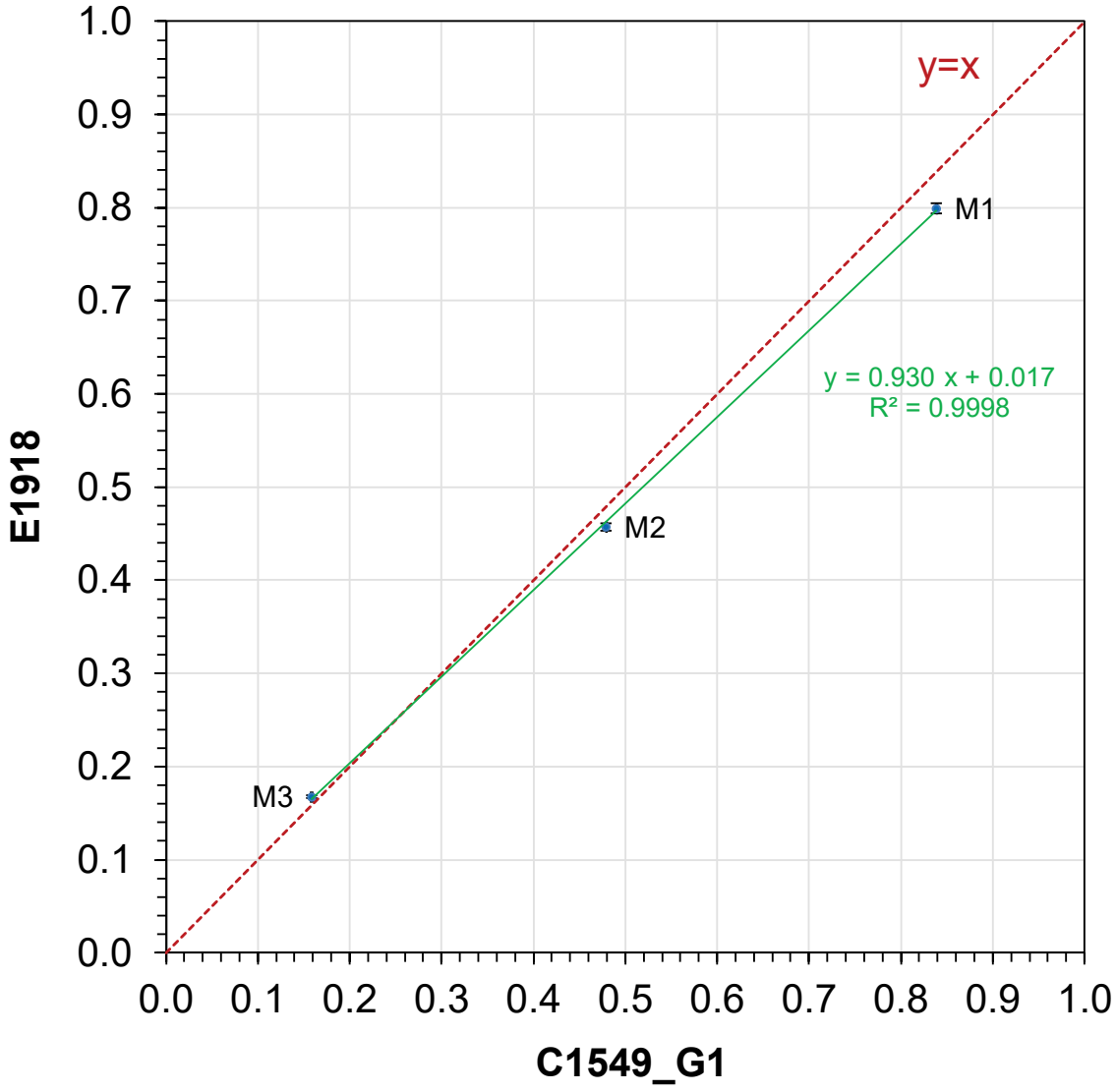

Figure 10. E1918 albedo vs. C1549_G1 (SSR output G1) albedo for membranes M1 – M3.

The coefficients obtained from the membrane albedo regression were then substituted into Eq. (7) to compute the E1918 corrected (E1918_cor) albedo for all products (Figure 11). The agreement between E1918A and E1918_cor (Figure 12) is closer than that between E1918A and E1918 (Figure 9).

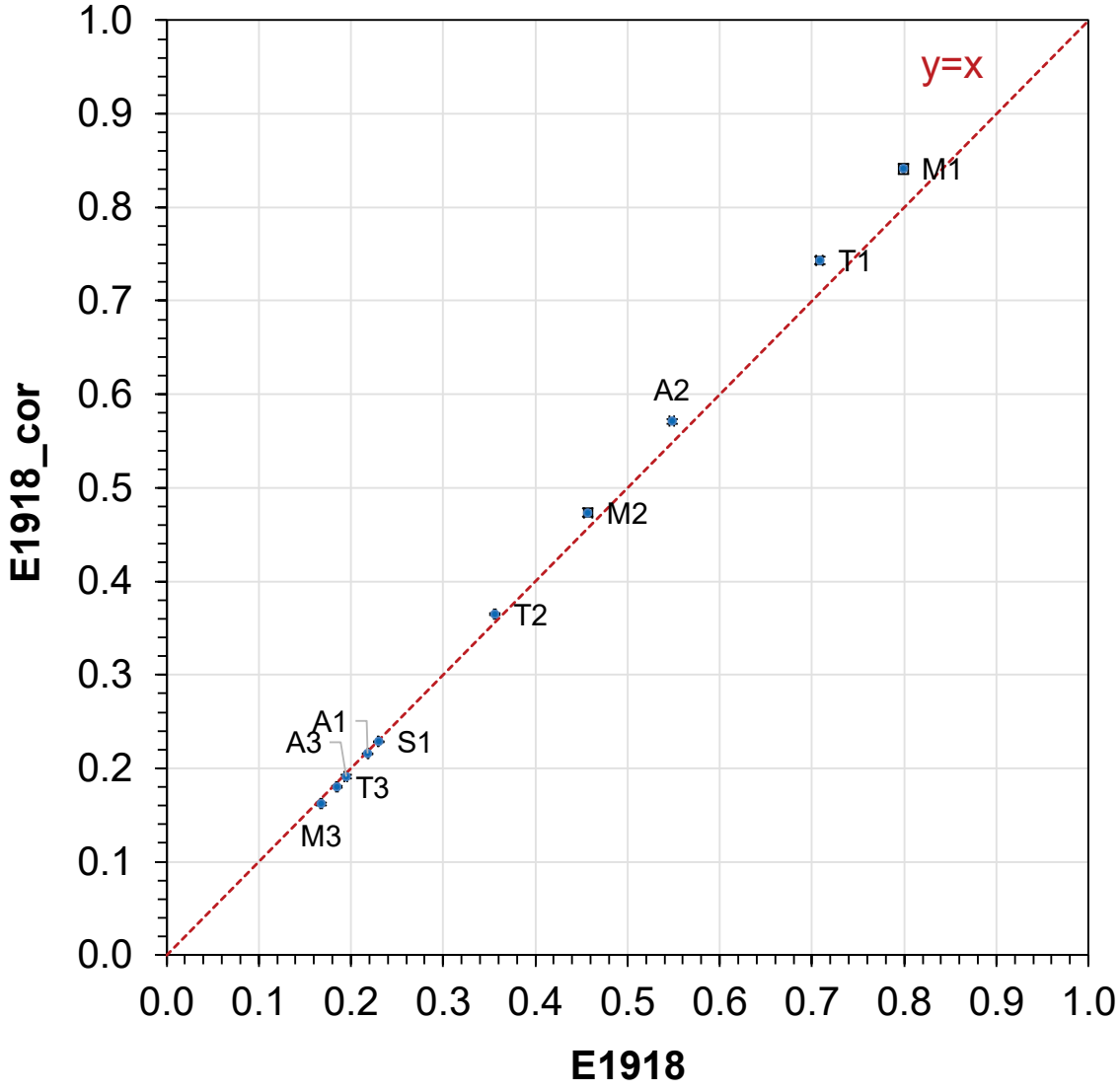

665

666 Figure 11. E1918_cor (E1918 corrected) albedo vs. E1918 albedo for all products.

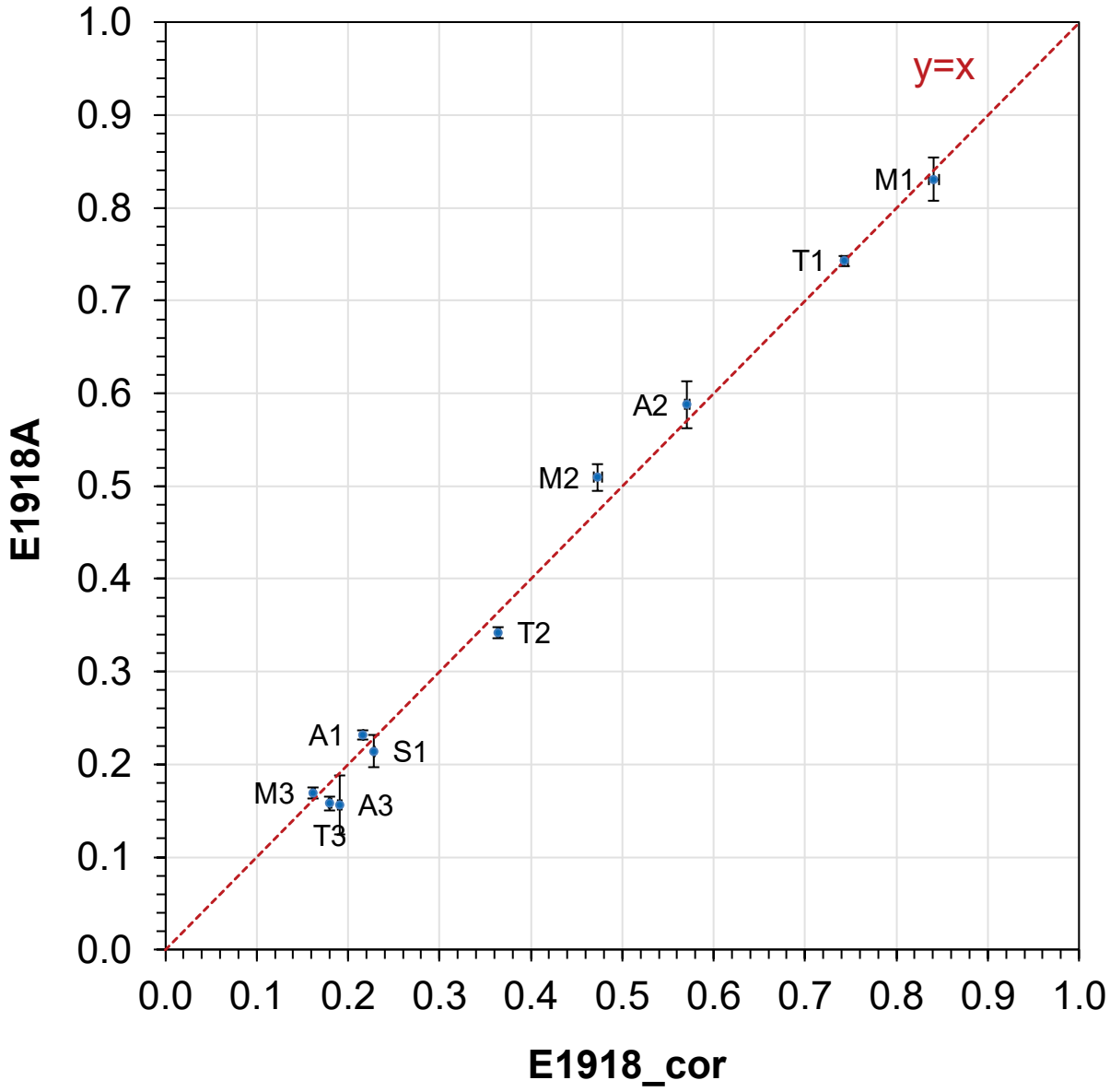

Figure 12. E1918A albedo vs. E1918_cor (E1918 corrected) albedo for all products.

The first three rows Table 4a-c and the first three bars in each panel of Figure 13 detail the mean and standard deviation of each product's E1918, E1918_cor, and E1918A albedos. The maximum absolute difference between E1918A and E1918_cor (0.036) was smaller than that between E1918A and E1918 (0.052) (Table 4d). As explored in Section 2.3.2, E1918A is more susceptible than E1918 to random errors in pyranometer measurement of irradiance because the view factor from the downward-facing pyranometer to the target in E1918A (about 0.55) is only about 58% that to the target in E1918 (about 0.95).

Table 4. E1918, E1918_cor, E1918A, C1549_G1, E903_AM1GH, C1549_1.5E, E903_E891BN, C1549_G1_ORNL, C1549_1.5E_ORNL, C1549_G1_cor, and C1549_1.5E_cor albedos, and the differences between selected albedo metrics, shown for (a) membranes M1 – M3 and shingle S1, (b) aggregates A1 – A3, and (c) tiles T1 – T3. Subtable (d) shows the range of difference between albedo metrics for each group (a, b, and c). Uncertainties in albedo differences assume that the uncertainties (standard deviations) in albedos are uncorrelated. Value "NA" (not available) indicates that the measurement was not made.

(a)

	Membrane M1 (white)	**Membrane M2 (gray)**	**Membrane M3 (blue)**	**Shingle S1 (gray)**
Mean (standard deviation)				
E1918	0.799 (0.005)	0.457 (0.004)	0.168 (0.001)	0.230 (0.001)
E1918_cor	0.841 (0.006)	0.473 (0.005)	0.162 (0.002)	0.229 (0.001)
E1918A	0.831 (0.023)	0.509 (0.015)	0.169 (0.006)	0.214 (0.017)
C1549_G1	0.839 (0.001)	0.479 (0.001)	0.159 (0.001)	0.243 (0.007)
E903_AM1GH	0.848 (0.001)	0.481 (0.000)	0.155 (0.000)	0.239 (0.016)
C1549_1.5E	0.878 (0.001)	0.495 (0.001)	0.163 (0.001)	0.253 (0.008)
E903_E891BN	0.870 (0.001)	0.492 (0.000)	0.160 (0.000)	0.247 (0.016)
C1549_G1_ORNL	0.830 (0.001)	0.475 (0.000)	0.153 (0.000)	0.234 (0.009)
C1549_1.5E_ORNL	0.873 (0.001)	0.491 (0.001)	0.154 (0.000)	0.254 (0.002)
C1549_G1_cor	0.839 (0.001)	0.479 (0.001)	0.159 (0.001)	0.243 (0.007)
C1549_1.5E_cor	0.878 (0.001)	0.495 (0.001)	0.163 (0.001)	0.253 (0.008)
Difference (uncertainty)				
E1918 – E1918_cor	-0.042 (0.008)	-0.016 (0.006)	0.006 (0.002)	0.001 (0.001)
E1918A – E1918	0.032 (0.024)	0.052 (0.015)	0.001 (0.006)	-0.016 (0.017)
E1918A – E1918_cor	-0.010 (0.024)	0.036 (0.016)	0.007 (0.006)	-0.015 (0.017)
C1549_G1 – E1918_cor	-0.002 (0.006)	0.006 (0.005)	-0.003 (0.002)	0.015 (0.007)
C1549_1.5E – E1918_cor	0.037 (0.006)	0.022 (0.005)	0.001 (0.002)	0.024 (0.008)
E903_AM1GH – E1918_cor	0.007 (0.006)	0.008 (0.005)	-0.007 (0.002)	0.010 (0.016)
E903_E891BN – E1918_cor	0.029 (0.006)	0.018 (0.005)	-0.002 (0.002)	0.018 (0.016)
C1549_1.5E – C1549_G1	0.039 (0.001)	0.016 (0.001)	0.004 (0.001)	0.010 (0.011)
E903_E891BN – E903_AM1GH	0.022 (0.001)	0.011 (0.001)	0.005 (0.000)	0.008 (0.023)
C1549_G1 – E903_AM1GH	-0.009 (0.001)	-0.002 (0.001)	0.004 (0.001)	0.004 (0.017)
C1549_1.5E – E903_E891BN	0.008 (0.001)	0.004 (0.001)	0.003 (0.001)	0.007 (0.018)
C1549_G1 – C1549_G1_ORNL	0.009 (0.001)	0.004 (0.001)	0.006 (0.001)	0.009 (0.011)
C1549_1.5E – C1549_1.5E_ORNL	0.004 (0.001)	0.005 (0.001)	0.009 (0.001)	-0.001 (0.008)
C1549_G1_cor – E1918_cor	-0.002 (0.006)	0.006 (0.005)	-0.003 (0.002)	0.015 (0.007)
C1549_1.5E_cor – E1918_cor	0.037 (0.006)	0.022 (0.005)	0.001 (0.002)	0.024 (0.008)

687 Table 4 (continued)

688 (b)

	Aggregate A1 (5/8” gray granite)	Aggregate A2 (3/8" white marble)	Aggregate A3 (1.5” multicolor ballast)
Mean (standard deviation)			
E1918	0.218 (0.000)	0.548 (0.002)	0.194 (0.002)
E1918_cor	0.216 (0.000)	0.571 (0.003)	0.191 (0.002)
E1918A	0.232 (0.005)	0.588 (0.026)	0.156 (0.032)
C1549_G1	0.214 (0.039)	0.542 (0.030)	0.160 (0.043)
E903_AM1GH	NA	NA	NA
C1549_1.5E	0.222 (0.043)	0.553 (0.031)	0.167 (0.044)
E903_E891BN	NA	NA	NA
C1549_G1_ORNL	NA	NA	NA
C1549_1.5E_ORNL	NA	NA	NA
C1549_G1_cor	0.214 (0.039)	0.542 (0.030)	0.160 (0.043)
C1549_1.5E_cor	0.222 (0.043)	0.553 (0.031)	0.167 (0.044)
Difference (uncertainty)			
E1918 – E1918_cor	0.002 (0.000)	-0.023 (0.003)	0.004 (0.003)
E1918A – E1918	0.014 (0.005)	0.040 (0.026)	-0.038 (0.032)
E1918A – E1918_cor	0.015 (0.005)	0.017 (0.026)	-0.034 (0.032)
C1549_G1 – E1918_cor	-0.002 (0.039)	-0.029 (0.030)	-0.031 (0.043)
C1549_1.5E – E1918_cor	0.005 (0.043)	-0.018 (0.031)	-0.024 (0.044)
E903_AM1GH – E1918_cor	NA	NA	NA
E903_E891BN – E1918_cor	NA	NA	NA
C1549_1.5E – C1549_G1	0.007 (0.058)	0.011 (0.043)	0.007 (0.062)
E903_E891BN – E903_AM1GH	NA	NA	NA
C1549_G1 – E903_AM1GH	NA	NA	NA
C1549_1.5E – E903_E891BN	NA	NA	NA
C1549_G1 – C1549_G1_ORNL	NA	NA	NA
C1549_1.5E – C1549_1.5E_ORNL	NA	NA	NA
C1549_G1_cor – E1918_cor	-0.002 (0.039)	-0.029 (0.030)	-0.031 (0.043)
C1549_1.5E_cor – E1918_cor	0.005 (0.043)	-0.018 (0.031)	-0.024 (0.044)

689
690

691 Table 4 (continued)

692 (c)

	Tile T1 (white)	Tile T2 (orange)	Tile T3 (red)
Mean (standard deviation)			
E1918	0.708 (0.003)	0.356 (0.001)	0.185 (0.001)
E1918_cor	0.743 (0.004)	0.365 (0.001)	0.180 (0.001)
E1918A	0.743 (0.005)	0.342 (0.006)	0.158 (0.008)
C1549_G1	0.784 (0.013)	0.419 (0.007)	0.241 (0.005)
E903_AM1GH	0.770 (0.014)	0.421 (0.006)	0.234 (0.006)
C1549_1.5E	0.800 (0.012)	0.473 (0.007)	0.268 (0.006)
E903_E891BN	0.787 (0.014)	0.461 (0.006)	0.253 (0.006)
C1549_G1_ORNL	0.759 (0.001)	0.399 (0.001)	0.196 (0.007)
C1549_1.5E_ORNL	0.774 (0.002)	0.448 (0.003)	0.218 (0.004)
C1549_G1_cor	0.776 (0.001)	0.416 (0.001)	0.213 (0.007)
C1549_1.5E_cor	0.788 (0.002)	0.462 (0.003)	0.233 (0.004)
Difference (uncertainty)			
E1918 – E1918_cor	-0.035 (0.005)	-0.009 (0.001)	0.004 (0.002)
E1918A – E1918	0.035 (0.006)	-0.014 (0.006)	-0.027 (0.008)
E1918A – E1918_cor	0.000 (0.006)	-0.023 (0.006)	-0.022 (0.008)
C1549_G1 – E1918_cor	0.041 (0.013)	0.054 (0.007)	0.060 (0.006)
C1549_1.5E – E1918_cor	0.057 (0.012)	0.108 (0.007)	0.088 (0.007)
E903_AM1GH – E1918_cor	0.027 (0.015)	0.056 (0.006)	0.054 (0.006)
E903_E891BN – E1918_cor	0.044 (0.014)	0.097 (0.006)	0.073 (0.006)
C1549_1.5E – C1549_G1	0.017 (0.017)	0.054 (0.010)	0.027 (0.008)
E903_E891BN – E903_AM1GH	0.017 (0.020)	0.041 (0.008)	0.019 (0.009)
C1549_G1 – E903_AM1GH	0.014 (0.019)	-0.002 (0.009)	0.006 (0.008)
C1549_1.5E – E903_E891BN	0.014 (0.018)	0.011 (0.009)	0.015 (0.009)
C1549_G1 – C1549_G1_ORNL	0.025 (0.013)	0.019 (0.007)	0.045 (0.009)
C1549_1.5E – C1549_1.5E_ORNL	0.027 (0.012)	0.025 (0.008)	0.050 (0.008)
C1549_G1_cor – E1918_cor	0.033 (0.004)	0.052 (0.001)	0.032 (0.007)
C1549_1.5E_cor – E1918_cor	0.045 (0.004)	0.097 (0.003)	0.052 (0.004)

693

694

(d)

	Membranes M1 – M3 and shingle S1	Aggregates A1 – A3	Tiles T1 – T3
Difference range			
E1918 – E1918_cor	-0.042 to 0.006	-0.023 to 0.004	-0.035 to 0.004
E1918A – E1918	-0.016 to 0.052	-0.038 to 0.040	-0.027 to 0.035
E1918A – E1918_cor	-0.015 to 0.036	-0.034 to 0.017	-0.023 to 0.000
C1549_G1 – E1918_cor	-0.003 to 0.015	-0.031 to -0.002	0.041 to 0.060
C1549_1.5E – E1918_cor	0.001 to 0.037	-0.024 to 0.005	0.057 to 0.108
E903_AM1GH – E1918_cor	-0.007 to 0.010	NA	0.027 to 0.056
E903_E891BN – E1918_cor	-0.002 to 0.029	NA	0.044 to 0.097
C1549_1.5E – C1549_G1	0.004 to 0.039	0.007 to 0.011	0.017 to 0.054
E903_E891BN – E903_AM1GH	0.005 to 0.022	NA	0.017 to 0.041
C1549_G1 – E903_AM1GH	-0.009 to 0.004	NA	-0.002 to 0.014
C1549_1.5E – E903_E891BN	0.003 to 0.008	NA	0.011 to 0.015
C1549_G1 – C1549_G1_ORNL	0.004 to 0.009	NA	0.019 to 0.045
C1549_1.5E – C1549_1.5E_ORNL	-0.001 to 0.009	NA	0.025 to 0.050
C1549_G1_cor – E1918_cor	-0.003 to 0.015	-0.031 to -0.002	0.032 to 0.052
C1549_1.5E_cor – E1918_cor	0.001 to 0.037	-0.024 to 0.005	0.045 to 0.097

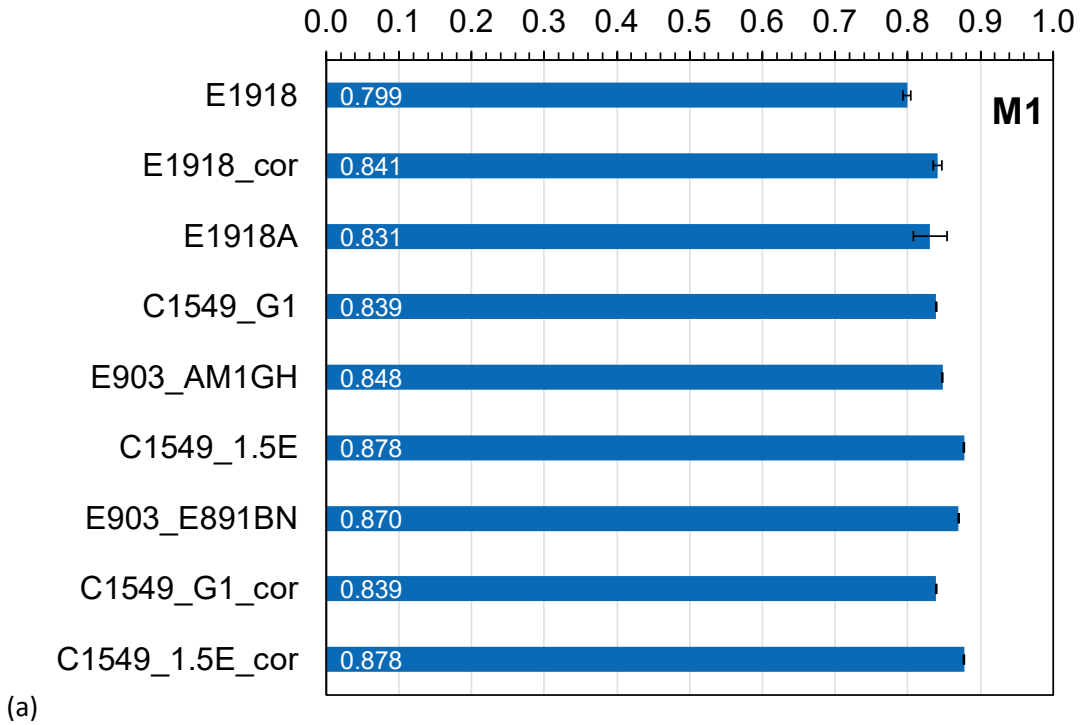

(a)

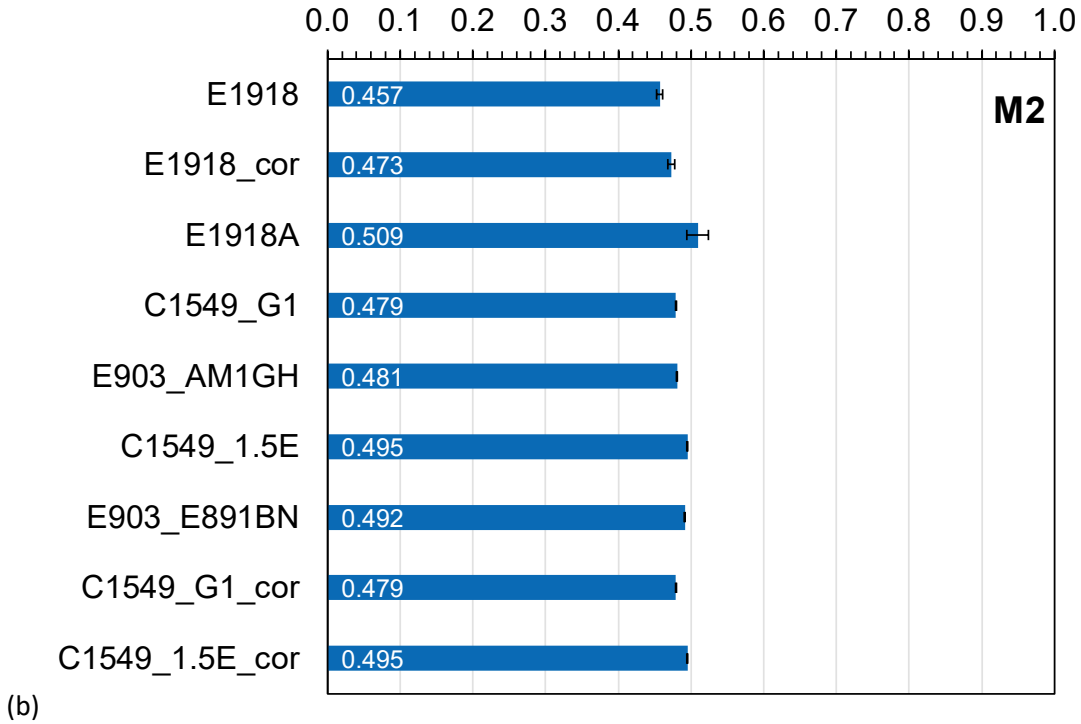

(b)

Figure 13. E1918, E1918_cor, E1918A, C1549_G1, E903_AM1GH, C1549_1.5E, E903_E891BN, C1549_G1_cor, and C1549_1.5E_cor albedos of (a) membrane M1 (white); (b) membrane M2 (gray); (c) membrane M3 (blue); (d) shingle S1 (gray); (e) aggregate A1 (5/8" gray granite); (f) aggregate A2 (3/8" white marble); (g) aggregate A3 (1.5" multicolor ballast); (h) tile T1 (white); (i) tile T2 (orange); (h) tile T3 (red).

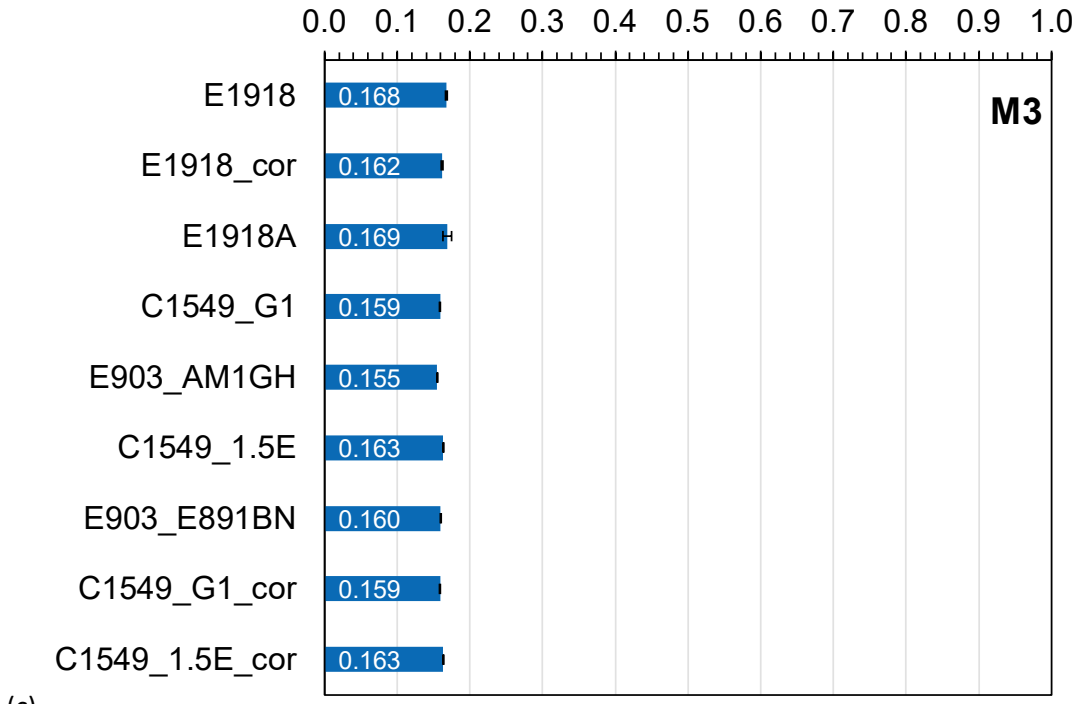

(c)

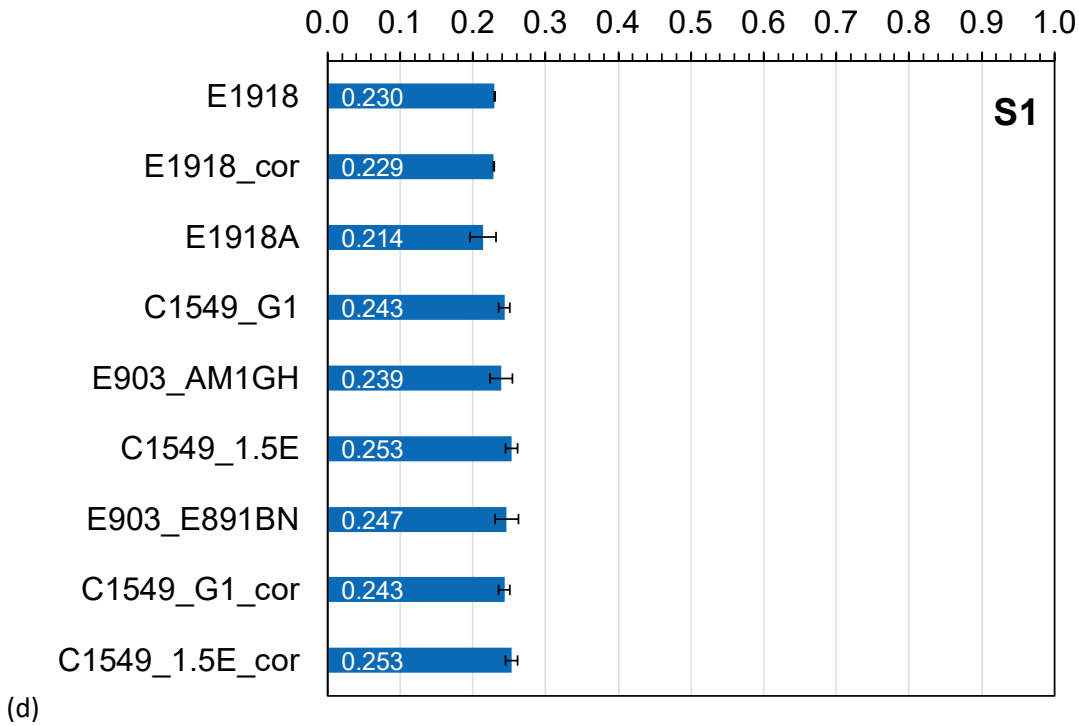

(d)

Figure 13 (continued)

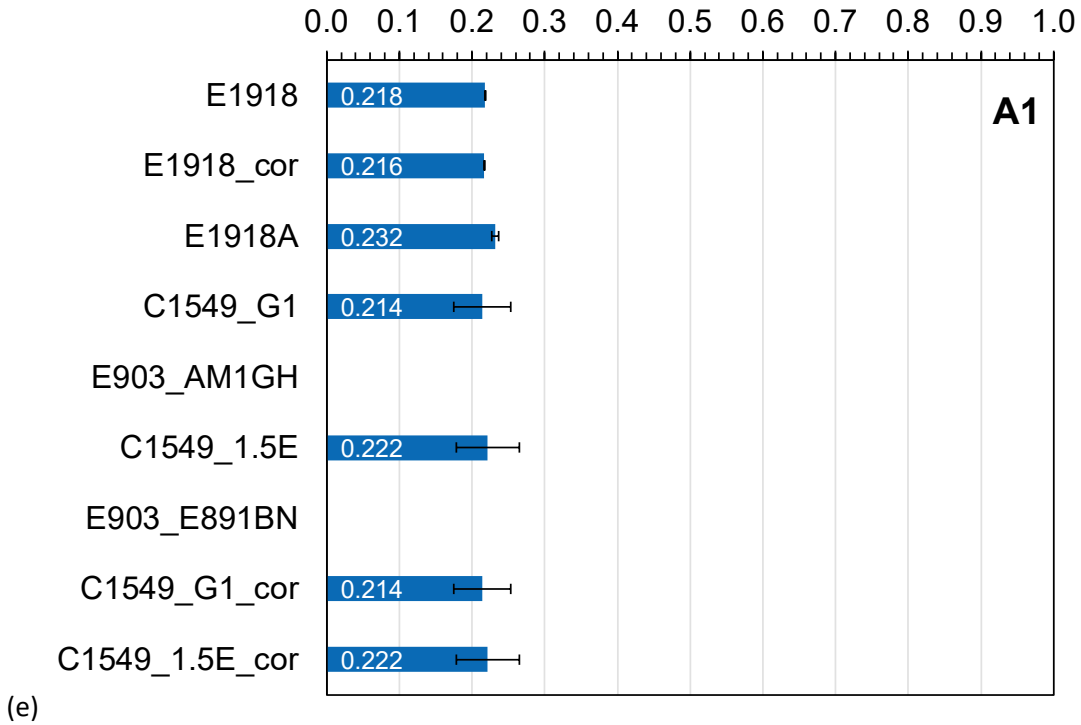

(e)

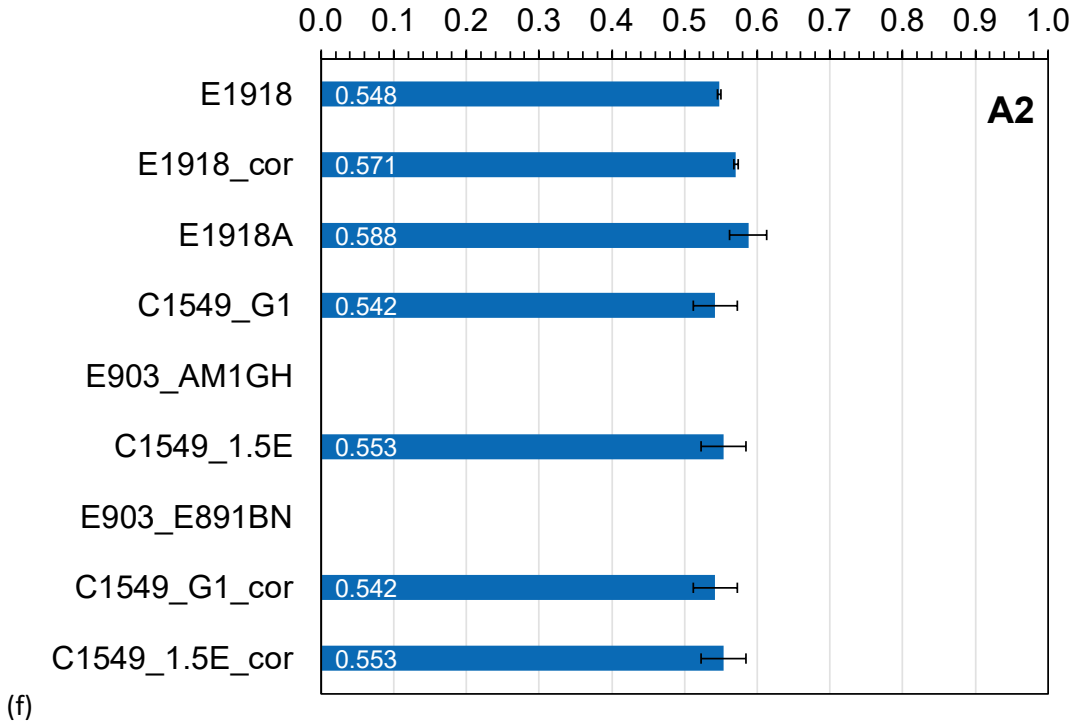

(f)

703 Figure 13 (continued)

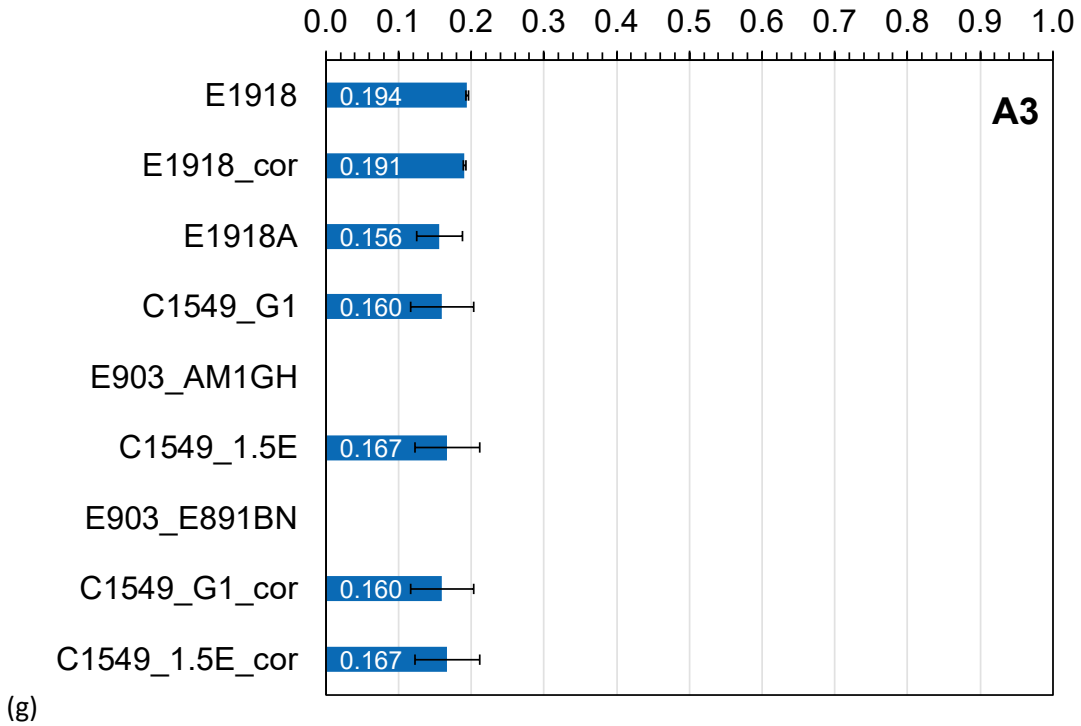

(g)

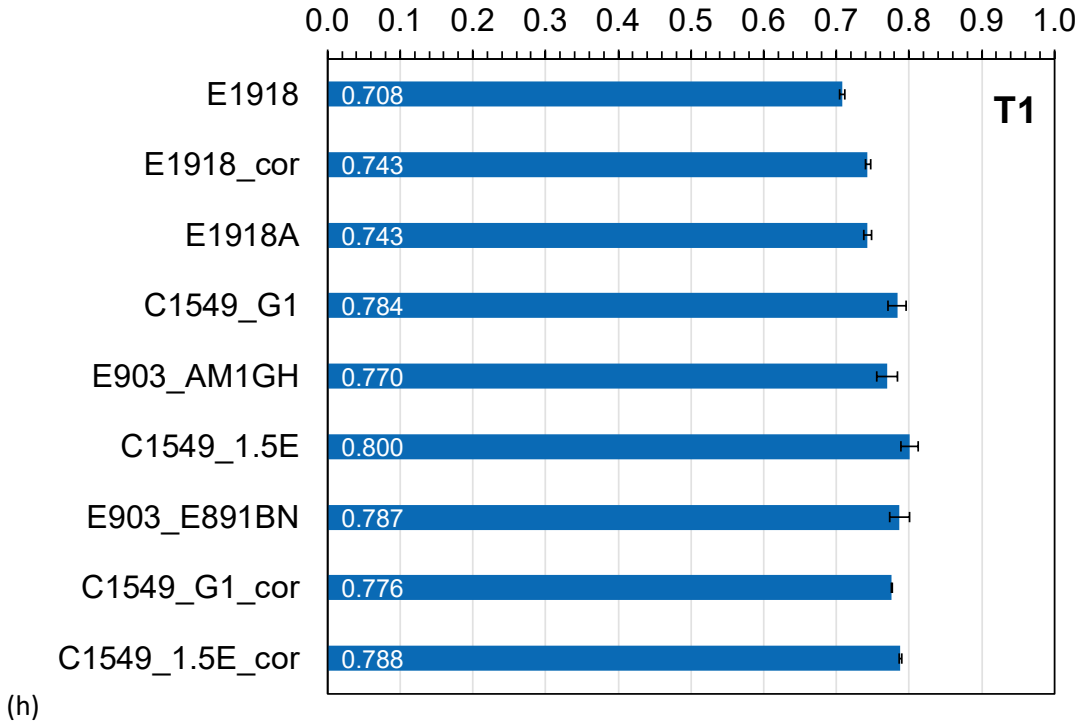

(h)

704 Figure 13 (continued)
705

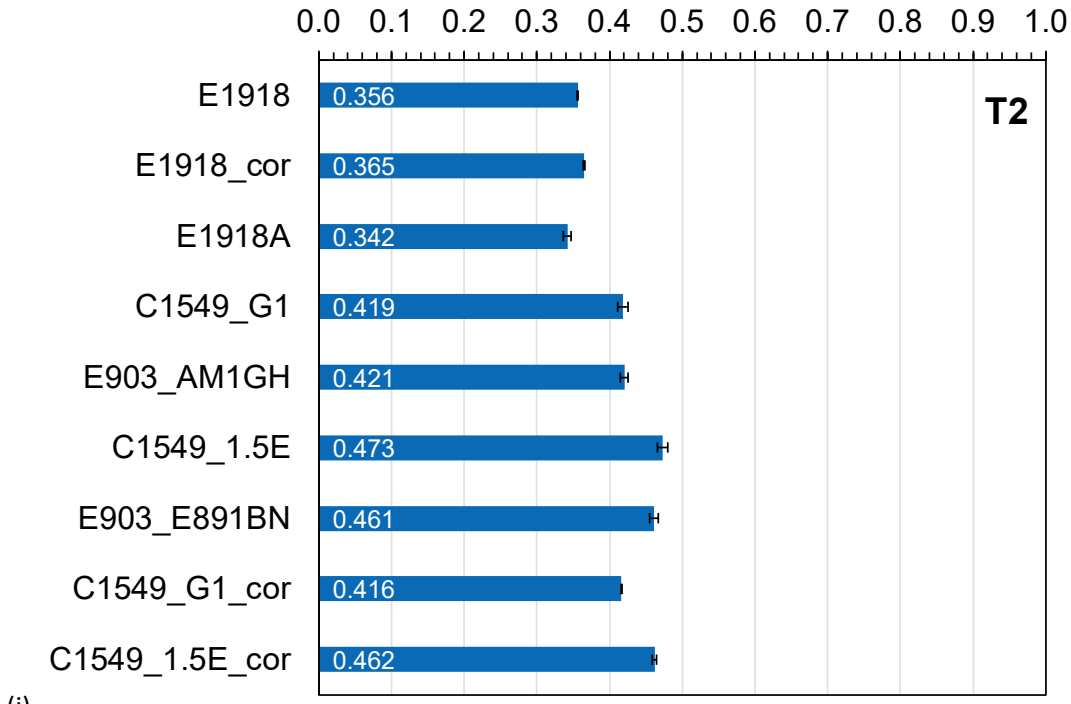

(i)

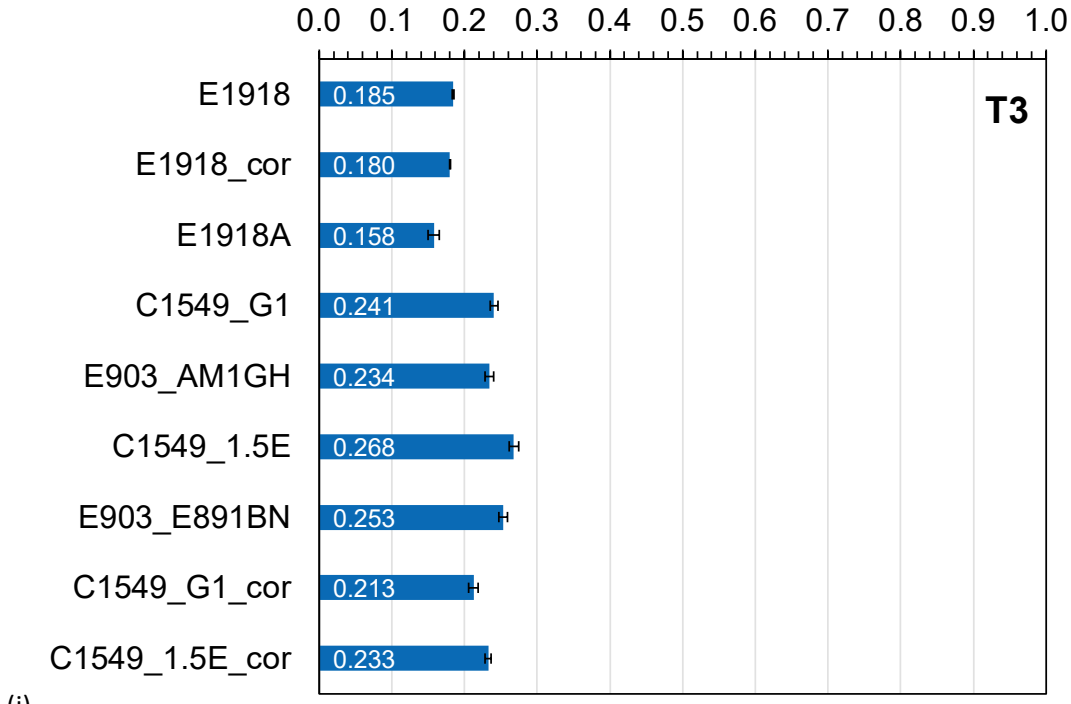

(j)

706 Figure 13 (continued)

4.2 Reflectometer (C1549) and spectrophotometer (E903) measurement of albedo

4.2.1 C1549 versus E903

The C1549 albedos of the membrane, shingle, and tile products closely matched their E903 albedos for the same choice of solar spectral irradiance. That is, C1549_G1 agreed with E903_AM1GH (Figure 14) and C1549_1.5E agreed with E903_E891BN (Figure 15) to within 0.015 (Table 4d). C1549 albedos were not compared to E903 albedos for aggregate products because latter were not measured.

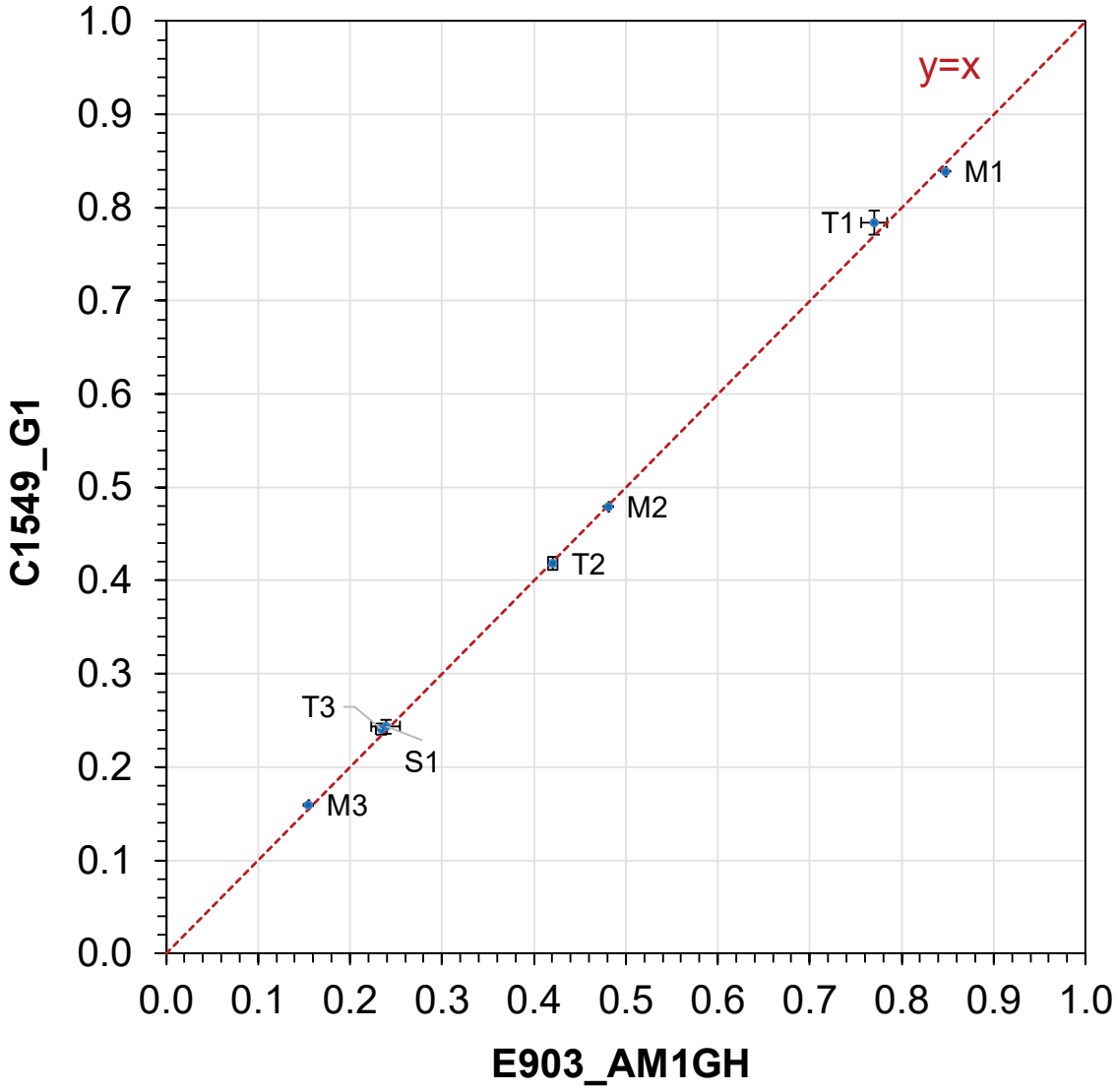

Figure 14. C1549_G1 albedo vs. E903_AM1GH (solar spectral reflectance weighted with air mass 1 global horizontal solar spectral irradiance) albedo for all products.

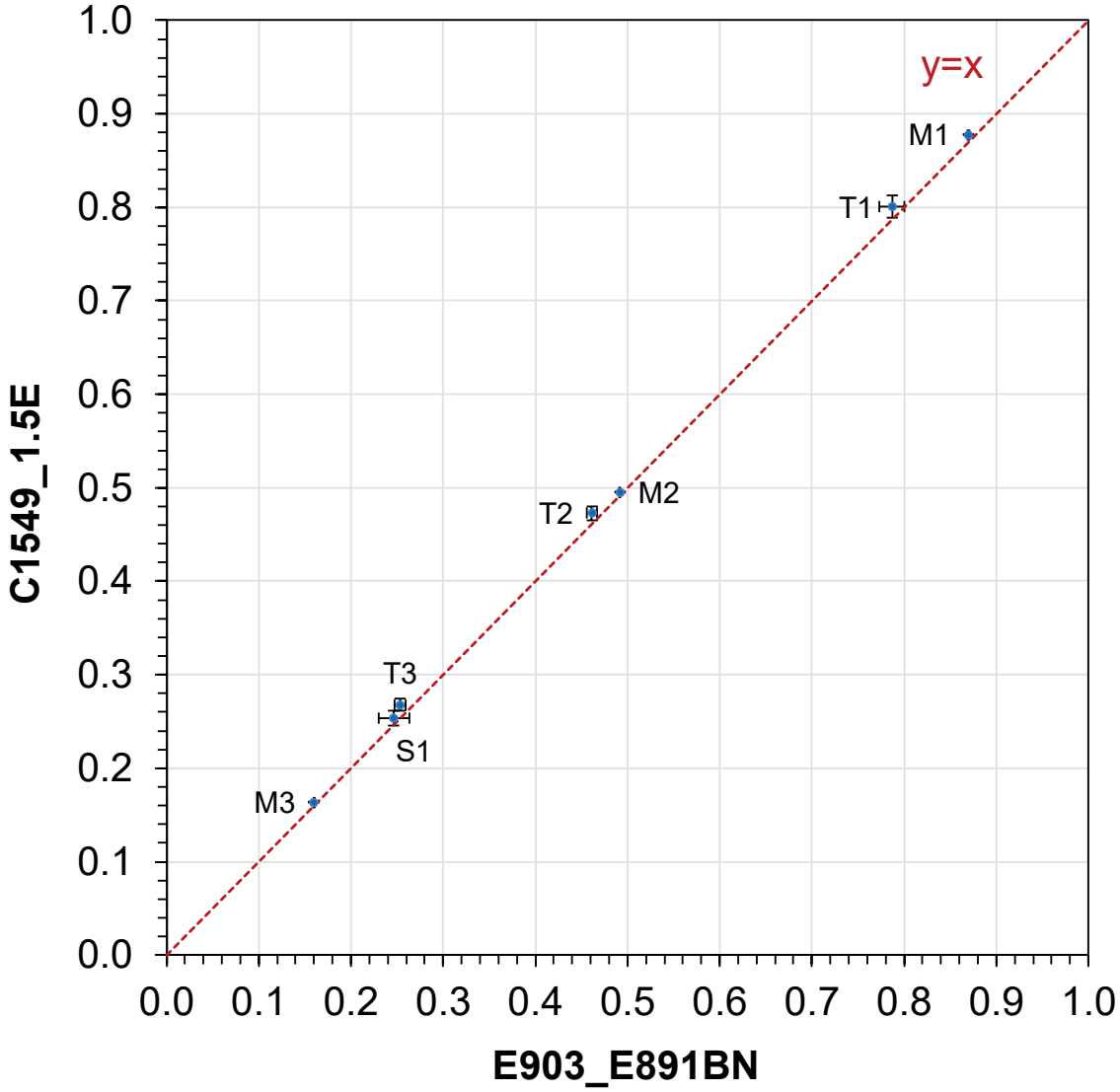

Figure 15. C1549_1.5E albedo vs. E903_E891BN (solar spectral reflectance weighted with ASTM E891 beam-normal solar spectral irradiance) albedo for all products.

Choice of solar spectral irradiance noticeably affected albedo for cool-colored products. Figure 16 shows the E903 solar spectral reflectances of the membranes and shingle (panel a) and the tiles and masks (panel b); their broadband reflectances and spectral selectances are detailed in Table 5. The two specimens with medium to high spectral selectance—tile T3, with selectance 0.13, and tile T2, with selectance 0.28—exhibited C1549_1.5E albedos that were 0.027 and 0.054 higher than their C1549_G1 albedos, respectively (Figure 17). The differences were slightly smaller for E903: E903_E891BN – E903_AM1GH was 0.019 for tile T3 and 0.041 for tile T2 (Figure 18). The rise with selectance of E891BN (beam-normal) albedo minus AM1GH (global) albedo is consistent with prior measurements by Levinson et al. (Levinson et al., 2010b). This effect stems from spectral selectance, rather than assembly geometry or material composition.

Means and standard deviations of the C1549 and E903 albedos for each choice of solar spectrum, and the differences between these albedos, are shown in Table 4a-c.

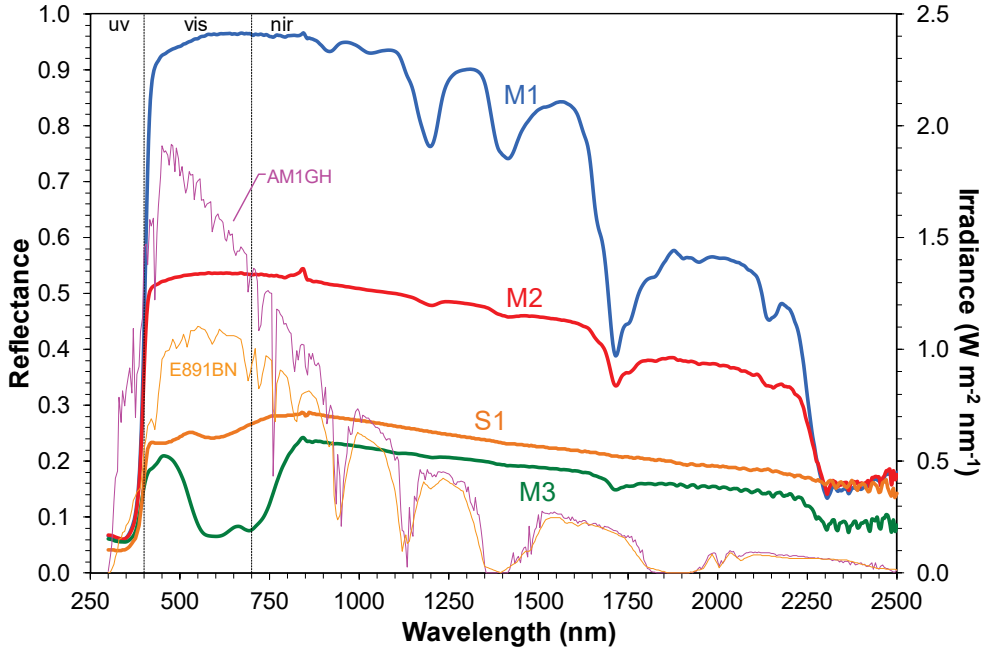

(a)

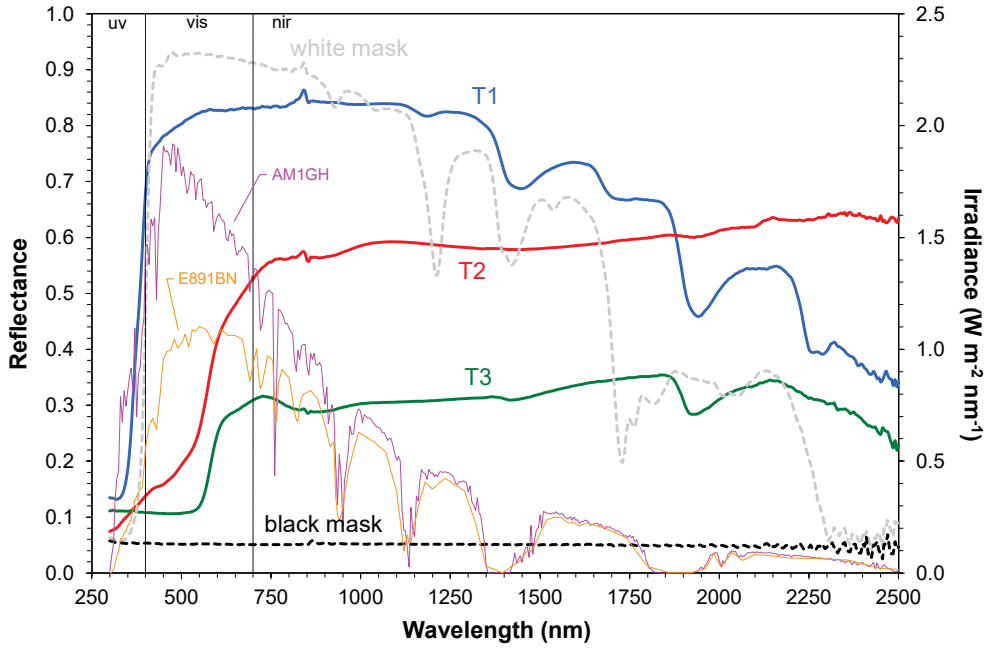

(b)

Figure 16. E903 solar spectral reflectance of (a) membranes M1 – M3 and shingle S1 and (b) tiles T1 – T3 and the white and black masks. Also shown are the AM1GH and E891BN solar spectral irradiances used to compute broadband reflectances and spectral selectance.

737 Table 5. E903 solar, ultraviolet, visible, and near-infrared broadband reflectances of each test
738 specimen and each E1918A mask, weighted with the AM1GH and E891BN solar spectral
739 irradiances. Also shown is AM1GH spectral selectance, evaluated as near-infrared reflectance
740 minus visible reflectance.

Specimen	M1	M2	M3	S1	T1	T2	T3	white mask	black mask
AM1GH reflectance									
solar	0.848	0.481	0.155	0.239	0.770	0.421	0.234	0.790	0.052
uv	0.129	0.118	0.079	0.068	0.336	0.111	0.110	0.140	0.053
vis	0.934	0.527	0.127	0.243	0.807	0.296	0.173	0.910	0.052
nir	0.867	0.488	0.190	0.258	0.795	0.577	0.308	0.768	0.051
E891BN reflectance									
solar	0.870	0.492	0.160	0.247	0.787	0.461	0.253	0.802	0.051
uv	0.146	0.133	0.085	0.076	0.383	0.115	0.110	0.160	0.053
vis	0.941	0.529	0.120	0.244	0.811	0.313	0.182	0.915	0.052
nir	0.858	0.484	0.190	0.257	0.791	0.578	0.308	0.758	0.051
AM1GH selectance	-0.067	-0.039	0.062	0.015	-0.012	0.280	0.135	-0.142	-0.001

741

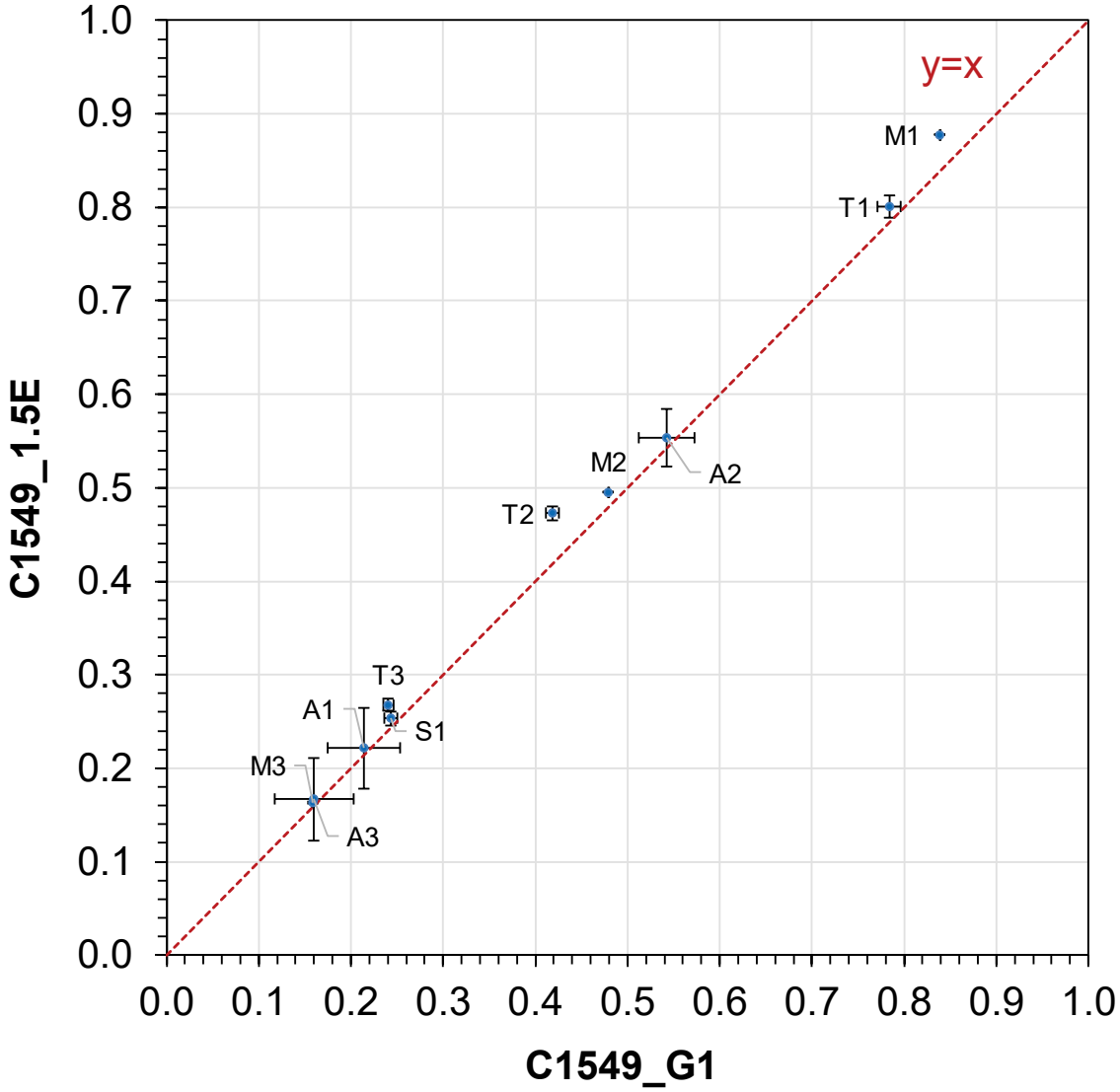

742

743 Figure 17. C1549_1.5E albedo vs. C1549_G1 albedo for all products.

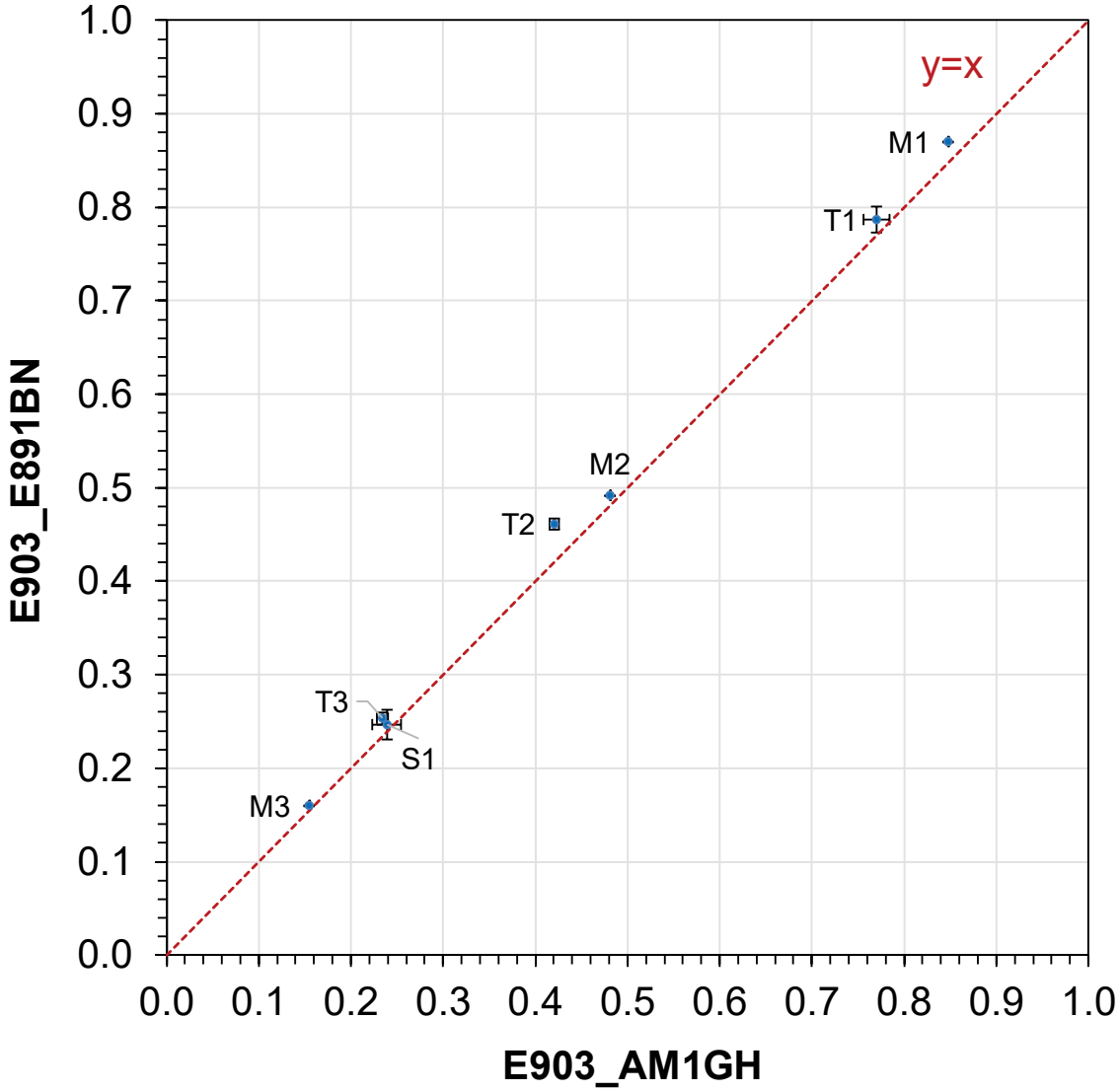

Figure 18. E903_E891BN albedo vs. E903_AM1GH albedo for all products except the aggregates.

4.2.2 Specular reflectances of specimens and masks

The AM1GH solar directional-normal specular reflectance at 8° incidence of each non-aggregate specimen and each mask was less than 0.02. This suggests that their corresponding specular reflectances at incidence angles up to 45° are negligible (less than $1.25 \times 0.02 = 0.025$) and that these specimens and masks can be treated as Lambertian reflectors for purposes of E1918 and E1918A. We also assume that the roughness of the aggregate specimens ensures that the specular component of reflectance is quite small.

4.2.3 Correction of C1549 albedos for tile chips

Differences of up to 0.050 were observed when comparing the C1549 albedos of the tile chips measured with the LBNL reflectometer to the C1549 albedos of the assembly tiles measured with the ORNL reflectometer (entries "C1549_G1 – C1549_G1_ORNL" and "C1549_1.5E – C1549_1.5E_ORNL" in Table 4c). Since (a) the C1549 albedos of the membranes and shingle measured with the LBNL reflectometer agreed to within 0.009 of those measured with the ORNL reflectometer (Table 4a); and (b) the curvature adjustment identified in Section 3.4.1 would reduce the C1549 albedo gap by about 0.01 for flat tile chips T1 and T3, and not at all for curved tile chip T2, we concluded that the differences between the albedos of the tile chips and those of the assembly tiles stemmed at least in part from minor variations in production. Therefore, we calculated corrected C1549 albedos as specified in Section 3.4.3.

4.3 Pyranometer (corrected) vs. reflectometer (corrected) measurement of albedo

Figure 19 compares C1549_G1_cor albedo[5] to E1918_cor albedo for all products. Agreement is near-perfect for the membranes—within 0.006—because the E1918 correction performed in Section 4.1.2 is based on their membranes C1549_G1 albedos. It is also very good for the shingle (C1549_G1_cor albedo – E1918_cor albedo = 0.015) (Table 4a). Absolute differences between C1549_G1_cor albedo and E1918_cor albedo are slightly larger for some of the aggregates (C1549_G1_cor albedo – E1918_cor albedo = -0.031 to -0.002) but the magnitude of each difference is smaller than the uncertainty in the difference induced by the standard deviation in C1549_G1 albedo (0.030 to 0.043) (Table 4b).

C1549_G1_cor albedo is 0.032 to 0.052 higher than E1918_cor albedo for the tiles, and the magnitudes of these differences are much larger than their uncertainties (0.001 to 0.007) (Table 4c). This confirms what we expect from first principles—namely, that the return-to-surface of light reflected by the high-profile tile assemblies makes each assembly significantly less reflective than its corresponding flat tile chip. This first effect results from the assembly geometry, rather than material composition or spectral selectance (variation of reflectance with wavelength).

[5] As noted in Section 3.4.3, correction of C1549 was applied only to the tile chips; for the remaining products, C1549_G1_cor = C1549_G1 and C1549_1.5E_cor = C1549_1.5E.

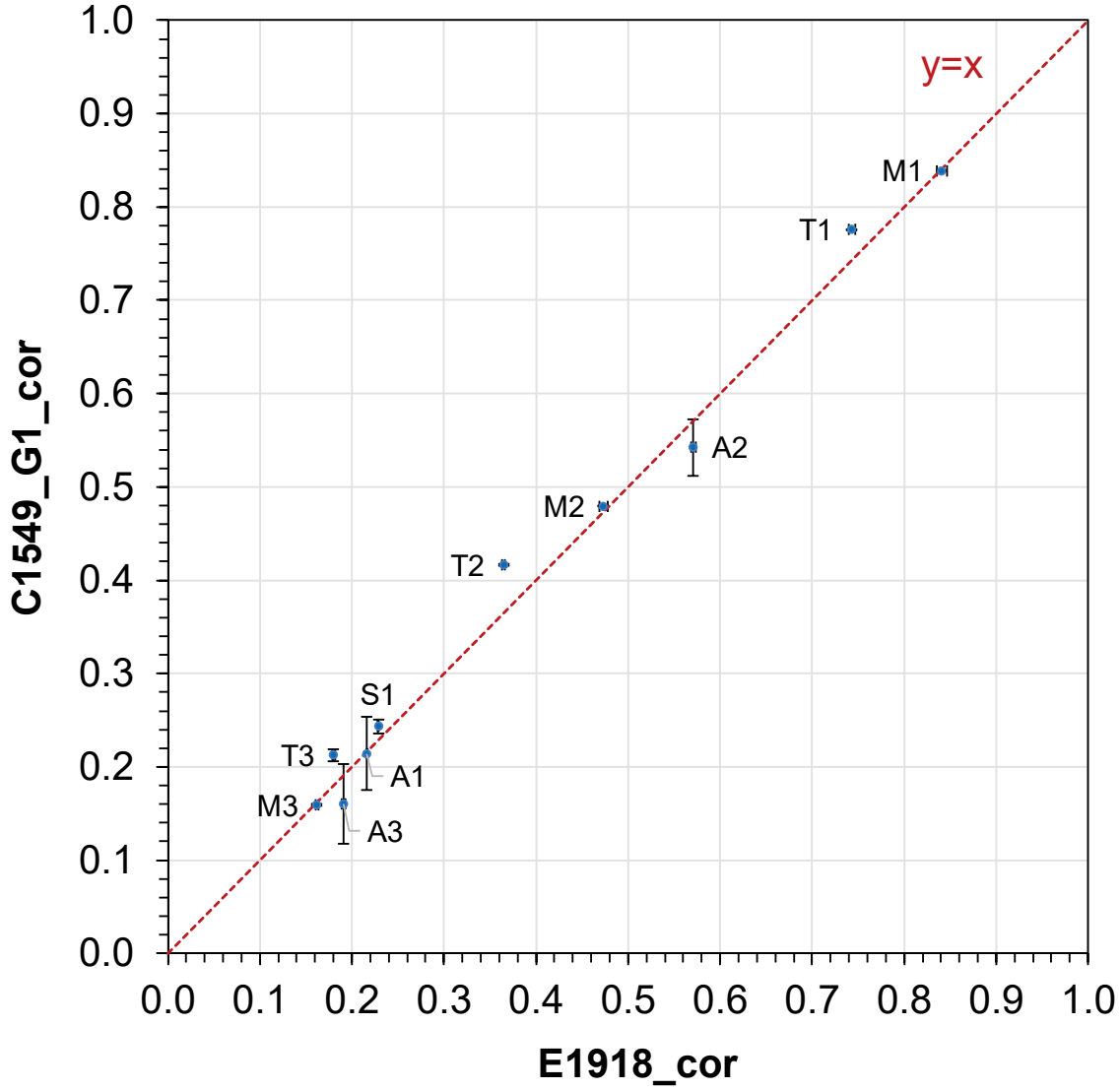

Figure 19. C1549_G1_cor albedo vs. E1918_cor albedo for all products.

Figure 20 compares C1549_1.5E_cor albedo to E1918_cor albedo for all products. Agreement is near-perfect for membrane M3 (blue), but C1549_G1 – E1918_cor = 0.022 to 0.037 for the remaining membranes and shingle. Absolute differences between C1549_1.5_cor albedo and E1918_cor albedo are slightly smaller for the aggregates (C1549_G1 – E1918_cor = -0.024 to 0.005) but the magnitude of each difference is smaller than the uncertainty in the difference induced by the standard deviation in C1549_1.5_cor albedo (0.031 to 0.044) (Table 4).

C1549_1.5E_cor albedo is 0.045 to 0.097 higher than E1918_cor albedo for the tiles, and the magnitudes of these differences are much larger than their uncertainties (0.003 to 0.004) (Table 4c). Here the overestimation of albedo caused by representing the high-profile tile assembly with a flat or convex tile chip was compounded by the overestimation of albedo induced by using a beam-normal, rather than global, solar spectral irradiance.

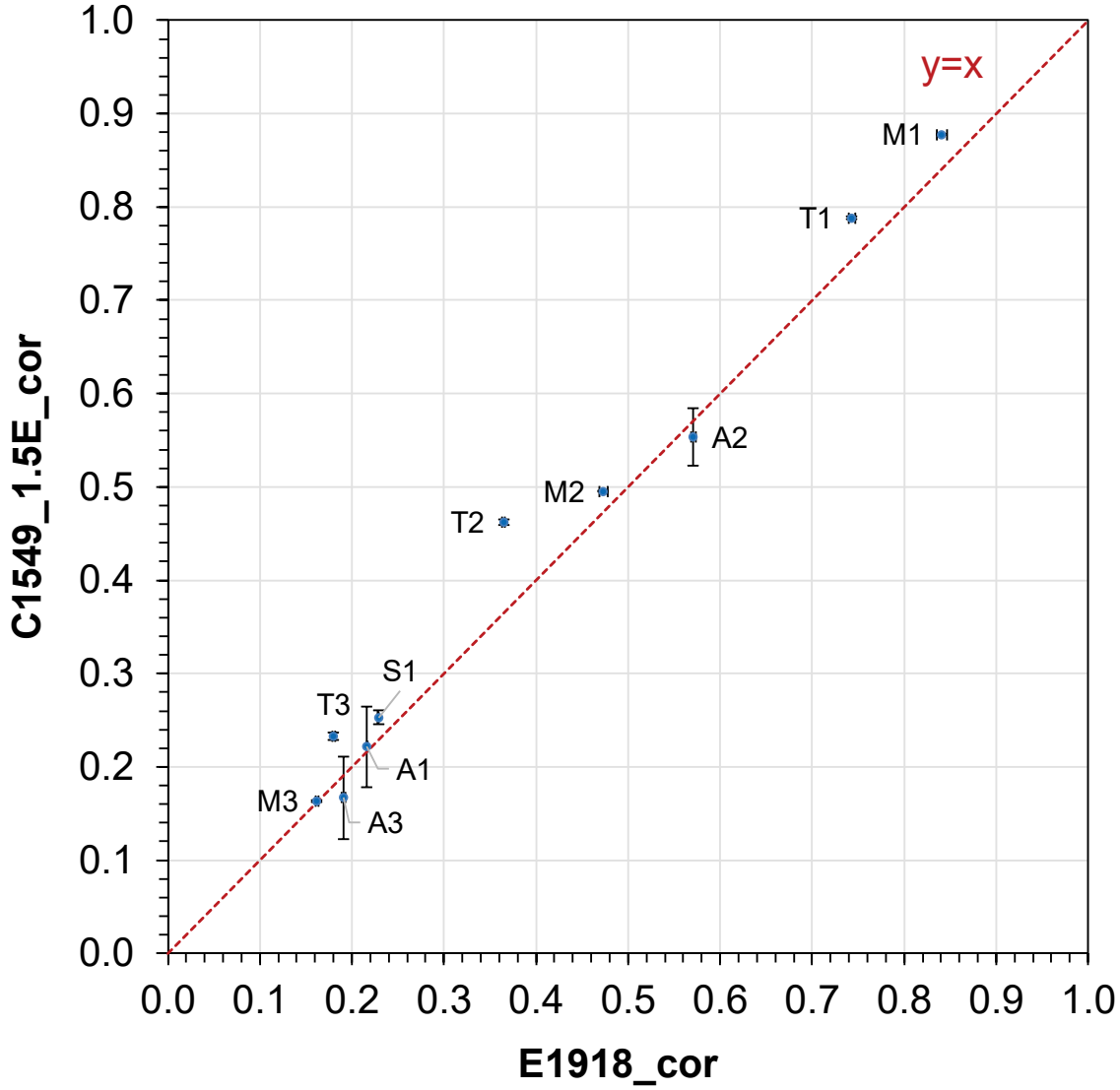

Figure 20. C1549_1.5E albedo vs. E1918_cor albedo for all products.

4.4 Comparison of E1918, C1549, and E903 measurements to those in past studies

For our full set of 10 specimens, the standard deviations of the E1918 measurements in the current study (0.000 – 0.005, mean 0.002) were comparable to the repeatability standard deviations reported in the E1918 precision-and-bias statement (0.0023 – 0.0056, mean 0.0040), while those of our C1549_1.5E measurements (0.001 – 0.044, mean 0.015) were substantially higher than those in the C1549 precision-and-bias statement (0.0006 – 0.0021, mean 0.0014). Excluding the three aggregates brings the standard deviations of our C1549_1.5E measurements to 0.001 – 0.012 (mean 0.005)—quite small, but still greater than those in the C1549 precision-and-bias statement.

This suggests that the surfaces of the unidentified roofing materials used in the C1549 precision-and-bias study may have been more homogenous that those in our study.

The standard deviations of our E903_E891BN measurements (0.000 – 0.016, mean 0.006) were well within the 0.02 uncertainty specified by the E903 summary of bias, precision, and uncertainty.

The range of albedo difference C1549_1.5E – E903_E891BN for the non-aggregate specimens in our study (-0.009 to 0.014, mean 0.002) was comparable to that reported in the C1549 precision-and-bias statement (-0.0020 to 0.0290, mean 0.0163) and much smaller than that reported by Synnefa et al. (2013) (-0.050 to 0.020, mean 0.005). This is consistent with our hypothesis that the extreme difference of -0.050 in the latter study resulted from the use of the wrong calibration standard for one specimen.

4.5 Assessment of reflectance decrease $\Delta\mathcal{R}$ for high-profile roof tiles

In Section 2.5, we outlined the theoretical expectation of the reflectance adjustment for curved products. Now, we compare the experimental results with the simple (Berdahl) model.

The area ratio of each of the three tiles—1.270 for T1, 1.245 for T2, and 1.220 for T3—was obtained by analyzing the tile cross section scale drawings shown in Figures A-11 to A-13 of Appendix A to estimate curved surface area S_2 and footprint (plan) surface area S_1. (It's worth mentioning that the length of the actual curved tile surfaces can be obtained directly with a flexible measuring tape.) The tiles overlap, so only the exposed upper surface of each tile, and the exposed tile edges, were included in S_2; the relatively small openings below the upper tile edges were neglected. The experimental reflectance decrease $\Delta\mathcal{R}$ was determined by subtracting the corrected pyranometer determination E1918_cor (macroscopic reflectance $\hat{\mathcal{R}}$) from the reflectometer measurement C1549_G1_cor (planar reflectance $\mathcal{R}$).

Figure 21 shows the results. The three measured reflectance decreases (filled circles) $\Delta\mathcal{R}$ range from 0.032 to 0.052 with average value 0.039. Notably, they are distinct from zero. Also, the simple model is in rough agreement; deviations (modeled – measured) are +0.009 for T1, -0.001 for T2, and -0.003 for T3. The mean deviation is thus very small (-0.001), indicating that the model performed well. The root mean square deviation is 0.005, an indication of the experimental uncertainty.

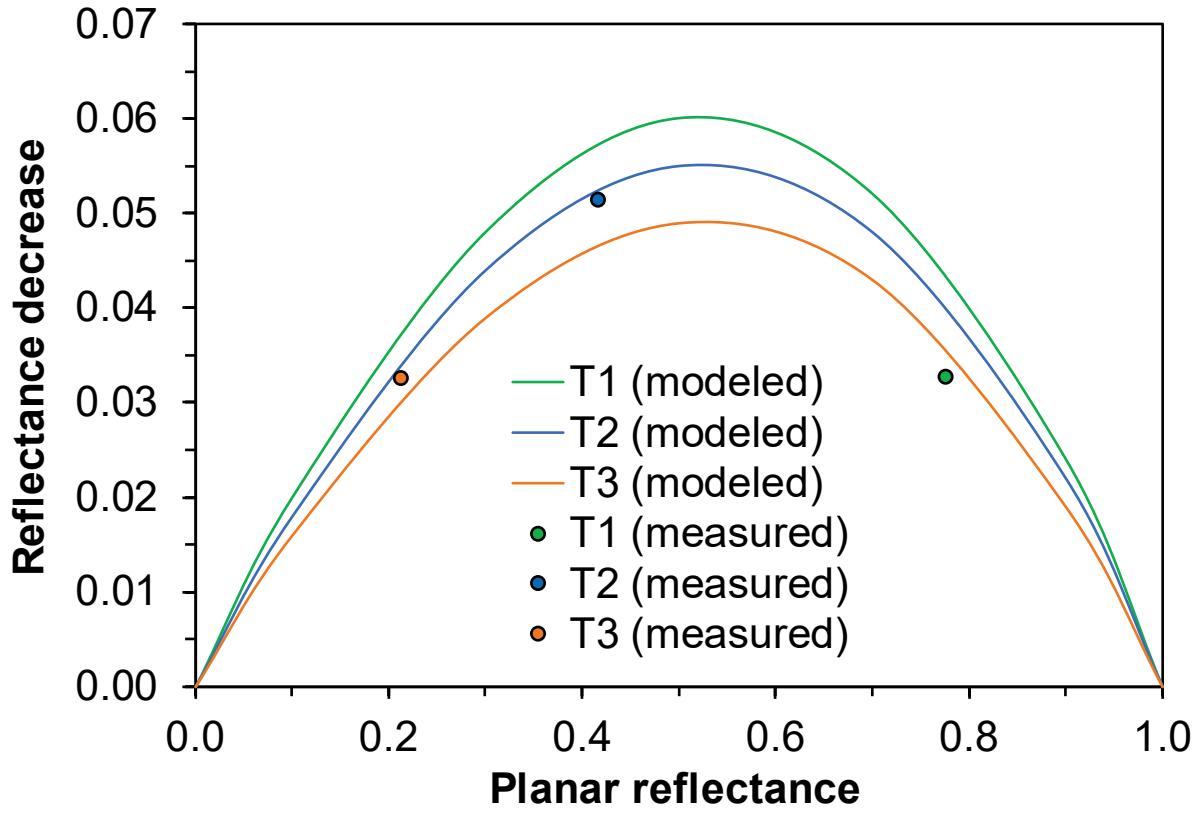

Figure 21. Modeled and measured values of reflectance decrease $\Delta\mathcal{R}$ versus planar reflectance $\mathcal{R}$ for tiles T1 – T3. Curves are based on the simple (Berdahl) model while each filled circle (measurement) is planar reflectance C1549_G1_cor minus macroscopic reflectance E1918_cor.

5 Conclusions

Our experimental comparison of pyranometer, reflectometer, and spectrophotometer methods for the measurement of albedo (solar reflectance) indicates that when paired with a global-horizontal, rather than beam-normal, choice of solar spectral irradiance, C1549 (reflectometer) albedo measurements applied to membrane and shingle coupons agreed closely with their E1918 (pyranometer) albedos corrected for shadow and background errors, with absolute differences not exceeding 0.015. The agreement for the membranes was somewhat artificial because the E1918 albedo correction used the C1549_G1 albedos of the membranes. Agreement between the C1549_G1 ("box of rocks") albedos and E1918 corrected albedos of the aggregates was also good, with absolute differences not exceeding 0.031. However, large standard deviations in the C1549_G1 albedos of the aggregates yielded the uncertainties in difference between C1549_G1 and E1918_cor albedos up to 0.043.

We found some differences between the C1549 albedos of tile chips and those of their assembly tiles that could not be fully attributed to variations in surface curvature or instrumentation. This suggests that some care may be needed to verify that tile chips have the same composition and

C1549 albedo (after adjustment for curvature) as the tiles that they represent. The same principle applies to any curved material represented by a flat chip.

The C1549_G1_cor albedos of tile chips estimated by adjusting the C1549_G1_ORNL albedos of assembly tiles for curvature and instrumentation variation were 0.032 to 0.052 higher than the E1918_cor albedos of their corresponding high-profile tile assemblies. This effect results from the assembly geometry, rather than material composition or spectral selectance (variation of reflectance with wavelength). The lower albedo of the tile assemblies is quantitatively consistent with the return-to-surface of reflected light. Our best estimate of the reflectance decrease induced by tile curvature and step edges is 0.04 for the three high-profile tiles studied. The simple model for estimating these reflectance adjustments performed well.

Switching to the beam-normal albedo (E891BN) increased the C1549 albedos of the tested products by 0.004 to 0.054, with the largest increases (C1549_1.5E – C1549_G1) accruing to spectrally selective cool colors. This second effect stems from spectral selectance, rather than assembly geometry or material composition. Applying the E891BN irradiance to the cool-colored tile T3 chip compounded the error associated with representing a high-profile surface by a flat specimen—the C1549_1.5E_cor albedo of the tile T3 chip was 0.097 higher than the E1918_cor albedo of the T3 tile assembly.

We also found that E1918A albedos agreed with E1918_cor albedos to within an absolute difference of 0.036, and that orientation of each high-profile tile assembly had minimal effect on its E1918 and E1918A albedos, with absolute changes not exceeding 0.005 and 0.014, respectively.

As expected from the design of the SSR and from past analysis by Levinson et al. (2010b), C1549 and E903 albedos agreed closely with each other (to within 0.015) when based on the same solar spectral irradiance.

Finally, we note that the E1918A method can be challenging to execute on a hot and/or windy day because the black mask can grow too hot to handle with bare hands, and strong winds can dislodge the masks from the test specimen. Thin metal plates affixed to the back of the masks may provide helpful ballast.

Acknowledgements

This study was funded by the Cool Roof Rating Council and supported by the Assistant Secretary for Energy Efficiency and Renewable Energy, Building Technologies Office of the U.S. Department of Energy under Contract No. DE-AC02-05CH11231.

The authors thank Annette Sindar of Eagle Roofing Products and Thomas Arzu of Boral Roofing, Mark Harner of CertainTeed, Al Janni of Duro-Last, Glenn Bestor of SOPREMA, and Wayne Lucas of Lucas Specialty Rock for the donation of roofing materials; Jaynae Bushong, Joe Farley, Amanda Florendo, Peter Williamson, and Keith Claunch of Atlas Material Testing Solutions for

providing site access, building test platforms, providing use of tools and supplementary testing materials, sharing on-site weather data, providing supplementary photos and measurements, and arranging transportation of materials; and Daisuke Narumi of Yokohama National University and Bill Hronek and Jose Gomez of JBS Roofing for helping make reflectance measurements at the Atlas site. We also thank Andre Desjarlais and Jerald Atchley of Oak Ridge National Laboratory for the loan of a portable reflectometer used at the Atlas site; Charlie Moore of Devices & Services for providing details of his curved-surface reflectance model; and Rick Olson of the Tile Roofing Institute, Rich Slomko of Atlas Material Testing Solutions, Andre Desjarlais of Oak Ridge National Laboratory, and Hashem Akbari of Concordia University for their assistance with various aspects of the experimental design and study logistics.

References

Akbari, H., Levinson, R., 2008. Evolution of cool-roof standards in the US. Adv. Build. Energy Res. 2, 1–32. https://doi.org/10.3763/aber.2008.0201

Akbari, H., Levinson, R., Stern, S., 2008. Procedure for measuring the solar reflectance of flat or curved roofing assemblies. Sol. Energy 82, 648–655. https://doi.org/10.1016/j.solener.2008.01.001

ASHRAE, 2016. ANSI/ASHRAE/IES Standard 90.1-2016: Energy Standard for Buildings Except Low-Rise Residential Buildings. https://www.techstreet.com/ashrae/ashrae_standards.html

ASHRAE, 2014. ANSI/ASHRAE/USGBC/IES Standard 189.1-2014: Standard for the Design of High-Performance Green Buildings Except Low-rise Residential Buildings. https://www.techstreet.com/ashrae/ashrae_standards.html

ASTM International, 2016a. ASTM E1918-16 Standard Test Method for Measuring Solar Reflectance of Horizontal and Low-Sloped Surfaces in the Field. West Conshohocken, PA. https://doi.org/10.1520/E1918-16

ASTM International, 2016b. ASTM C1549-16: Standard Test Method for Determination of Solar Reflectance Near Ambient Temperature Using a Portable Solar Reflectometer. West Conshohocken, PA. https://doi.org/10.1520/C1549-16

ASTM International, 2012. ASTM E903-12: Standard Test Method for Solar Absorptance, Reflectance, and Transmittance of Materials Using Integrating Spheres. West Conshohocken, PA. https://doi.org/10.1520/E0903-12

ASTM International, 1992. ASTM E891-87(1992): Tables for Terrestrial Direct Normal Solar Spectral Irradiance Tables for Air Mass 1.5. West Conshohocken, PA. https://doi.org/10.1520/E0891-87R92

Berdahl, P., Akbari, H., Jacobs, J., Klink, F., 2008. Surface roughness effects on the solar reflectance of cool asphalt shingles. Sol. Energy Mater. Sol. Cells 92, 482–489. https://doi.org/10.1016/j.solmat.2007.10.011

California Building Standards Commission, 2016. 2016 California Green Buildings Standards Code (CALGreen). http://www.bsc.ca.gov/Home/CALGreen.aspx

California Energy Commission, 2016. 2016 Building Energy Efficiency Standards for Residential and Nonresidential Buildings (Publication CEC-400-2015-037-CMF). Sacramento, CA. http://www.energy.ca.gov/title24/

Cool Roof Rating Council, 2018a. Resources—rebates & codes [WWW Document]. https://coolroofs.org/resources/rebates-and-codes

Cool Roof Rating Council, 2018b. Rated Products Directory [WWW Document]. https://coolroofs.org/directory

Cool Roof Rating Council, 2016. ANSI/CRRC S100 (2016): Standard Test Methods for Determining Radiative Properties of Materials. Portland, OR. https://coolroofs.org/product-rating/ansi-crrc-s100

Georgia State University, 2019. Hyperphysics tutorial: Fresnel's equations [WWW Document]. http://hyperphysics.phy-astr.gsu.edu/hbase/phyopt/freseq.html#c1

Howell, J.R., 2018. A Catalog of Radiation Heat Transfer Configuration Factors, 3rd Edition [WWW Document]. http://www.thermalradiation.net/indexCat.html

Howell, J.R., 1998. The Monte Carlo Method in Radiative Heat Transfer. J. Heat Transfer 120, 547–560. https://doi.org/10.1115/1.2824310

Howell, J.R., Menguc, M.P., Siegel, R., 2015. Thermal Radiation Heat Transfer, 6th ed. Chapman and Hall/CRC, Boca Raton.

International Code Council, 2018a. 2018 International Energy Conservation Code. https://www.iccsafe.org

International Code Council, 2018b. 2018 International Green Construction Code. https://www.iccsafe.org

Kipp & Zonen, 2016. Instruction manual: CMP series pyranometer, CMA series albedometer [WWW Document]. https://www.kippzonen.com/Download/64/Manual-Albedometers-English

Levinson, R., Akbari, H., Berdahl, P., 2010a. Measuring solar reflectance—Part I: Defining a metric that accurately predicts solar heat gain. Sol. Energy 84, 1717–1744. https://doi.org/10.1016/j.solener.2010.04.018

Levinson, R., Akbari, H., Berdahl, P., 2010b. Measuring solar reflectance—Part II: Review of practical methods. Sol. Energy 84, 1745–1759. https://doi.org/10.1016/j.solener.2010.04.017

Levinson, R., Berdahl, P., Akbari, H., 2005. Solar spectral optical properties of pigments—Part

959 II: Survey of common colorants. Sol. Energy Mater. Sol. Cells 89, 351–389.
960 https://doi.org/10.1016/j.solmat.2004.11.013

961 Levinson, R., Chen, S., Berdahl, P., Rosado, P., Medina, L.A., 2014. Reflectometer measurement
962 of roofing aggregate albedo. Sol. Energy 100, 159–171.
963 https://doi.org/10.1016/j.solener.2013.11.006

964 Mei, G., Wu, B., Ma, S., Qin, Y., 2017. A simplified method for the solar reflectance of a finite
965 surface in field. Meas. J. Int. Meas. Confed. 110, 211–216.
966 https://doi.org/10.1016/j.measurement.2017.06.039

967 Moore, C., 2010. SSR-ER reflectance measurements for large radius cylindrical surfaces
968 (Technical Note TN11-1). Devices & Services, Dallas, TX.
969 http://devicesandservices.com/TechNotes/TN11-1.pdf

970 Moore, C., 2009. A proposed correction to reflectance measurements of profiled surfaces
971 (Technical Note 09-2). Devices & Services, Dallas, TX.
972 http://devicesandservices.com/TechNotes/TN09-2.pdf

973 National Renewable Energy Laboratory, 2018. Measurement and Information Data Center Solar
974 Position and Intensity (MIDC SOLPOS) Calculator [WWW Document].
975 https://midcdmz.nrel.gov/solpos/solpos.html

976 Qin, Y., He, H., 2017. A new simplified method for measuring the albedo of limited extent
977 targets. Sol. Energy 157, 1047–1055. https://doi.org/10.1016/j.solener.2017.09.027

978 Qin, Y., Luo, J., Chen, Z., Mei, G., Yan, L.E., 2018. Measuring the albedo of limited-extent
979 targets without the aid of known-albedo masks. Sol. Energy 171, 971–976.
980 https://doi.org/10.1016/j.solener.2018.07.043

981 Sailor, D.J., Resh, K., Segura, D., 2006. Field measurement of albedo for limited extent test
982 surfaces. Sol. Energy 80, 589–599. https://doi.org/10.1016/j.solener.2005.03.012

983 Synnefa, A., Pantazaras, A., Santamouris, M., Bozonnet, E., Zinzi, M., Muscio, A., Libbra, A.,
984 Ferrari, C., Coccia, V., Rossi, F., Kolokotsa, D., 2013. Interlaboratory comparison of cool
985 roofing material measurement methods, in: Proceedings of the 34th AIVC - 3rd TightVent -
986 2nd Cool Roofs - 1st Venticool Conference. Athens, Greece; 25-26 September.
987 https://www.aivc.org/resource/interlaboratory-comparison-cool-roofing-material-
988 measurement-methods?volume=34784.

989 Takebayashi, H., Moriyama, M., Sugihara, T., 2012. Study on the cool roof effect of Japanese
990 traditional tiled roof: Numerical analysis of solar reflectance of unevenness tiled surface and
991 heat budget of typical tiled roof system. Energy Build. 55, 77–84.
992 https://doi.org/10.1016/j.enbuild.2011.09.023

993 U.S. Green Building Council, 2018. LEED v4. http://www.usgbc.org/leed

994 United States Environmental Protection Agency, 2018. Energy Star program requirements for

roof products [WWW Document].
https://www.energystar.gov/ia/partners/product_specs/program_reqs/Roof_Products_Program_Requirements.pdf

ESM Appendix A. Product images

(a)

(b)

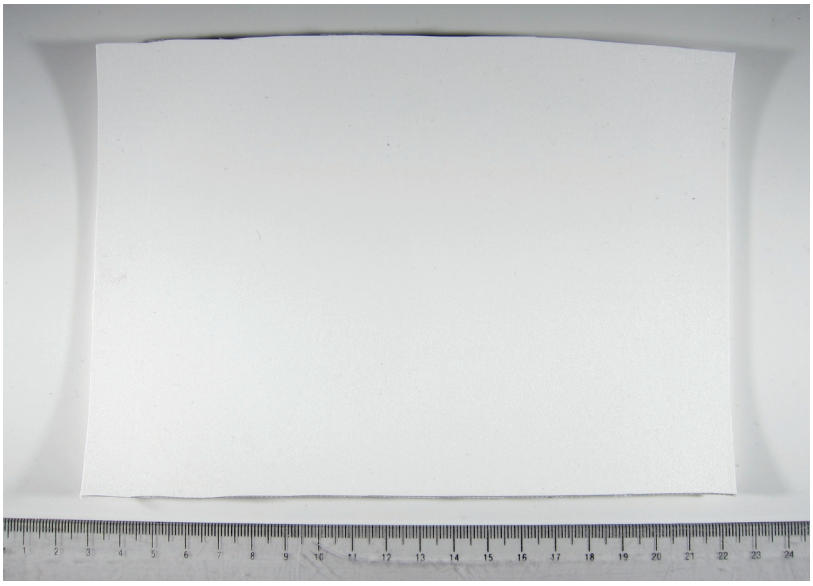

ESM Figure A-1. Images of membrane M1 (white) showing (a) 4 m × 4 m target for E1918/E1918A and (b) 15 cm × 20 cm coupon for C1549 and E903. Code during testing was 1-1.

(a)

(b)

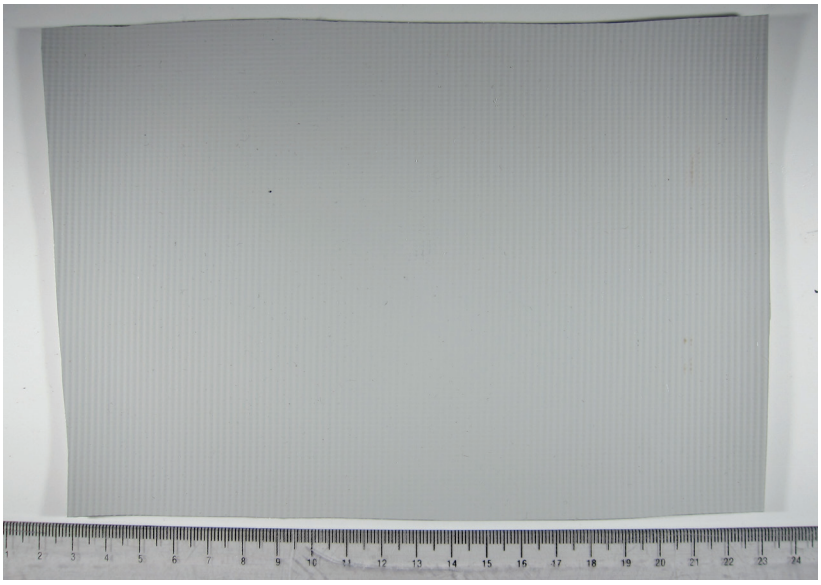

ESM Figure A-2. Images of membrane M2 (gray) showing (a) 4 m × 4 m target for E1918/E1918A and (b) 15 cm × 20 cm coupon for C1549 and E903. Code during testing was 1-2.

(a)

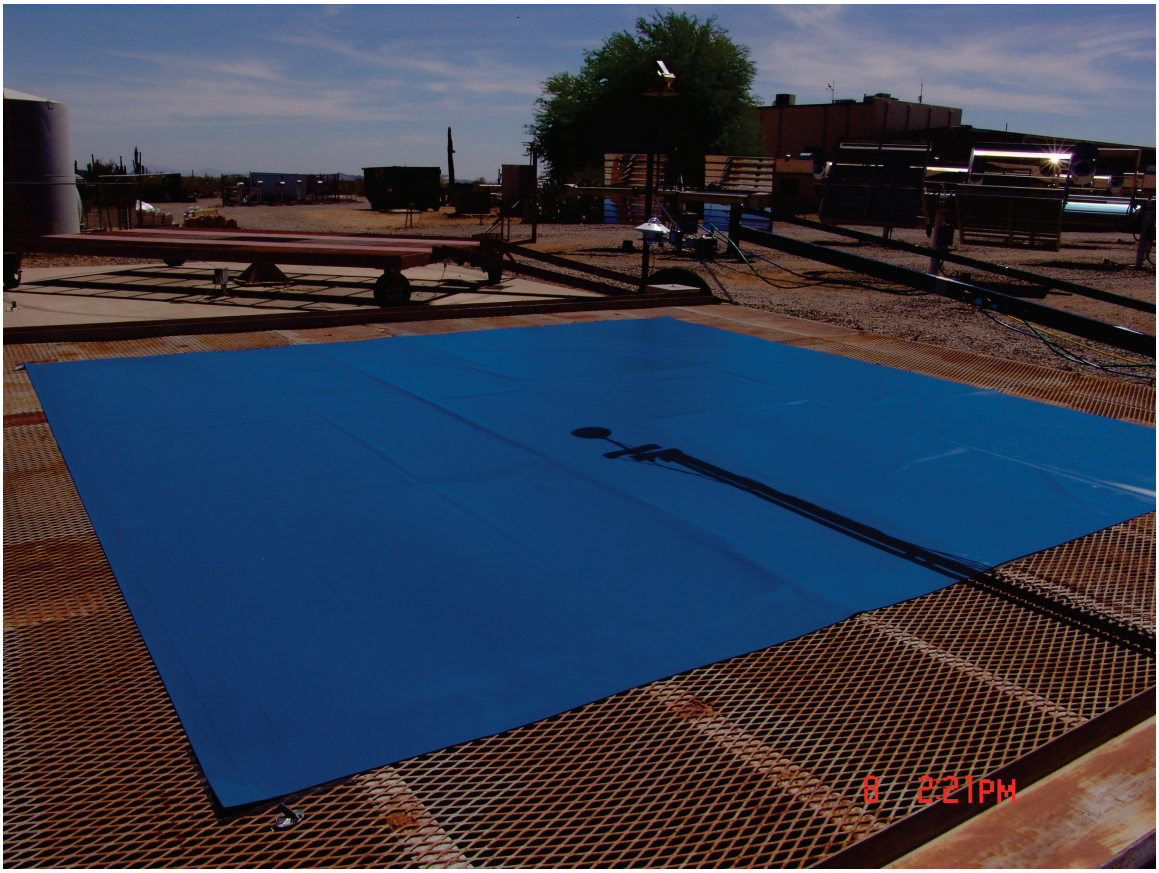

(b)

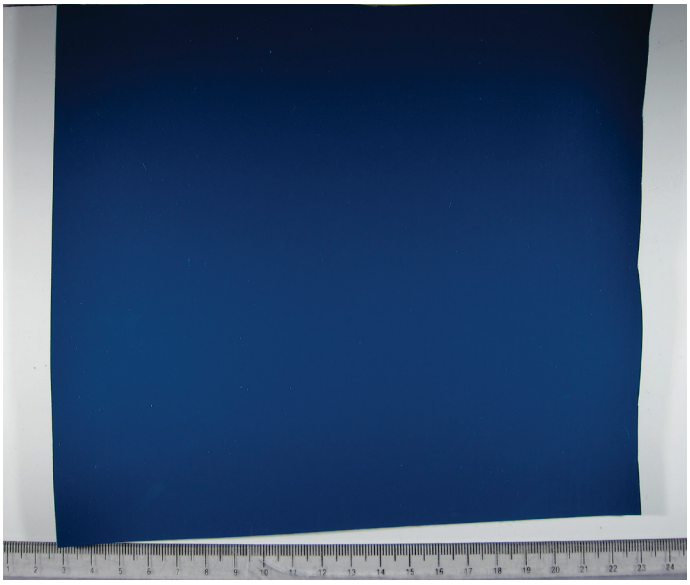

ESM Figure A-3. Images of membrane M3 (blue) showing (a) 4 m × 4 m target for E1918/E1918A and (b) 18 cm × 20 cm coupon for C1549 and E903. Code during testing was 1-3.

(a)

(b)

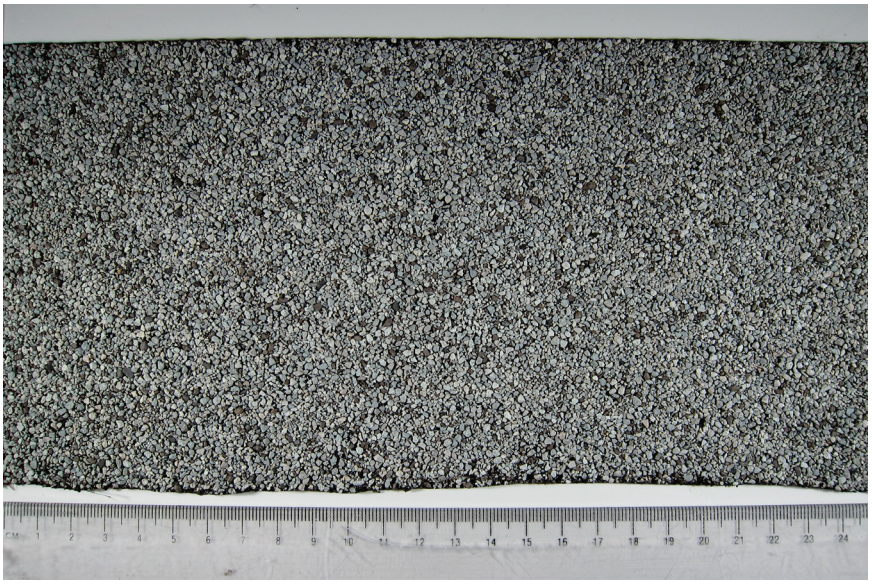

ESM Figure A-4. Images of shingle S1 (gray) showing (a) 4 m × 4 m target for E1918/E1918A and (b) 13 cm × 30 cm coupon for C1549 and E903. Code during testing was 2-2.

(a)

(b)

ESM Figure A-5. Images of aggregate A1 (5/8” gray granite) showing (a) 4 m × 4 m target for E1918/E1918A and (b) 15 cm × 15 cm “box of rocks” for C1549. Numbers in panel *b* mark inches. Code during testing was 3-1.

(a)

(b)

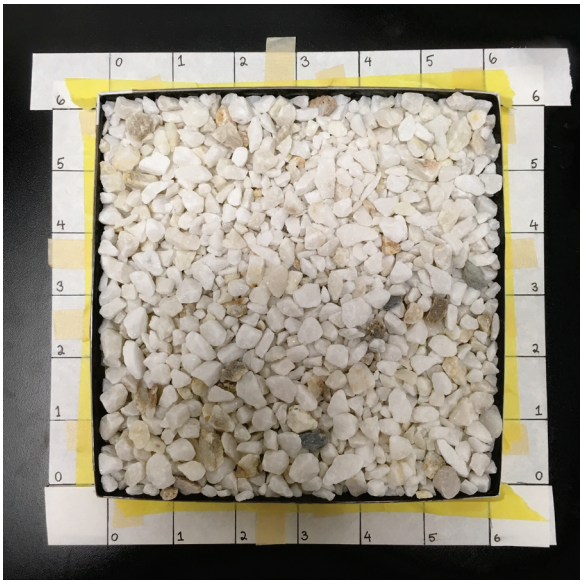

ESM Figure A-6. Images of aggregate A2 (3/8” white marble) showing (a) 4 m × 4 m target for E1918/E1918A and (b) 15 cm × 15 cm “box of rocks” for C1549. Code during testing was 3-2.

(a)

(b)

ESM Figure A-7. Images of aggregate A3 (1.5” multicolor ballast) showing (a) 4 m × 4 m target for E1918/E1918A and (b) 15 cm × 15 cm “box of rocks” for C1549. Code during testing was 3-3.

(a)

(b)

ESM Figure A-8. Images of tile T1 (white) showing (a) 4 m × 4 m target for E1918/E1918A and (b) 8 cm × 8 cm flat chip for C1549 and E903. Code during testing was 5-1.

(a)

(b)

(c)

ESM Figure A-9. Images of tile T2 (orange) showing (a) 4 m × 4 m target for E1918/E1918A, (b) 10 cm × 10 cm curved chip for C1549 and E903, and (c) side view of curved specimen. Code during testing was 5-2.

(a)

(b)

ESM Figure A-10. Images of tile T3 (red) showing (a) 4 m × 4 m target for E1918/E1918A and (b) 8 cm × 8 cm flat chip for C1549 and E903. Code during testing was 6-2.

(a)

(b)

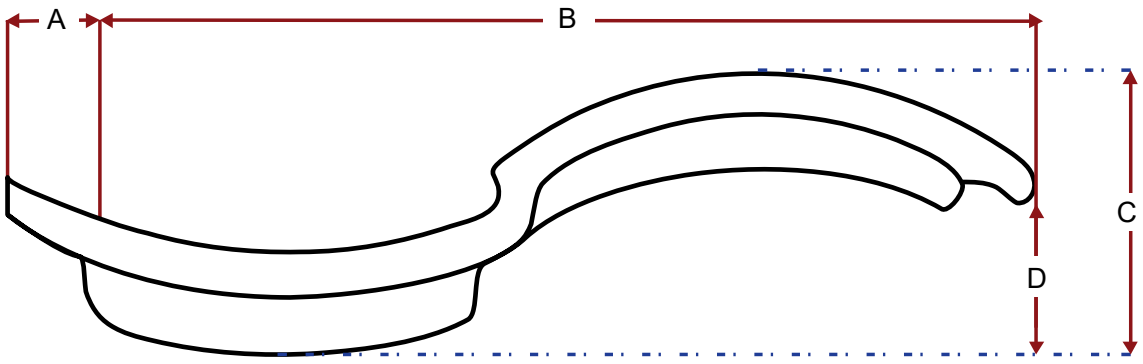

ESM Figure A-11. Image (panel *a*) and dimensioned schematic (panel *b*) of one piece of tile T1 (white concrete S-tile). Dimensions: A = 29 mm (1-1/8”), B = 302 mm (11-7/8”), C = 92 mm, D = [not reported], width (A + B) = 330 mm (13”), length = 432 mm (17”), average thickness = [not reported].

(a)

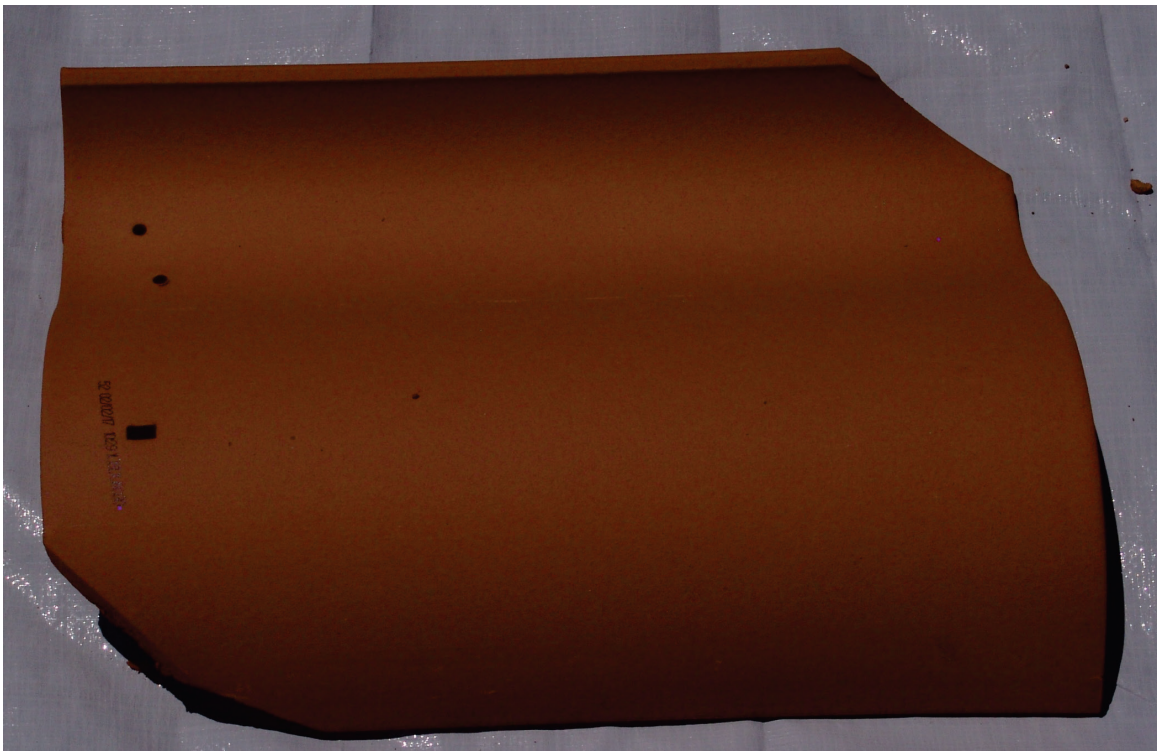

(b)

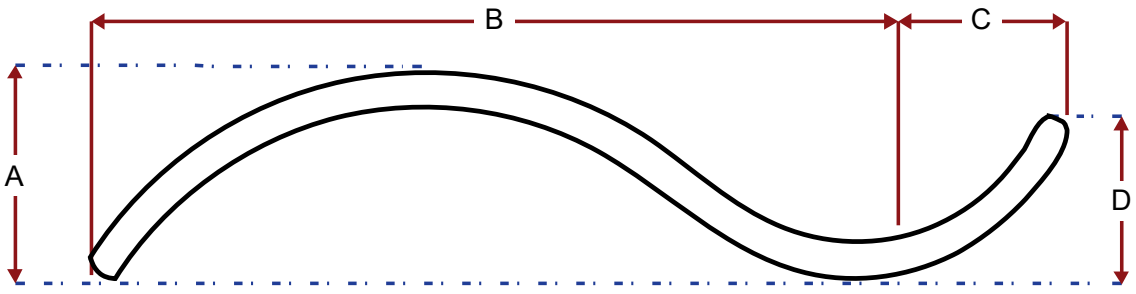

ESM Figure A-12. Image (panel *a*) and dimensioned schematic (panel *b*) of one piece of tile T2 (orange clay S-tile). Note that the tile shown in panel *a* is missing its upper-right corner, while its curve at lower left is a taper. Dimensions: A = 74 mm, B = 279 mm, C = 51 mm, D = 57 mm, width (B + C) = 330 mm (13”), length = 457 mm (18”), average thickness = 12.5 mm.

(a)

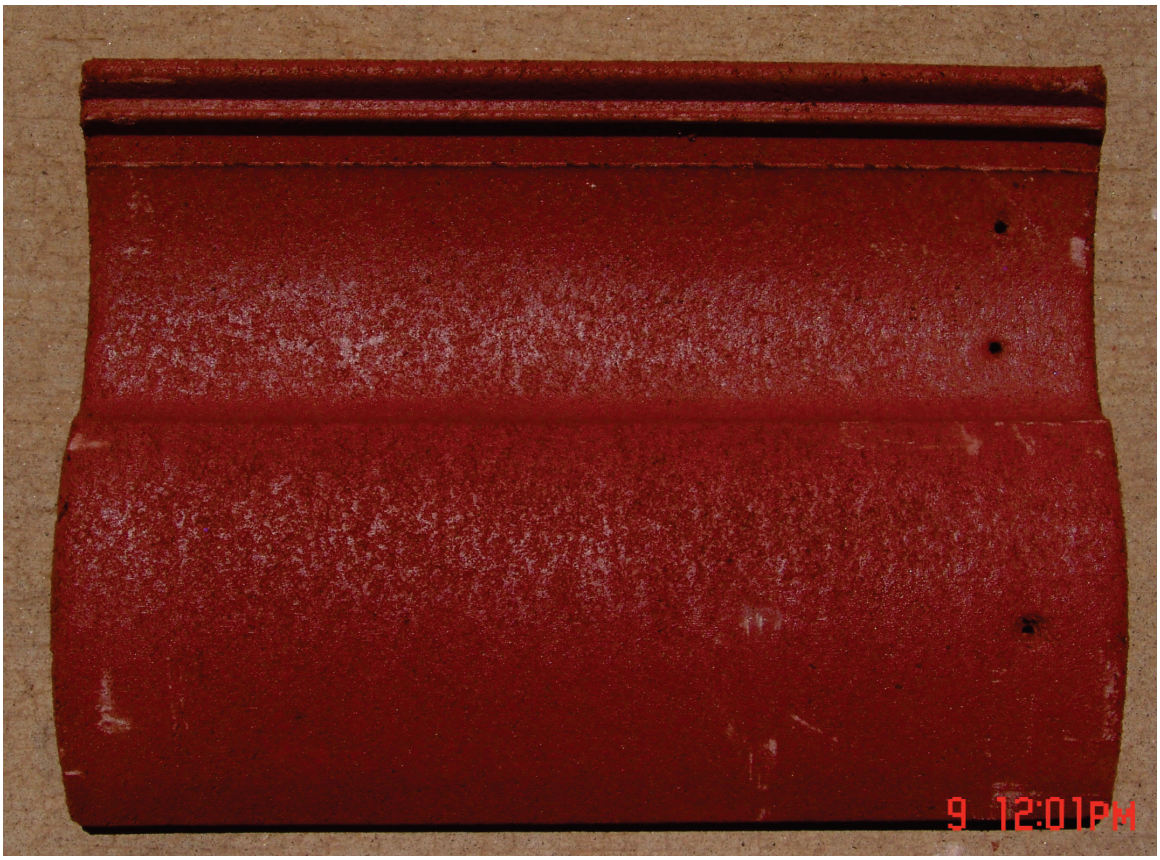

(b)

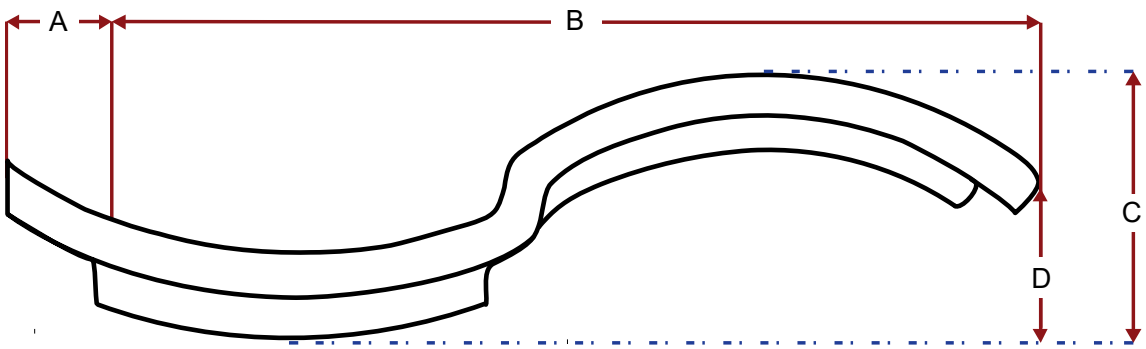

ESM Figure A-13. Image (panel *a*) and dimensioned schematic (panel *b*) of one piece of tile T3 (red concrete S-tile). Dimensions: A = 57 mm (2-1/4”), B = 257 mm (10-1/8”), C = 76 mm (3”), D = 57 mm (2-1/4"), width (A + B) = 314 mm (12-3/8”), length = 432 mm (17”), thickness = 11.9 mm (15/32”).

ESM Appendix B. Measurement images

(a)

(b)

(c)

ESM Figure B-1. Images of E1918/E1918A measurement protocol applied to tile T1 (orange) with tile ridge parallel to horizontal projection of solar beam. Panels show (a) white mask over black mask over target (masked region), (b) black mask over target, and (c) bare target.

(a)

(b)

(c)

ESM Figure B-2. Same as ESM Figure B-1, but with tile ridge perpendicular to horizontal projection of solar beam.

(a)

(b)

(c)

ESM Figure B-3. Images of E1918/E1918A measurement protocol applied to membrane M2 (gray). Panels show (a) white mask over black mask over target (masked region), (b) black mask over target, and (c) bare target.

(a)

(b)

(c)

ESM Figure B-4. Images of E1918/E1918A measurement protocol applied to shingle S1 (gray). Panels show (a) white mask over black mask over target (masked region), (b) black mask over target, and (c) bare target.

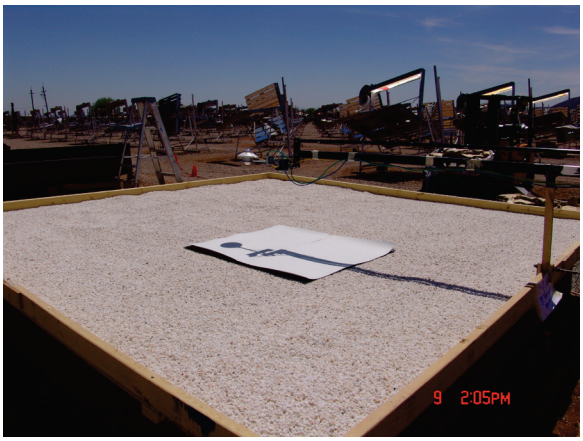

(a)

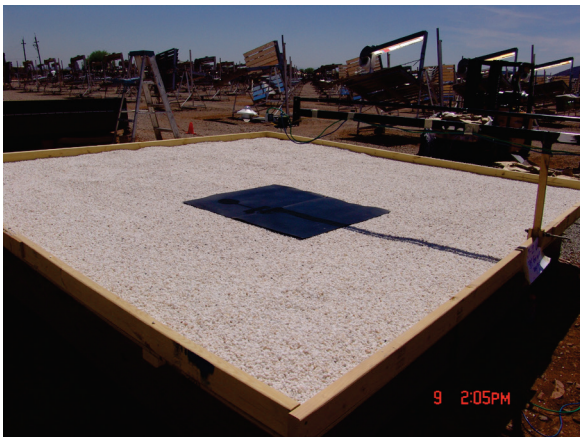

(b)

(c)

ESM Figure B-5. Images of E1918/E1918A measurement protocol applied to aggregate A2 (3/8” fire white marble). Panels show (a) white mask over black mask over target (masked region), (b) black mask over target, and (c) bare target.

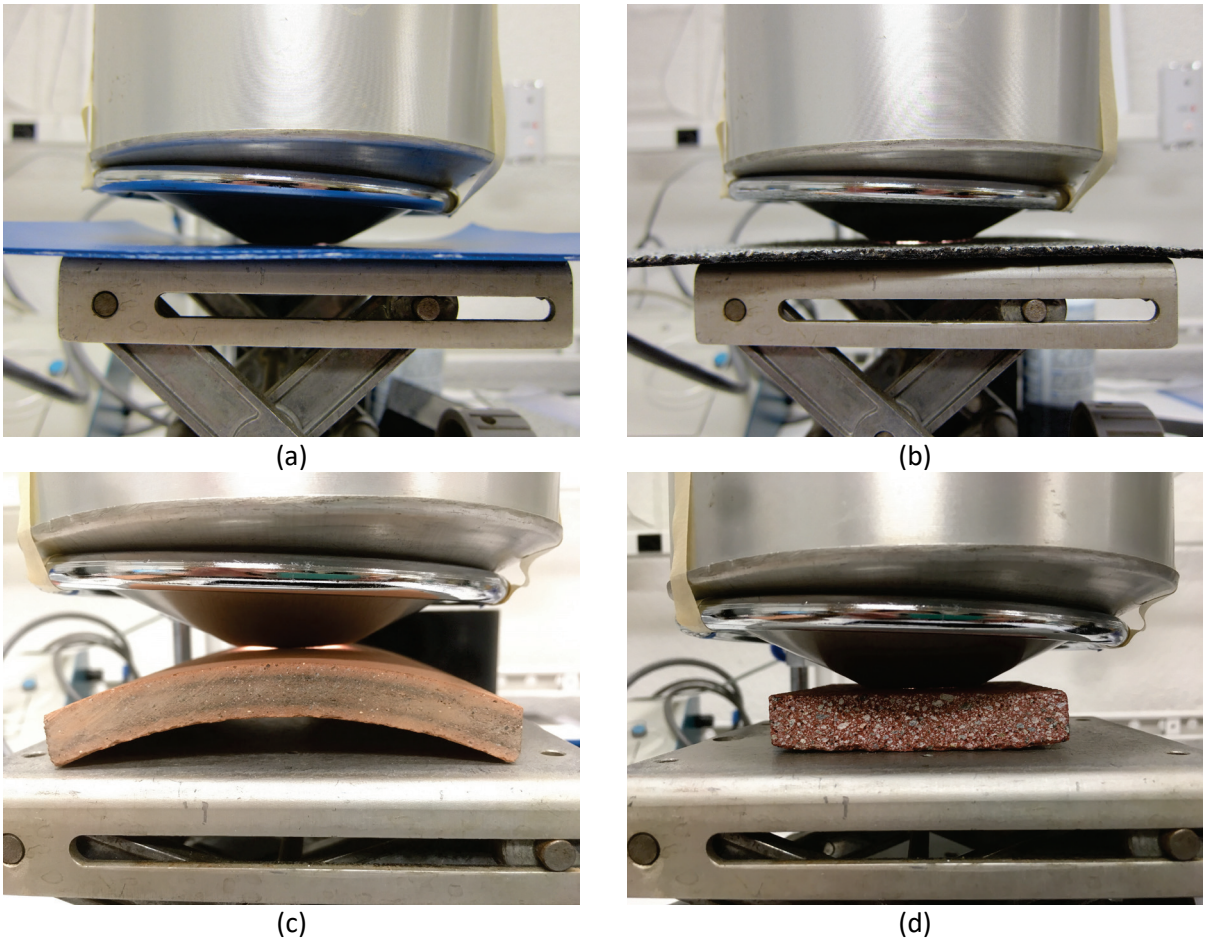

ESM Figure B-6. Images of C1549 measurement protocol applied to (a) membrane M3 (blue), (b) shingle S1 (gray), (c) tile T2 (orange), and (d) tile T3 (red).

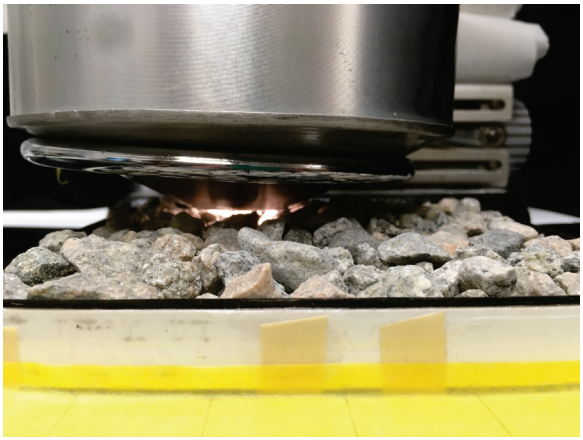

(a)

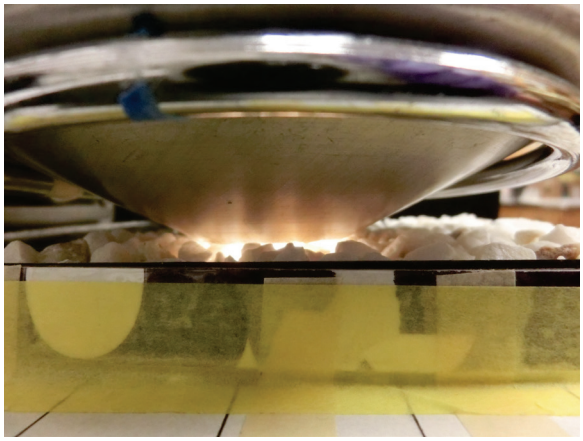

(b)

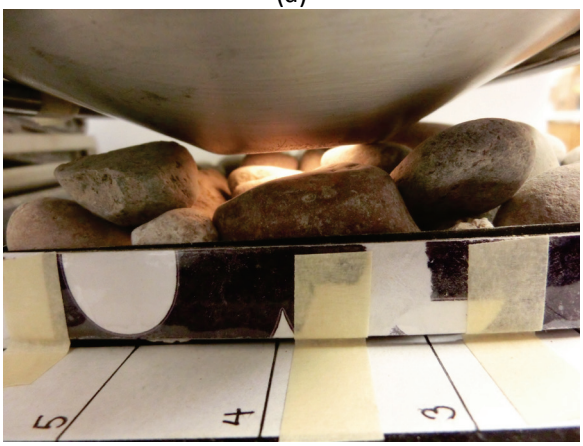

(c)

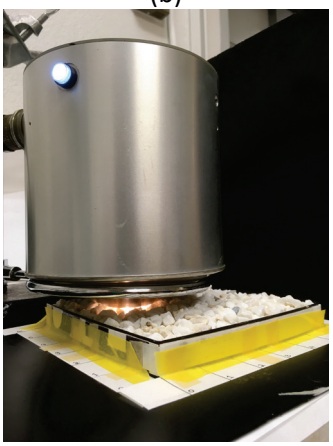

(d)

ESM Figure B-7. Images of "box of rocks" variant of C1549 measurement protocol applied to (a) aggregate A1 (5/8" gray granite), (b) aggregate A2 (3/8" fire white marble), and (c) aggregate A3 (1.5" multicolor ballast). Panel *d* shows the measurement of aggregate A2 from greater distance.

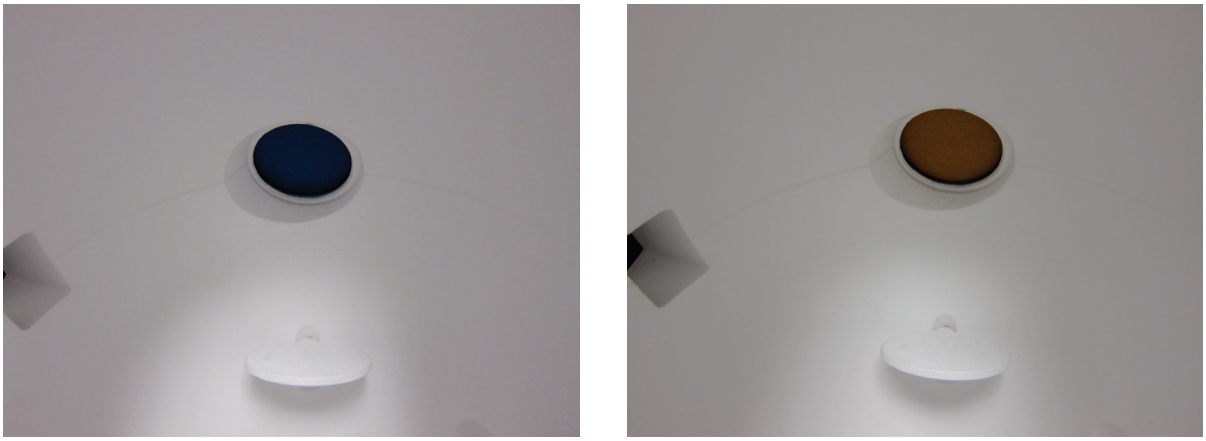

(a) (b)

ESM Figure B-8. Images of E903 measurement protocol applied to (a) membrane M3 (blue) and (b) tile T2 (orange), showing each specimen at reflectance port of integrating sphere.

(a)

(b)

ESM Figure B-9. Images of (a) carousel (turntable) and (b) aggregate table showing background (surroundings) of test specimens. Each photo was taken in December 2018, approximately 7 months after the E1918/E1918A trials. Source: Joseph Farley (Atlas).